STUDY OF ELECTRO-MECHANICAL PROPERTIES OF MANGANESE-BASED NANOCOMPOSITES FOR SUPERCAPACITORS

Musanna Galib

DEPARTMENT OF MECHANICAL ENGINEERING
BANGLADESH UNIVERSITY OF ENGINEERING AND TECHNOLOGY

DHAKA-1000, BANGLADESH

May 2019

STUDY OF ELECTRO-MECHANICAL PROPERTIES OF MANGANESE-BASED NANOCOMPOSITES FOR SUPERCAPACITORS

by

Musanna Galib

(0417102007)

Submitted in partial fulfilment of the requirements for the degree of Master of Science in Mechanical Engineering

Under the supervision of

Dr. Md. Ashiqur Rahman
Associate Professor
Department of Mechanical Engineering
Bangladesh University of Engineering and Technology (BUET)

BANGLADESH UNIVERSITY OF ENGINEERING AND TECHNOLOGY

DHAKA-1000, BANGLADESH

May 2019

Certificate of Approval

The thesis titled, "**Study of Electro-mechanical Properties of Manganese-based Nanocomposites for Supercapacitors**", submitted by **Musanna Galib**, Roll No: **0417102007**, Session: **April 2017**, has been accepted as satisfactory in partial fulfilment of the requirements for the degree of **Master of Science in Mechanical Engineering** on May 8, 2019.

08/05/19

Dr. Md. Ashiqur Rahman
Associate Professor
Department of Mechanical Engineering
BUET, Dhaka

Chairman
(Supervisor)

Dr. Md. Ashraful Islam
Professor and Head
Department of Mechanical Engineering
BUET, Dhaka

Member
(Ex-Officio)

Dr. Mohammad Arif Hasan Mamun
Professor
Department of Mechanical Engineering
BUET, Dhaka

Member

Dr. Mohammad Nasim Hasan
Professor
Department of Mechanical Engineering
BUET, Dhaka

Member

08.05.19.

Dr. Md. Shakhawat Hossain Firoz
Professor
Department of Chemistry
BUET, Dhaka

Member
(External)

Candidate's Declaration

This is hereby declared that this thesis or any part of this thesis has not been submitted elsewhere for award of any degree or diploma.

08/05/19

Musanna Galib

May 8, 2019

ACKNOWLEDGEMENT

At first, I want to pay my gratitude to Almighty ALLAH for giving me the zest, strength and skill to complete this thesis work.

I would like to express my deepest gratitude to my honourable thesis supervisor, Dr. Md. Ashiqur Rahman, Associate Professor, Department of Mechanical Engineering, BUET, for his unwavering support, mentorship, valuable guidance and suggestion throughout this study. Without his initiative ideas, encouragements, careful supervision this challenging work would not have been possible to complete successfully.

The author would like to express his sincere gratitude to Dr. Md. Shakhawat Hossain Firoz, for introducing me to the most interesting field of energy storage materials and also for his precious advice and recommendations which have helped tremendously to improve this research work. I am also very much thankful to my other faculty members for their constant support during my thesis work.

I would like to convey my deepest gratitude to the board of examiners for their valuable corrective suggestions regarding this dissertation.

I cannot but thank Mohammad Mozammal Hosen, Scientific Officer, Chemistry Division, Atomic Energy Centre, Bangladesh Atomic Energy Commission, Dhaka, Sourav Saha, Assistant Professor, BUET, Dr. Joyanta Kumar Saha, Assistant Professor, Jagannath University and Dr. Md. Mominul Islam, Associate Professor for their cordial co-operation during laboratory work and in writing the thesis.

Institute of Information and Communication Technology (IICT), BUET provided me the opportunity to use high speed computational facilities. I am really grateful to IICT for using their computational resources.

I express my gratitude and appreciation to different laboratories in BUET like the Post Graduate Lab (Department of Mechanical Engineering, BUET), Nanochemistry Research Laboratory (Department of chemistry, BUET) as well as to the corresponding personnel for their help and support with ideas, instruments and devices that were essential for my experimental and simulation work.

I would like to thank all others who are directly or indirectly related to this thesis by sharing their ideas, suggestions and finally by supporting me. I would like to express my warmest gratitude to my family members- my mother, father and brother for their continuous inspirations, moral supports and immeasurable sacrifices during this project. Last but not least, I would like to thank my wife precious for her support and endurance during my studies and conscientiously editing this thesis. Such an act can only be inspired by love.

“The journey of a thousand miles begins with a single step”

— Lao Tzu

ABSTRACT

The Electric Double Layer (EDL) supercapacitors can have extremely high-power densities, incomparable cycle life, stability, and reliability, as a result they are already used in uninterruptible power systems (UPS), memory back-up systems and even in the emergency doors of Airbus A380. Graphene-based electrodes with appropriate defects (encapsulated metal or metal oxide nanocomposite) and optimized alignment display enhanced capacitive behavior and can provide good cycling performance of energy storage material. Graphene is a mono-atomic layer of Sp^2 hybridized carbon with honeycomb lattice structure. When engineered with metal oxides, they show high electrochemical double layer capacitance through synergistic effect. MnO_2 has been investigated extensively as a suitable material for high-performance electrochemical capacitor due to its low-cost, rich redox behavior and good environmental compatibility. In this work, the potential for rGO-MnO_2 nanocomposite to be used as supercapacitor material has been examined in detail, both experimentally and *via* molecular dynamics simulation. To examine the performance of the nanocomposite experimentally, Cyclic Voltammetry and Galvanostatic Charging Discharging experiment (Chronopotentiometry) have been performed at several scan rates and several current densities, respectively. For active mass of 0.000405g and potential window of -100 – 800 mV, specific capacitance of 261 F/g has been obtained from Galvanostatic Charging Discharging, which is moderately good enough to use in a supercapacitor. In depth analysis using molecular dynamic (MD) simulation method has performed to understand the atomistic configuration of existing rGO-MnO_2 structure and to improve the nanocomposite electrode structure for better performance. Our study suggests an improved design of rGO-MnO_2 nanocomposite electrode by adding nano slit-pore in a particular way which can be called 'nano slit-pore' model. Using this model electric potential as a result specific capacitance shows higher values than typical planer model. This is because adding slit-pore in the electrode surface increases the ion-electrode interaction as a result more solvent and electrolyte ions clustered near electrode surface and provides higher capacitance values. Our results clearly indicate that slit-pore in nanoscale creates opportunity to use the potential of graphene sheet edges to improve the capacitance. Upon charging, the structure of the EDL exhibits a greater response near the edges due to the preferential accumulation of excess charge carriers toward the edges. And also the rGO-MnO_2 sheets incorporate its potential which is calculated through experiment and showed qualitatively through simulation.

Summation of these two effects increases the specific capacitance of electric double layer supercapacitor and we proposed the model as 'nano slit-pore' model. Findings from this study will enable us to enhance the energy storage capability of rGO-MnO_2 nanocomposite EDL supercapacitor.

Nomenclature

A	: Surface area of the electrode
C	: Capacitance of the EDLC
C_S^{St}	: Capacitance of the Stern layer
C_S^{D}	: Capacitance of the diffuse layer
C_T	: Total capacitance
d	: Effective thickness of the double layer
e	: Elementary charge (C)
E	: Energy density
P	: Power density
Q	: Charge quantity
T	: Temperature (K)
V	: Potential

Subscripts

p	: Positive electrode
n	: Negative electrode
A	: Anode
C	: Cathode

Greek letters

ε_0	: Vacuum's dielectric constant
ε	: Relative dielectric constant

Abbreviation

AN	: Acetonitrile
CNT	: Carbon nanotube
c-DFT	: Classical density functional theory
Cl^-	: Chloride
DFT	: Density functional theory
EC	: Equivalent-circuit
EDL	: Electric double-layer
EDLC	: Electrical double layer capacitor
ES	: Electrochemical supercapacitor
ESR	: Equivalent series resistance
GC	: Gouy-Chapman
GCS	: Gouy-Chapman-Stern
IHP	: Inner Helmholtz plane
MC	: Monte Carlo
MD	: Molecular dynamics
Mn	: Manganese
MnO_x	: Manganese oxide
Na^+	: Sodium
OHP	: Outer Helmholtz plane
q-DFT	: Quantum density functional theory
R_S	: Equivalent inner resistance
RTIL	: Room-temperature ionic liquids
SPC/E	: Simple point charge
TIP3P	: Three-point transferrable intermolecular potential

Table of Contents

List of Figures

Figure No. **Title** **Page**

List of Tables

CHAPTER 1
Introduction

1.1 Background

In this modern world, extraordinary growth of electronic equipment such as portable communication devices and hybrid electric vehicles has created an increasing demand for high-power energy resources. As a common example battery has shown its importance in everyday life because it can store sufficient amount of energy in a relatively small volume and weight. However, as illustrated in figure 1.1 for the most important energy storage systems, batteries have high energy density in the order of 180 Wh kg^{-1} but unfortunately suffer from slow power delivery [1]. This limitation reduces the widespread use of batteries, especially in the field of high power-coupled with fast storage systems. An alternative approach of this problem is to use 'Electrochemical capacitors' (EC), which are also known as supercapacitors or ultracapacitors. The EC can provide some excellent features which stimulate extensive interests to study these components such as high specific power (10 kW kg^{-1}), a long cycle life (>10^5), and fast charge/discharge processes [2].

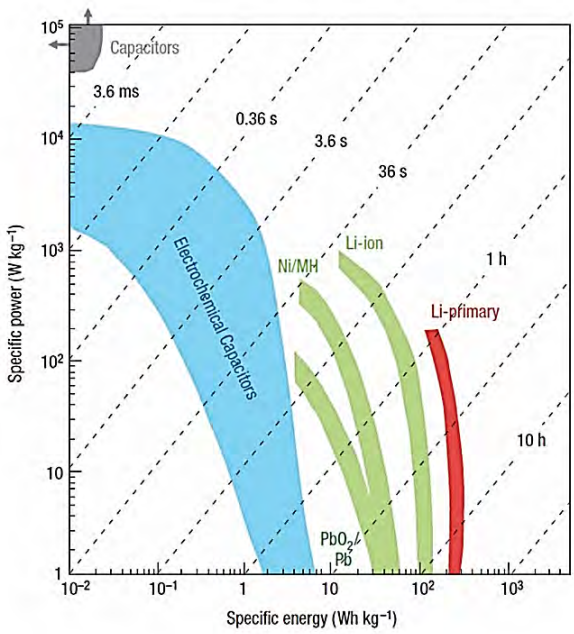

Fig 1. 1: The plot shows the specific power against specific energy for different energy storage systems. Here, time shown in the plot is obtained from the division of energy density to power. As an example to explain the plot, the specific power indicates how fast the vehicle

can move where as the specific energy indicates the distance a vehicle can move on a single charge [3].

Currently, widespread uses of electrochemical capacitors show its importance in the energy industry. For example, supercapacitors are used in electronic devices, memory back-up systems, industrial activities [4]. One of the major advantages is their ability to provide the energy necessary to accelerate a vehicle's start-up by acting as an intermediate power source along with batteries. This phenomenon enables the battery to reduce the stress develops on it due to the fast discharging requirement at the starting of vehicle.

1.2 Electrochemical capacitors

The mechanism by which electrochemical capacitors store energy has been discussed in detail in this chapter. In principle, capacitive behaviour can be classified into two categories: the electrical double layer capacitance and pseudo-capacitance. The physics of electrical double layer capacitance is the pure electrostatic attraction between ions and the charged electrode surface [5] whereas for pseudo-capacitance the reason is fast and reversible oxidation-reduction or Faradic charge transfer reactions on the electrode surface [6]. As schematically represented in Fig. no. 1.2, 1.3 and 1.4, while the charging occurs, the anions and cations of electrolytes in electric double layer capacitors (EDLCs) are attracted to positive and negative electrode surface, respectively [7]. Though the electrolyte ions

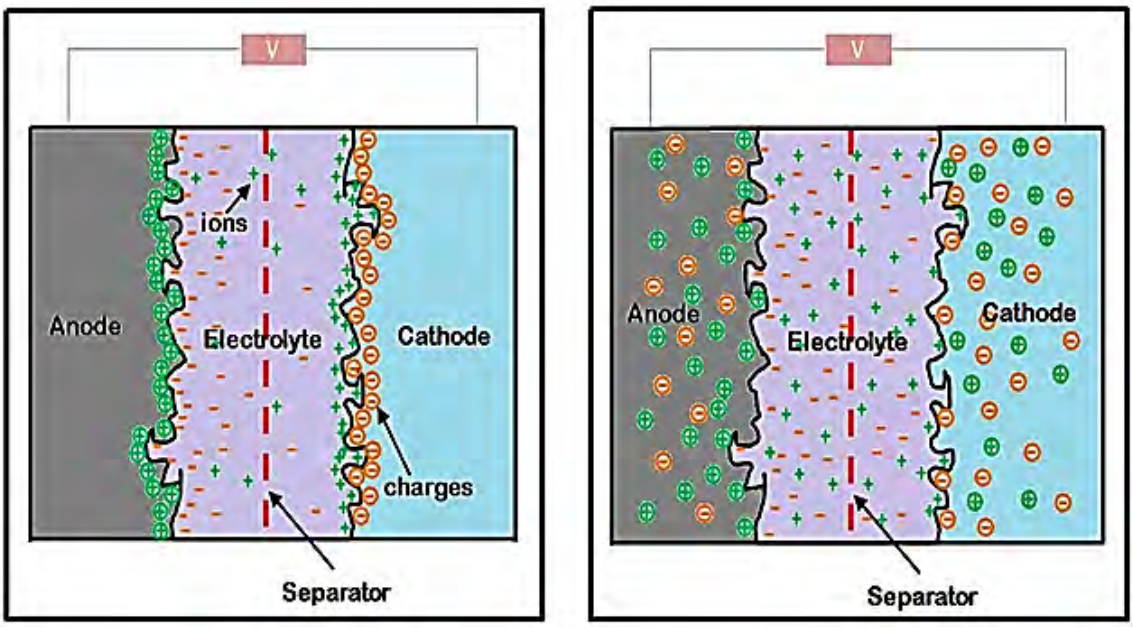

Fig 1. 2: Schematic representation of a porous carbon electrical double layer capacitor in a charged (left) and discharged state (right) [8].

are attracted to the electrode surfaces during charging process, there is no reaction between the ions and surface material or no adsorption of ions in surface. The resultant capacitance from the electric double layer capacitors are largely dependent on the electrode's surface composition, surface area, electrolyte types and the Debye length where Debye length represents the effective thickness of the double layer. The following formula represents the specific capacitance of EDLCs:

$$C = \frac{\varepsilon_r * \varepsilon_0 * A}{d} \tag{1.1}$$

where C is the capacitance of the EDLC, ε_r is the electrolyte's dielectric constant, ε_0 is the vacuum's dielectric constant, d is the effective thickness of the double layer, and A is the surface area of the electrode. Electrolyte ions can access only to the surface of the electrode that means only the surface contributes to charge storage. Therefore, optimization of pore size, pore structure, surface properties and conductivity of the electrode materials is essential to improve the performance. Advantages of this mechanism include very fast energy storing and delivery and also high stability of EDLCs during charge-discharge cycles. On the other hand, redox reaction is the key for pseudo-capacitance between the electrode and electrolyte. In this mechanism, charges which accumulate in the electrode and electric potential are strongly related to each other. This relation can be expressed by eqn. 1.2 as follow:

$$C = \frac{dQ}{dV} \tag{1.2}$$

where C is the pseudo-capacitor's capacitance, Q is the charge quantity and V is the potential. Pseudo-capacitors typically show much higher capacitance than that of EDLCs. But this type of capacitors generally suffers from low power density and lack of stability. These problems occur due to poor electrical conductivity and swelling of framework during cycling.

1.3 Development of mean-field electrical double layer theory

1.3.1 Electric double layer (EDL)

Due to its high-power density, supercapacitor's demand has been increased all around the world. Graphene with a high surface area as well as the ionic liquid (IL) with many unique properties, make them highly desirable. Thus, a theoretical understanding of the capacitance behavior on such newly developed materials is greatly needed. Over the past few decades, a mean-field theory (MFT) is observed and referred frequently by scientists. The Gouy–Chapman (GC) EDL model is one of these MFT theories. In this article, the development of mean field based EDL theories will be overviewed which has to become a great deal of attention in the energy industry.

The first EDL model had been proposed by Helmholtz [9],

$$C_H = \frac{\varepsilon * \varepsilon_0}{d} \tag{1.3}$$

where ε is relative dielectric constant, ε_0 is free space's permittivity and d is the width between the two parallel plates with opposite charge. Eqn. 1.3 is used to calculate the specific capacitance C_H of parallel plate capacitor, which indicates that higher relative dielectric constant and shorter distance between the two plates can give enhanced capacitance.

As depicted in Fig. no. 1.3 and 1.4, the counterions will accumulate on the electrode due to the electrostatic interactions in the interface between a charged electrode and ionic electrolyte. Such arrangement may be analogous to the parallel plate capacitor, with the other plate forming by the counter-ion layer. A distinct feature of such a capacitor is that the distance between the two "plates" is much shortened. Theoretically, the distance is often attributed to the radius of the ions on the nanometer scale. Due to such short distance d, the capacitance C_H by eqn. 1.3 is much enhanced, and a capacitor formed by such EDL is the so-called electrochemical capacitor or supercapacitor.

In this model, it is assumed that only an electrolyte composes the solution. And no electron transfer reactions occur in this model. Further, the ions in the solution interact with electrode surface by electrostatic interactions which resulted from the fact that the electrode holds a charge density (q^m). This charge density is created at the electrode surface by either an excess or deficiency of electrons. The charge held on the electrode is balanced by the redistribution of ions close to the electrode surface because of keeping the interface neutral.

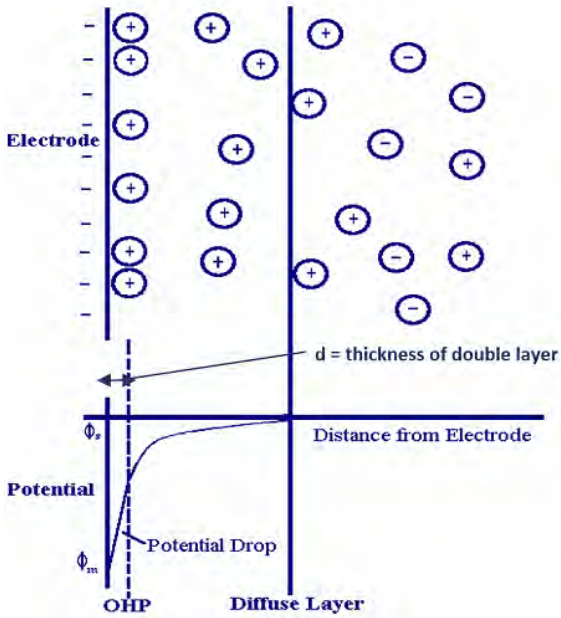

Fig 1. 3: Potential profile with distance from electrode in EDLC [10].

A layer of ions attracted to the electrode surface has been formed by balancing the electrode charge. The approach distance of this layer is assumed to be limited to the combination of ion radius and a single sphere of solvation shell round each ion. This results in combination of two layers of charges which is called the double layer. A potential drop also happens only in this region which is known as 'Helmholtz Region' in solution [10].

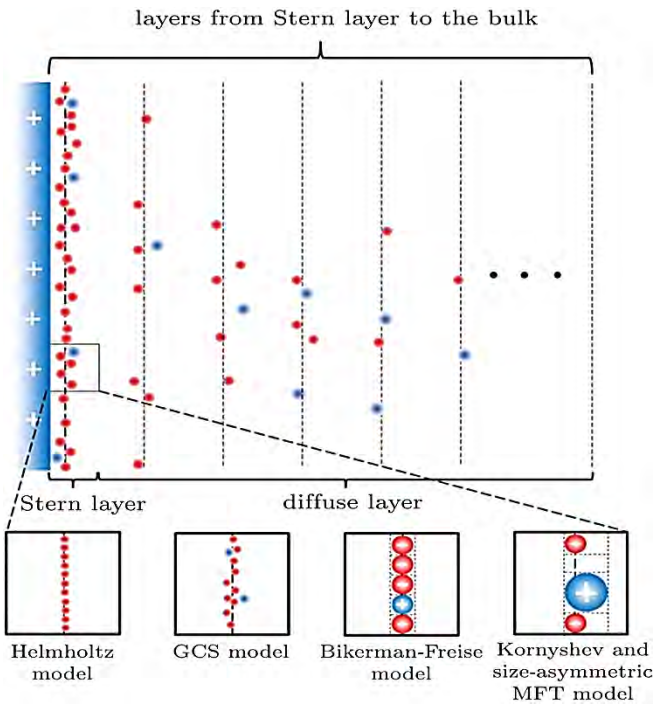

Fig 1. 4: Schematic diagram of electric double layer (EDL). The single charged ion layer adjacent to the electrode forms the compact layer or Stern layer, while the outer layer forms the diffuse layer. The series of the two layers is called the Gouy–Chapman–Stern (GCS) EDL model [11].

1.3.2 Gouy–Chapman–Stern (GCS) model

It is notable that the simple model described by eq n. 1.3 can not predict accurately the complicated EDL structure and electrolyte solution even though it is frequently adopted to study the super-capacitance behavior [12]. It is clear that a single charged layer cannot even closely show the counterions distribution close to the electrode surface. A more realistic picture is the diffuse layer as in Fig. no. 1.4 , as proposed by Gouy and Chapman [13].

In the Gouy–Chapman model, the number density of monovalence ion in the electrolyte solution is given by the Boltzmann distribution

$$c_{\pm} = c_{\infty}\, e^{\pm e\phi/kT} \tag{1.4}$$

in which c_+ and c_- are the density of the cation and anion, respectively, c_∞ is the equilibrium bulk density of individual ions far from the electrode at x = 0, e is the elementary electron charge, ϕ is the electrostatic potential, k is Boltzmann constant and T is the temperature. The Boltzmann distribution in eqn. 1.4 is a mean field approximation to the ionic density, and the charge density ρ in the diffuse layer is given by

$$\rho = e\,(c_+ - c_\infty) = -\,2\,ec_\infty \sinh\left(\frac{e\phi}{kT}\right) \tag{1.5}$$

Eqn. 1.5 gives charge density of 1:1 electrolyte system, for which an analytical expression of differential capacitance is available. Applying Poisson equation, *i.e.*,

$$\frac{d^2\phi}{dx^2} = -\frac{\rho}{\varepsilon * \varepsilon_0} \tag{1.6}$$

the differential capacitance C_d is given by

$$C_d = \frac{\varepsilon\varepsilon_o}{\lambda_D}\cosh\left(\frac{e\phi_o}{2kT}\right) \tag{1.7}$$

in which ϕ_0 is the electrode potential, and λ_D is the Debye length, i.e.,

$$\lambda_D = \sqrt{\frac{\varepsilon\varepsilon_o kT}{2c_\infty e^2}} \tag{1.8}$$

This Gouy–Chapman model in eqn. 1.7 differs from the Helmholtz model of eqn. 1.3 in its extra dependence on ϕ_0. From the electrochemical perspective, C_d in eqn. 1.7 is the natural response of the electrode potential dependent EDL at different ϕ_0, which alters EDL structures and results in different C_d. However, the hyperbolic cosine function in eqn. 1.7 implies that C_d increases with ϕ_0, and this never happens in reality. In order to remedy this, Stern [14] proposed the series of eqns. 1.3 and 1.7, so that the capacitance is given by

$$\frac{1}{C} = \frac{1}{C_H} + \frac{1}{C_{GC}} \tag{1.9}$$

in which C_H and C_{GC} are given by eqns. 1.3 and 1.7 respectively.

Eqn. 1.9 is well known as the Gouy–Chapman–Stern (GCS) model. It has been widely accepted and bears the standard definition of an electric double layer [9]. Besides, the success of the GCS model has been demonstrated in many works [14].

1.4 Characterization of EDLC performance

The two important parameters, which characterize the performance of an EDLC cell, are known as energy density and power density, denoted by E (in Watt-hours per unit mass or volume) and P (in Watts per unit mass or volume). E and P can be expressed as the following [15],

$$E = \frac{1}{2}C_T V^2 = \frac{QV}{2} \tag{1.10}$$

$$P = \frac{V^2}{4R} \tag{1.11}$$

where V (in volt) is the operating voltage, Q denotes the total charges stored in the electrochemical supercapacitor (ES), C_T (in F) is the total capacitance of the cell, and R (in Ω) is the Equivalent series resistance (ESR). From the eqns. 1.10 and 1.11, it is clear that increasing C_T and/or V will increase the energy density of the electric double layer supercapacitor. Interactions between electrode and electrolyte are responsible for the total capacitance of a cell whereas operating voltage is mainly influenced by the electrolyte. Several parameters affect the equivalent series resistance such the material and construction of separator, electrode and electrical conductivity of the separator, electrolyte, electrode, binder.

From the eqn. 1.11, it can be said that EDLCs have a relatively high power density because of low ESR due to absence of charge adsorption and desorption between electrode and electrolytes. On the other hand, energy density is relatively lower for EDLCs. As V is given for an electrolyte, the only option left to increase E is to increase C_T, which can be obtained from the following equation,

$$\frac{1}{C_T} = \frac{1}{C_A} + \frac{1}{C_C} \tag{1.12}$$

where C_A and C_C are the capacitances of the anode and cathode, respectively. Eqn. 1.12 indicates that it is desirable to increase C_A and C_C simultaneously to avoid limiting the total cell capacitance by the electrode. According to the Helmholtz model, the capacitance of a single electrode can be expressed as following [16]:

$$C_S = \frac{\varepsilon_r \varepsilon_o}{H} \text{ [Fm}^{-2}\text{]} \tag{1.13}$$

where ε_r is the relative permittivity, and ε_0 is the permittivity of vacuum (in Fm^{-1}). Based on the Gouy-Chapman-Stern model, C_S consists of two contributions given in eqn. 1.14 - one is from the Stern layer and the other one is from the diffuse layer,[16]

$$\frac{1}{C_S} = \frac{1}{C_S^{St}} + \frac{1}{C_S^{D}} \tag{1.14}$$

where C_S^{St} is the capacitance of the Stern layer and C_S^{D} is the capacitance of the diffuse layer, which can be calculated, for a binary symmetric electrolyte with a constant relative permittivity, from [16],

$$C_S^{D} = \frac{4ze N_A c_\infty \lambda_D}{\psi_D} \sinh\left(\frac{ze\psi_D}{2k_B T}\right) \tag{1.15}$$

where z is the valency of the electrolyte, e is the elemental charge, N_A is Avogadro's number ($N_A = 6.022 * 10^{23}$ mol^{-1}), c_∞ is the molar concentration of the electrolyte in the bulk (in mol

L^{-1}), ψ_D is the electric potential in the diffuse layer, T is the absolute temperature (in K), k_B is the Boltzmann constant(k_B = 1.381 * 10^{-23} m^2 kg K^{-1} s^{-2}), and λ_D is the Debye length defined as [16]

$$\lambda_D = \sqrt{\varepsilon_r \varepsilon_o k_B T} \,/\, \sqrt{2z^2 e^2 N_A c_\infty} \tag{1.16}$$

If Cp and Cn represents the positive and negative capacitances of the two electrodes respectively, the overall capacitance (C_T) of the entire cell can be defined by the following eqn. 1.17:[7]

$$\frac{1}{C_T} = \frac{1}{C_P} + \frac{1}{C_n} \tag{1.17}$$

Depending on the values of Cp and Cn, the ES can be defined as symmetric and asymmetric. For symmetric ES, materials as well as capacitance, of both electrodes will be the same, namely, $Cp = Cn$. As a result, the total capacitance (C_T) will be half of either one's capacitance. Again for asymmetric ES, materials, as well as capacitance will be different for positive and negative electrode. In this case, the total capacitance will be mainly dominated by the electrode with lower capacitance.

In general, it is clear that electrode materials essentially control the capacitance and stored charge. The ES voltage (V) develops across electrodes by charging process whose value is dependent on electrolyte and electrode materials. For example, for aqueous electrolytes with carbon electrodes, the cell voltage window is about 1 V where it is in the range of 3–3.5 V for organic electrolytes. According to eqns. 1.10 and 1. 11, power and energy densities are directly proportional to the square of applied voltage of the cell. Due to this factor higher voltage has a more positive impact on EDLCs energy and power densities rather than increasing capacitance or decreasing ESR. Higher operating voltage can be achieved by optimizing the electrode surface structures and also optimizing the materials that consist the electrode. Furthermore, from eqn. 1.11 another major focus can be the optimization of the electrodes that will reduce the internal resistance of cell which will increase the power density. In general, it is well established that due to rapid combination of charges with electrodes, internal resistance of ES is relatively much smaller than that in batteries. Even faradic-type ES has higher internal resistance than EDLCs though it involves fast electron and ion transfer.

In order to increase total capacitance of a supercapacitor cell, both positive and negative electrode materials and surface have to develop using research and development. To evaluate

an ES's overall performance, the specific capacitance, C_s (Fg^{-1}) is generally used. C_s can be defiend using the following eqn. 1.18:

$$C_S = \frac{C_i}{W} \tag{1.18}$$

where C_i is the electrode capacitance (positive or negative electrode) and W is the weight (in grams) of the electrode material. Though the specific capacitance has been an essential parameter to evaluate an ES cell, it has some limitations. A better electrode material will have a higher specific capacitance but not always a higher specific capacitance indicates the best electrode material. Because specific capacitance largely depends on the structure and thickness of electrode double layer. For example, an extremely thin film by electrolyte ions on the electrode surface will have very low weight and as a result it will yield a huge specific capacitance value. At the end, if it is possible to form a thick double layer using this high capacitance material, a highly capable energy storage system will be developed which will be examined and studied in this research.

1.5 Advantages of Electrochemical Supercapacitors (ES)

Electrochemical Supercapacitors have several advantages when compared to batteries. Some of them are discussed below:

(1) High power density. Specific power versus specific energy of modern storage devices has been shown in Fig. no. 1.5. It is well known that ES display a much higher power delivery (1–10 kW kg^{-1}) when compared to lithium ion batteries (150 W kg^{-1}). The charging-discharging process is significantly faster than those in the batteries which lead to high power density in supercapacitors. The reason behind of fast charging-discharging in the ES is that it stores electrical charges both at the electrode surface and in the bulk near the surface of the solid electrode. Ionic conduction into the electrode bulk does not limit the charge–discharge process. As a result, rapid rates can be achieved which lead to high power density in ES. For example, a normal battery can be fully charged on the scale of hours; on the other hand, an ES can be fully charged or discharged in seconds. Again the energy stored in ES can be used very fast, within 0.1 s, indicating high power density [18].

(2) Long life expectancy. Faradic redox reactions are the main factor to store electrochemical energy in batteries. This redox process restricts the inter-conversion of chemical electrode reagents and also restricts the phase change which makes the process irreversible. On the other hand, there is a negligible amount of phase change phenomena and

very few chemical charge transfer reactions involved while energy is stored in supercapacitor. These extraordinary phenomena give unlimited cyclability to ES.

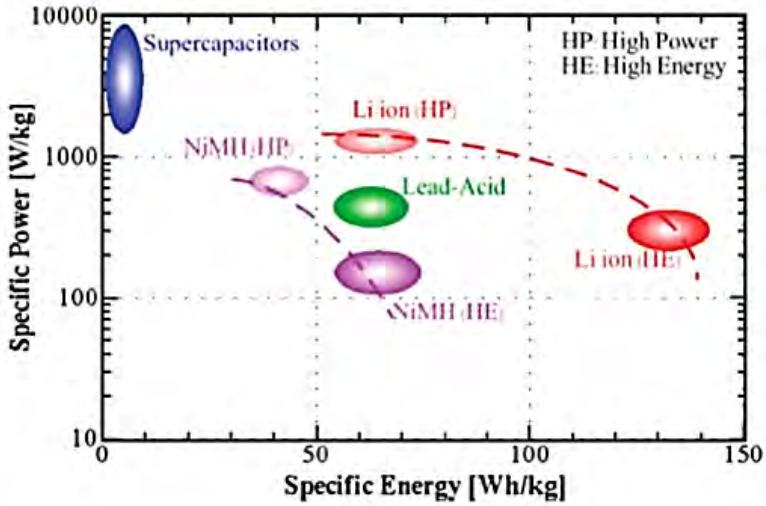

Fig 1. 5: Specific power versus specific energy of modern storage devices [19-20].

Electrochemical supercapacitors can go through a huge number of charge-discharge cycles (for example, up to 1000000) but need no maintenance during their operating period. Moreover, ES can run deeply at high rates for 500000 –1000000 cycles with only small changes in their characteristics. Such longevity is impossible for batteries even if the depth of discharge is as small as 10–20% of the overall energy. The life expectancy for ES is estimated to be up to 30 years, which is much longer than for lithium ion batteries (1000–10000 cycles and a life expectancy of 5 –10 years). Even faradic supercapacitor has better operating lifetime than battery although redox reactions are involved during charging and recharging in both cases [21].

(3) Long shelf life. Long shelf life is a noticeable advantage for electrochemical supercapacitors. Self-discharging and corrosion are the two factors which degrade the performance of unused rechargeable batteries. On the other hand, supercapacitors can hold the capacitance like the original condition even though they are kept in self for a long time. According to some reports, supercapacitors practically showed its long shelf life by remaining close to their original condition even when they are unused for several years.[21]

(4) High efficiency. One of the major advantages of ES is that heat loss management is easier due to reversible behavior during charging-discharging throughout the complete operating range of voltage. The energy loss, as a result, the heat loss is very low during charging-discharging for ES which can be readily removed. For example, high cycle efficiency of ES (around 95%) has been reported even for operating at rates above 1 $kWkg^{-1}$ [22].

(5) Wide range of operating temperatures. ES can function effectively at extremely high and low temperatures. The typical operating temperature for ES ranges from -40 to 70 °C. This is advantageous for military applications, where reliable energy storage is required to run proprietary electronic devices under all temperature conditions during war.

1.5.1 Applications of ES

With their many advantages, ES has become very competitive choices for applications such as electric vehicles, electric hybrid vehicles, digital communication devices, digital cameras, mobile phones, electrical equipments, uninterruptible power supplies etc [23]. For example, due to poorer cycle life of batteries, approximately 20% extra cost for replacement of battery has to be done in battery installed devices [24]. In addition, battery-powered electric vehicles are facing some limitations when peak load needed (i.e. accelerating and climbing) as batteries have lower power density in general. ES can easily solve these problems with their higher power density [20]. Combining ES with batteries can yield improved performance in hybrid electric vehicles, including powerful acceleration, braking energy recovery, excellent cold weather starting, and increased battery life. Thus, it can be said that electrochemical supercapacitors have immense potential to serve in the field of energy storage along with batteries. The main market targeted by ES manufacturers in the coming decades may be transportation, including hybrid electric vehicles and metro trains [20]. Due to their relatively low energy density and high cost, the market development of ES is still in the early commercialization stage. At present, ES occupies a very small portion of energy storage market (less than 1%) and most of the market is in the advanced countries like Japan, South Korea, USA, France [20]. The ES market is moving ahead steadily and changing significantly every year. Continuing improvements will open new markets, leading to a bright future for supercapacitors.

1.6 Challenges for ES

Although ES has many advantages over batteries and fuel cells, they also face some challenges at the current stage of technology.

(1) Low energy density. ES suffer from limited energy density (about 5 $Whkg^{-1}$) when compared with batteries (> 50$Whkg^{-1}$). Commercially available ES can provide energy densities of only 3–4 $Wh\,kg^{-1}$. If a large energy capacity is required for an application, a larger supercapacitor must be constructed, driving up the cost. Low energy density is the major challenge for ES applications in the short and medium terms.

(2) High cost. One of the major challenges for electrochemical supercapacitor commercialization is the costs of manufacturing and raw materials. The majority cost comes from electrode material, separator and electrolyte where electrode materials generally share the largest portion. For example, Carbon and RuO_2 are the most common and high performance electrode materials now-a-days where it has to be mentioned that RuO_2 is a rare metal oxide and carbon materials with a high surface area are pretty expensive (US$50–100 per kg) [21]. In addition, if organic electrolytes are used the cost will definitely increase.

(3) High self-discharging rate. ES have an alarming limitation in the field of practical use that is its high self discharging rate. For some application- it shows a high discharging rate of 10–40% per day and also low duration [25].

(4) Wide range of operating temperatures. ES can function effectively at extremely high and low temperatures. The typical operating temperature for ES ranges from -40 to 70 °C. This is advantageous for military applications, where reliable energy storage is required to run proprietary electronic devices under all temperature conditions during war.

In summary, above mentioned challenges limits the use of EC in commercial sectors though noticeable parameters such as efficiency, reversibility, shelf life, environmental friendliness also show more positive impact for EC than others [26].

1.7 Objectives of the Present Study

From the previous sections, it is evident that, the use of EDLCs as efficient energy storage devices is a rapidly advancing field. Optimization of EDLCs as a whole system, and discovery of new electrode materials and electrolyte combinations with high electro-capacitive performance are critical areas, where molecular modeling can make important contributions. In recent years, molecular modeling has contributed greatly to the understanding of charge storage mechanisms and dynamics in EDLCs in response to experiments that have challenged long held views of the EDL. Molecular modeling has largely focused on planar electrodes to study steric and potential effects, and porous electrodes to study confinement effects, under equilibrium conditions. Polarisation of the electrode by the electrolyte enhances surface charge via induced charges, resulting in an increase in electric field strength and capacitance. This is a critical feature that needs to be included in molecular models that aim to quantitatively reproduce experimental results and accurately represent real systems. In comparison, dynamic effects have been modeled to a lesser extent and suggestions for exploiting these effects to increase EDLC performance are lacking. Focusing properly on ionic transport and charging-discharging kinetics using

molecular modeling will improve the performance of dense RTIL electrolytes in nanoporous carbons. Furthermore, as charging-discharging has a direct relation with energy and power densities, performing simulations to predict the kinetics of different charging-discharging rates will be very useful. So far, some of the performance manipulating parameters for EDLC such as polarisation relaxation, temperature, electrode geometry, and ion size effects has been studied using the Dynamic EDLC phenomena.

Developing effective models in these areas may be crucial for efficiently identifying conditions and materials that can lead to huge gains in EDLC performance. The goal of the present research is to analyze and understand the capability of Graphene-MnOx nanocomposite as a promising energy storage material in supercapacitor applications.

The specific objectives of the present study are-

- To study the specific capacitance and cyclic charging/discharging performance of the Graphene/MnO_x nanocomposite using cyclic voltammetry (CV) and chronopotentiometry (CP) experiments, respectively, for examining its suitability for practical applications.
- To perform molecular dynamics (MD) simulations, characterizing the electrode, electrolytes and solvent interactions, to explain the findings from the CV and CP.
- To examine the energy storage performance of the Graphene/MnOx nanocomposite via molecular dynamic simulation.
- To study the atomistic behavior of the nanocomposite for energy storage capability with different atomistic structures and design modifications for performance enhancement.
- To analyze the energy and power density characteristics of the Graphene/MnOx nanocomposite as a supercapacitor.

The present study is expected to provide considerable insight into establishing an appropriate algorithm to simulate the characteristics of generic double-layer capacitive system using Graphene/MnOx nanocomposite. The findings of the effect of incorporating design modifications at the micro-structural level, such as carbon slit-pores, will enable us to understand their role in the possible performance enhancement of the supercapacitors. The cyclic voltammetry (CV) and chronopotentiometry experiments will provide performance data to assess the potential of the Graphene/MnOx nanocomposite in real-life applications as supercapacitors.

CHAPTER 2

Literature Review

2.1. Pioneering Works

Pure carbon-based capacitors cannot meet the requirements in high energy storage field by the specific capacitance derives from EDLC. Adding additional contributions from pseudo-capacitance is an efficient method to enhance the capacitance. To enhance the energy storage capacity, transition metal oxides (MO_x) such as RuO_2, MnO_2 might be a promising material to use with carbon as they possess high theoretical pseudo-capacitance. Despite of having lower capacitance in bulk than the theoretical value, deposition of MO_x onto carbon increases the effective utilization of the active materials and also improves the electrical conductivity of the composites. This is because composite of porous carbon and transition metal oxides can show high surface area and good electrical conductivity. This indicates the limitations of MO_x as independent electrode materials and tremendous opportunity to act as composite with carbon in the field of high power supercapacitors.

The most promising electrode material for supercapacitors is RuO_2 due to its much long cycle life, highly reversible redox reactions and high specific capacitance. For example, a specific capacitance up to 599 Fg^{-1} has been obtained for RuO_2 /carbon composites with 80 wt% of RuO_2 loading [27]. Though RuO_2 shows excellent performance in case of specific capacitance, the high cost greatly restricts its commercial application. Recently, MnO_2 has been investigated as a suitable alternative material due to its low-cost, rich redox behavior and good environmental compatibility. Gao *et al.* [28] have prepared homogenous MnO_2 /MWNT(multi-walled nanotubes) composite via an in situ coating technique. The specific capacitance of the composite is 250.5 Fg^{-1}, which is about eight times higher than that of the pure MWNT. Dong *et al.*[29] have prepared MnO_2 /mesoporous carbon composites with different nanoparticle sizes embedded into the matrix through redox reaction between permanganate ions and carbons. They have found that the capacitance of the composites improved with increasing MnO_2 amount. A high capacitance up to 220 Fg^{-1} was obtained for the composite with the highest MnO_2 loading and 600 $F g^{-1}$ was calculated based on the MnO_2 content. Carbon nanotube array (CNTA) is another ideal support which is vertically grown on the current collector. By using this CNTA as a support, a binder-free MnO_2 /CNTA electrode with hierarchical porous structure, high surface area and superior conductivity has

been successfully fabricated [27]. This CNTA-MnO_2 composite showed high capacitance (199 F g^{-1} and 305 F cm^{-3}) with a long cycle life (3% capacity loss after 20,000 charge/discharge cycles).

The capacitance for carbon-MnO_2 composite varies with preparation method. For instance, materials modified with a 1 nm thick film of MnO_2 prepared by a post-synthesis method, [30] retained its capacitance at much higher scan rates than the mesoporous carbons containing MnO_2 nanocrystals in the mesopore walls (one-pot synthesis) [29]. The former materials exhibited twice as large mesopores (~ 8 nm), compared to the latter composites. This feature implied lower electrolyte resistance and better diffusion in the materials with larger mesopores. Furthermore, similar oxide contents deposited on MWNT afforded thicker MnO_2 films (6 nm) [28] than on the surface of mesoporous carbons, resulting in better conductivity in the latter case at 100 mV s^{-1} scan rates [30]. While for MnO_2 - MWNT the gravimetric capacitance dropped from 350 F g^{-1} MnO_2 at 2 mV s^{-1} down to 37 Fg^{-1} MnO_2 at 100 mVs^{-1}, the capacitance approached 137 Fg^{-1} MnO_2 at 100 mV s^{-1} for the MnO_2 coated mesoporous carbon.

Nanostructured electrodes having ultra-high specific surface area as well as micropores comparable to the ionic size advances the performance of EDLC in recent days. Charge carriers such as room-temperature ionic liquids (RTIL) or organic electrolytes can further enhance the EDLC performance, especially in the field of the energy density and thermal stability [31]. The senon-aqueous electrolytes allow EDLC operation at a wider voltage window, thereby providing higher energy density. Interest has been growing to theoretically examine the interfacial structure and the electrokinetic behavior of electronic double layers (EDLs) consisting of ionic liquids (ILs) along with experiments to understand the characteristics of EDLC [32]. These simulation and theoretical studies have helped to elucidate phenomena related to electrochemical behavior in atomistic scale. The microscopic structures and changes in the pore size responsible for the drastic increase of capacitance in nanoporous electrodes have been investigated using these theoretical simulation studies. Few investigations have been devoted to understand the dynamics and transport behavior of RTIL in confined geometry and their connections with the unique microscopic details of EDLs. Though there are numerous reports on the equilibrium properties of RTIL-EDLs. Theoretical interpretation of the experimental cyclic voltammetry data are generally based on conventional equivalent-circuit (EC) systems. And also, microscopic electrokinetic theories are typically based on the systems containing ions in dilute aqueous solutions. On the other

hand, electrokinetics in RTIL systems has been distinctively different from the electrokinetics for aqueous electrolyte solutions. The conventional methods generally deals with macroscopic electrochemical phenomena and entail drastic approximations suitable only for macroscopic cases whereas RTIL-EDLs has showed its applicability from a microscopic perspective [31]. For an ionic liquid and nanoporous carbon, Péan et al. studied the supercapacitor charging dynamics based on molecular dynamics (MD) simulations [33]. It was found that the charging kinetics can be properly fitted with an EC simulation model. Also, for nanoporous materials ion transport is not much affected by the confinement. However, ion diffusion could be faster in ionophilic nanopores than that in the bulk for simulations of simpler models of ionic liquids and porous electrodes [34]. In addition, a diffusive process with "overfilling" at short time and "defilling" in the later stage has been found while charging EDL in RTIL. This kind of charging behavior cannot be properly explained with conventional EC models [34]. In this work, we investigate the behaviour of EDLC using MD simulations for a realistic model of RTIL but with nanostructured MnO_2 over graphene electrodes. The model system has been designed for fast equilibrium and better control of the temperature without compromising the essential features of EDL charging. We show that kinetics of EDL in ionic liquids severely depends on the positioning of co-ions and counter-ions near the electrodes. Unlike the predictions of conventional electrokinetic models, pore size and variation of the surface charge density are the main sensitive areas for RTIL-EDL.

2.2 Use of molecular modeling for EDLC design

Effective optimization of EDLC design is a significant challenge due to the complicated relationships between electrode and electrolyte properties, and their influence on the overall energy and power densities. Examples of design considerations include which pair of electrolytes should be used in combination with specific pore geometries and sizes [35]. If the anion and cation have different kinetic sizes under the charging–discharging conditions, then models for this kind of electrolytes need to be developed and the optimal pore size shall be different for the cathode and anode.[36] Organic solvents can be used to increase the electric conductivity of RTILs, [37] in which case the optimal electrolyte concentration needs to be determined. Polarization of the electrode can change local pore structure and geometry,[38] therefore the chosen electric potential needs to be carefully considered. Another optimization problem is the effect of pore size on the power density [39]. Nanopores with diameters close

to the ion diameter can increase the energy density of EDLCs,[40] however the power density can be limited due to high diffusion resistance imposed by the small pores. Furthermore, there are still significant areas where various EDL phenomena are not well understood. Examples include the influence of specific adsorption of ions to the electrode surface, [37] and the electro-kinetic and transport phenomena involving solvated ions in nanopores of varying geometries and sizes. [37] Chmiola *et al.* [41] conducted an experiment using carbide-derived carbon (CDC) electrodes with a narrow pore size distribution (PSD) and pore diameters less than 1 nm, and a $[TEA]^{+}[BF4]^{-}$ electrolyte in acetonitrile (AN). The experiment produced very high capacitance for an electrode with a pore diameter of about 0.7 nm, with volumetric energy twice as high as those of activated carbon electrodes. The observed anomalous capacitance behavior was also observed in a follow up experiment using Room temperature ionic liquids as the electrolyte [40] and challenged the long held belief that small pores were inaccessible to solvated ions. To explain the experimental observations, Huang *et al.*[42] developed heuristic models named the electric double-cylinder capacitor (EDCC) and electric wire-in-cylinder capacitor (EWCC), to describe EDL capacitance in cylindrical mesoporous and nanoporous electrodes, respectively. Merletet *et al.*[38] performed an accurate molecular simulation by accounting the polarization of the electrode by the electrolyte and managed to reproduce experimental results [40] quantitatively, giving realistic insights into ionic liquid structure inside nanoporous electrodes. Other molecular models have suggested an oscillatory pattern in which capacitance decays with increasing pore size [43]. The above modeling and simulation studies, as brief examples demonstrate some of the kind's contributions that molecular modeling can make to the field of EDLCs. Molecular modeling is essential for the design of optimal EDLCs. One of the greatest benefits of molecular modeling is the ability to predict phenomena that cannot be directly observed experimentally. For example, the spatiotemporal distribution and orientation of electrolyte ions, [44] and the change in morphology of electrodes due to polarization [38] are both important factors influencing the electrode capacitance but are difficult to measure experimentally. Thanks to simulations and accurate physical modeling, the intertwined impact of these variables can be understood and used to optimize the design of new EDLCs.

Molecular modeling can model the equilibrium and dynamic phenomena occurring in an EDLC in atomistic level. The force fields help to define the physics of molecular interactions in the simulation domain and the accuracy of molecular modeling depends largely on the validity of the force fields parameters used. The two most popular molecular simulation tools

are Monte Carlo (MC) and molecular dynamics (MD) [37]. Based on statistical mechanics, MC uses sampling to sample the phase space of a molecular system. The properties of the system are averaged over a large number of sampling steps to give ensemble averages which can be correlated to calculate thermodynamic and equilibrium structural properties.

MC simulations are limited to calculating equilibrium properties using statistical mechanics. For a short period of simulated time, MD simulations can solve Newton's equations of motion. The properties of the molecular system are averaged over this time to calculate the properties of the system. MD simulations have the advantage of also being able to predict dynamic properties, such as ionic diffusion.

In the development of molecular models, the selection of electrolyte and solvent models is a critical step that can greatly influence the accuracy and reliability of simulation results. Earlier simulations of EDLCs favored the use of primitive models that describe ions as hard spheres and electrodes as hard walls with solvents considered only as a dielectric constant, or with non-primitive models that consider solvent molecules as uncharged hard spheres [37]. The use of primitive models greatly reduces the simulation cost due to their simplicity, and may have previously been considered a necessary concession when computational resources were lower than what is generally available today. However, the accurate simulations using primitive models is greatly hindered due to lack of a realistic structure and inability to calculate dynamic electrostatic properties, specifically molecular dipole moments, which change with electrolyte polarization. All-atom electrolyte models, as the name implies, include every single atom within an electrolyte molecule, and are the most realistic models of electrolytes available. All-atom electrolytes are particularly useful models for studying specific molecular interaction, orientations, and overall structure within the EDL due to their accurate structure and polarisability. However, all-atom models have significantly high computational cost which limits their use, particularly in simulating large systems and RTILs, which require long simulation times to equilibrate, due to their high viscosities [45]. To overcome this computational limitation, simplifications can be made, such as using united-atom models, which unite CH_2 and CH_3 groups as single atoms, or using coarse-grained models, which group several sites of atoms together to represent them as a single pseudo-atom [45]. Coarse-grained models are of particular interest for simulating RTILs, which are bulky in size and often require large simulation box sizes with many hundreds of ions to minimize the finite size effect. Coarse-grained models can implement larger simulation time steps and simplified interactions, which can result in simulation times reduced by 100 times

when compared to all atom electrolyte model simulations [45]. Another critical step in the accuracy of molecular simulations of EDLCs is the selection of the electrode model, namely constant and uniform surface charges or polarisable electrodes with a constant potential where partial charges on electrode atoms fluctuate throughout the simulation [46]. Many researchers modeled electrodes with uniform surface charge to reduce the simulation times, and particularly in the earlier studies when techniques for electrode polarisability were not quite so well developed. Including electrode polarisability is important not only for the numerical difference it creates in simulation results, but also because it accurately represents a fundamental physical aspect that occurs in EDLCs which affects not only capacitance, but also dynamics. Electrode polarization enhances the surface charge in local areas via induced charges, which consequently increases the electric field strength and capacitance. Omitting polarisation of the electrode will result in artificially low capacitance when compared to experimental results. Another simulation technique that is used is based on quantum density functional theory (q-DFT) [47]. The q-DFT method solves quantum mechanical equations for a many-body system. In q-DFT, the number of particles involved in a simulation is generally far less than what is used in MC and MD simulations. Though q-DFT simulations cannot yet be extended to a realistic representation of a porous electrode due to the computational costs this simulation can be used as a complement to MC and MD simulations by validating force fields or other simulation results, such as the distance of the electrolyte ion from the surface of the electrode [37].

Classical density functional theory (c-DFT) simulation is the closest non-atomistic technique to MC and MD simulations. c-DFT simulations can be applied to describe EDLCs with porous electrodes by minimizing grand potential energy and obtaining local density profiles of solvent and electrolyte models, which can subsequently be used to determine EDL properties. Simulation times for c-DFT are far shorter than those of MD or MC. However, many important phenomena like surface roughness, polarization of the electrode surface, complex electrode geometry or ionic compressibility cannot be calculated using c-DFT. Often c-DFT is compared to MC simulations that make use of primitive models or non-primitive models to study various EDL structures as functions of ion size, the valency of electrolytes, and pore size [37]. These simulations are often compared against modified Poisson–Boltzmann theory and can demonstrate deviation from Gouy–Chapman–Stern behaviours [48]. However, they are of limited use in modelling realistic EDLC systems due to their simplification of ionic structure. Beyond this, c-DFT uses continuum modelling

which is an efficient approach for predicting capacitance and dynamics of EDLCs. Importantly, it allows one to systematically study the influence of many influential parameters, such as ion size, electrode geometry, and electric potential more easily than by using experimental methods [49]. However, continuum models cannot be used to predict capacitance in devices which employ nanoporous electrodes with pore sizes less than one nm and/or densely packed electrolyte molecules, such as in RTILs [50]. In these scenarios, which are becoming increasingly common in EDLCs, utilizing molecular simulations are favored for capacitance predictions due to their atomistic approach and ability to predict ion packing structure in the EDL.

2.3 Electrolytes for EDLC applications

Aqueous electrolytes, despite offering smaller energy density than organic solvent based electrolytes or RTILs (Room temperature ionic liquid) due to their lower electric potential window, still have attractive properties such as high relative permittivity, low ESR (Equivalent series resistance), low toxicity, and low cost. They are preferable to other electrolyte types in certain applications. It is also important to note that exceptional performance of EDLC can be achieved with aqueous electrolytes [51]. The extended simple point-charge model [52] was used to conduct equilibrium and non-equilibrium MD simulations of the transport of aqueous K^+Cl^- electrolyte in charged cylindrical nanoporous electrodes [53]. The surface of the electrode was modelled as smooth, and hydrophobic. The radius of the electrode was varied to investigate ionic confinement effects. It was found that strong confinement caused desolvation of ions, increased the influence of the external field on water molecule orientation, and decreased hydrogen bonding. Ionic conductivity was also found to decrease with decreasing pore radius.MD simulations were used to examine ion size effects in negatively-charged nanoporous (5,5) armchair CNTs with a diameter of 0.67 nm and a length of 1.1 nm interacting with Na^+, K^+, and Cs^+ cations in an aqueous solution. At zero surface potential, water molecules entered the CNTs in low concentrations and formed a single-layer wire down the centre of the CNT. At low negative surface charge densities, more water molecules were transferred into the CNTs with a preferred orientation, causing a low density area in the centre of the CNTs due to water-water molecule repulsion. At greater negative surface charge densities, it was thermodynamically favorable for cations to be partitioned into the pore. Interestingly, the medium-sized K^+ ions were found to have the least resistance to entering the pore, while the smallest Na^+ ions had the greatest partition

resistance. It should be noted that no anions were included in these simulations. In fact, anions may be present in weakly negatively-charged electrodes due to specific adsorption, which would drastically change the observed results. Feng *et al.*[54] used MD simulations to study the effect of slit type nanopore width on the distribution of K^+ ions and on the capacitance at a constant surface charge density. By examining long-range ion-ion interactions, non-electrostatic ion-electrode interactions, ion hydration, hydration water molecule-nonhydration water molecule interactions, and entropic effects, the authors were able to make several interesting observations. For pore widths between 1.0 and 1.5 nm, K^+ ions formed a well-hydrated single layer in the centre of the pores. Below 1 nm, the K^+ ions formed two separate layers near each slit wall. The transition from a single to a double layer was driven mainly by enthalpic effects between hydrated water molecules and the surrounding non-hydrated water molecules rather than by electrostatic interactions between ions. On the basis of these results, the authors suggested a 'sandwich model' describing the capacitance of single-layer ions in slit-type nanopores that is capable of predicting the anomalous increase in capacitance, [54]

$$C_{tot} = \frac{2A\varepsilon_r\,\varepsilon_0}{b-a_0} \tag{2.1}$$

where a_0 is the solvated ion diameter and b is the slit-pore width. It is important to note that the results from this study are not valid for systems with lower surface charge densities where anions would be included inside the pore. The authors considered a simulation of an aqueous *NaCl* solution to examine the energy penalty associated with partial desolvation of solvated ions entering a sub-nanometre pore [55]. Low free energy penalties were observed for both Na^+ and Cl^- ions and was attributed to van der Waals attractions between ions and pore walls, image charge effects, and strengthening interactions between ions and their solvation molecules inside the pore. MD simulations of aqueous *NaCl* solutions in contact with uncharged slit and cylindrical porous carbon electrodes in mesoporous and nanoporous regimes were used to study interfacial confinement effects and provide an atomic-scale depiction of ion transport dynamics [56]. Their simulations indicate that ordered layers form parallel to the surface of the electrodes and facilitate focused ion motion under confined conditions. This enhances ion diffusivity in the direction of the pore or slit. However, under increased confinement where the pore or slit size is reduced, the ionic diffusivity decreases. Similar MD simulations of aqueous NaCl electrolytes inside charged nanoporous graphene and slit-pore electrodes were performed by Kalluri *et al* [57]. Opposite sides of the pore walls were modelled as the anode and cathode. The electrolyte concentration, the surface charge

densities, and the pore diameter were all varied to study the structural properties of the aqueous electrolytes. At the highest surface charge density tested (+40 μC cm^{-2}) it was found that the ionic concentration inside the pores reached approximately 10 times the bulk concentration. Also at ± 40 μC cm^{-2}, it was observed that the Na^+ confined between electrodes (separated by 1.2 nm) approached the negatively charged grapheme surface more closely than the water molecules and partly lost their hydration shells. It was also found that multiple layers of adsorbed electrolytes formed near the electrode surface. This behaviour was similar to that observed by Wander *et al.*[56] and was attributed not only to electrostatic interactions but also to hydration phenomena and ion-ion correlations. Recent MD simulations considered a similar system, but included $CaCl_2$ solutions as well as $NaCl$ solutions to investigate ion size effects alongside the effect of nanopore width [57]. A schematic of the simulation cell is shown in Fig. no. 2.1. Maximum ionic densities inside the pore were dependent on the ion type and occurred at different pore widths for different ions. Analysis of the internal pore structure revealed that ion-ion correlations are only important for larger pore widths at low surface charge densities. In smaller pores especially, water-ion correlations are important for determining the correct distribution of ions. This is crucial for estimating the EDL thickness and the resulting capacitance. Aqueous electrolytes offer exceptionally high power density for EDLCs, yet their energy densities are often lacking. To compete with high energy densities offered by RTIL electrolytes, future simulations of EDLCs with aqueous electrolytes must have a focus on optimization of novel electrode materials, as opposed to the slit-type nanopores used in previous simulations.

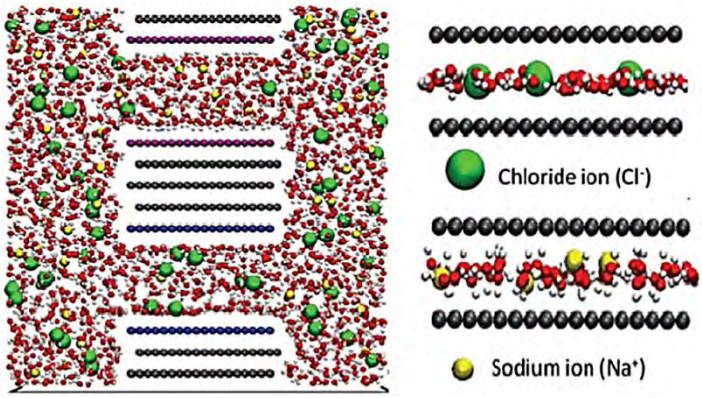

Fig 2. 1. Two-dimensional schematic of simulation box with yellow Na^+ ions, green Cl^- ions, red and white water molecules, black neutral carbons, blue positively charged carbons, and purple negatively charged carbons [37].

2.4 MnO_x based composites for supercapacitor applications

From the early report by Lee and Goodenough in 1999, [58] it has been claimed that MnO_x is a promising material for ES applications [59]. In general, manganese oxides (MnO_x) shows high theoretical capacities ranging from 1100 to 1300 F g^{-1} and it is relatively less costly, more environment friendly and less toxic [59]. Pseudocapacitance is the primary source of capacitance for manganese oxides. Reversible redox transitions which conducts the exchange of protons and/or cations with the electrolyte, as well as the transitions between Mn(III)/ Mn(II), Mn(IV)/Mn(III), and Mn(VI)/Mn(IV) attributes this pseudocapacitance [60]. The proposed mechanism is expressed in eqn 2.2: [59]

$$MnO_{\alpha}(OC)_{\beta} + \delta C^{+} + \delta e^{+} \leftrightarrow MnO_{\alpha-\beta}(OC)_{\beta+\delta} \quad (2.2)$$

Where C^{+} denotes the protons and alkali metal cations (Li^{+}, Na^{+}, K^{+}) in the electrolyte, and $MnO_{\alpha}(OC)_{\beta}$ and $MnO_{\alpha-\delta}(OC)_{\alpha+\delta}$ indicate $MnO_2.nH_2O$ in high and low oxidation states, respectively. The above-mentioned eqn 2.2 suggests that MnO_x material must have high ionic and electronic conductivity whereas in the redox reaction process both alkali cations and protons are involved [61]. Despite the clearly redox nature of the energy storage mechanism, MnO_x-based electrodes can also show non-faradic energy storage mechanisms which can demonstrate by typical rectangular-shaped cyclic voltammetry curves (Fig. no. 2.2 presents an example) [62]. As reported in the previous studies, both physical properties and chemical factors such as microstructure, surface morphology and valence, the hydrous state of the oxide, respectively, affect Mn oxides capacitive performance [59]. It was found that microstructure controls the cycle stability of Mn oxides while chemically hydrous state controls their specific capacitance [63].

2.4.1 Factors affecting the capacitance of MnO_x

Several physical and chemical factors that affect the capacitance of MnO_x electrodes:

(1) Crystallinity. High crystallinity has both positive and negative effects. It can give higher conductivity but loss of surface area can occur simultaneously. Crystallinity has direct impact on the protonation (or deprotonation) reaction and it will be limited if the crystallinity is too high in MnO_x.

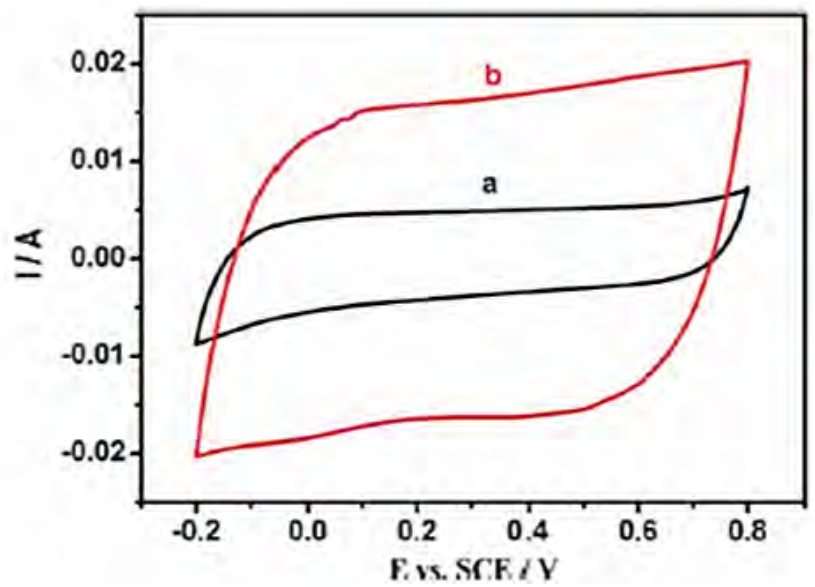

Fig 2. 2: Cyclic voltammograms of MnO_2-based electrodes in a 1 M Na_2SO_4 electrolyte at a potential scan rate of 5 mVs^{-1}. (a) MnO_2 obtained by using CNT and (b) MnO_2 obtained by using mesoporous carbon [59].

On the other hand, the electrical conductivity of MnO_x will be low for lower crystalline structure which can give highly porous microstructure. To achieve optimal conductivity, the annealing temperature plays an important role. When compared with those not heat-treated, MnO_x heat-treated at 200°C showed a lower specific capacitance at low scan rates and higher specific capacitance at high scan rates [64]. This phenomenon might be attributable to the fact that films treated at 200°C possess both lower open porosity and lower surface area. At a high scan rate, diffusion of H^+ and Na^+ ions is limited and some pores and voids become inaccessible. Obviously, excellent pseudocapacitive behavior can be obtained when Mn oxide is treated at an appropriate annealing temperature [65].

(2) Crystal structure. Crystallized MnO_2 materials have several crystalline structures, including α-, β-, γ-, and δ-MnO_2. Among them, α-, β-, and γ-MnO_2 have a tunnel structure (2 × 2 octahedral units for α-MnO_2, the relatively large tunnel structured phase; 1 × 1 octahedral units for β- MnO_2, the more compact and dense phase), and δ- MnO_2 has a relatively open layered structure (as shown in Fig. no. 2.3) [66].

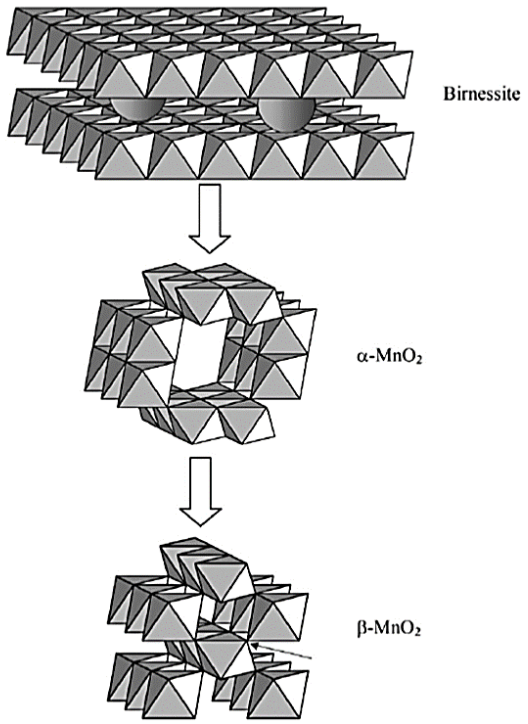

Fig 2. 3: Structural transitions of Manganese dioxide during material synthesis [66].

It has been recognized that different preparation conditions can occur in different MnO_x structures. For example, layered δ-MnO_2 can be prepared by increasing gradually the precursor acidity, through the relatively large tunnel structured phase α- MnO_2, to a more compact and dense β- MnO_2. The product from the process is mainly a δ- MnO_2 phase for NaOH or KOH solution. Electronic and ionic conductivity have been highly influenced by the structural changes in MnO_2, affecting the material's pseudocapacitive behaviour [66]. It was reported by Hua and Tsou [60] that an amorphous hydrous manganese oxide (α-$MnO_2.nH_2O$) fabricated from an $MnSO_4.5H_2O$ solution via anodic deposition showed a specific capacitance in the range of 265–320 Fg^{-1} for a potential range between 0 and 1.0 V using a 0.1 M Na_2SO_4 aqueous electrolyte solution. However, a specific capacitance of 168 Fg^{-1} at a potential scan rate of 1 mVs^{-1} has been shown by the nanostructured α-MnO_2 synthesized via a hydrothermal technique under mild conditions [67]. Single-crystal α-MnO_2 prepared by hydrothermal reaction of $KMnO_4$ under acidic conditions exhibited a specific capacitance of only 71.1 Fg^{-1} at a current density of 300 mAg^{-1} [68]. For γ-MnO_2 based materials, although one high specific capacitance of 240 $F g^{-1}$ at a current density of 1 mA cm^{-2} was reported [69], the majority of materials yielded specific capacitances of only 20–30 Fg^{-1} [70]. The two-dimensional layered structure of δ-MnO_2 can facilitate cation intercalation/deintercalation with little structural rearrangement [71]. Several methods for

synthesizing δ-MnO_2 have been developed. δ-MnO_2 obtained via a hydrothermal synthesis process exhibited a much higher specific capacitance than γ-MnO_2 and β-MnO_2.

(3) Morphology. The morphology of MnO_2 plays a determinant role in its electrochemical performance as it closely relates to the specific surface area and therefore the specific capacitance [72]. In the literature, prepared manganese oxides have many different morphologies, such as nanowires, nanorods, nanobelts, flower-like microspheres, nanobundles, and flower-like nanowhiskers [59]. Depending on the morphology, the obtained material's specific surface area can range from 20 to 150 m^2g^{-1}. Normally, the preparation process or reaction conditions control the morphology of MnO_x. Some morphologies of MnO_2 and their effects on specific capacitance are worth discussing here. The first is one-dimensional nanostructured MnO_x. Short transport/diffusion path lengths for both ions and electrons can be realized for one-dimensional nanostructured materials which leads to faster kinetics, offers large specific surface areas, and results in high charge/discharge capacities. For example, nanowires with smaller diameters can offer larger specific surface area for the access of electrolyte ions, more active sites for charge transfer, and short transport/diffusion distance for proton diffusion. That may be the reason why they have a higher capacitance of 350 F g^{-1} compared with nanorods' capacitance of 243 F g^{-1} [73]. Another example is one-dimensional nanobelt materials. They not only offer large electrode surface area and provide conducting pathways for ions, leading to high capacity and fast kinetics, but also better accommodate large volume changes, resulting in improved cycle performance for cathode materials. Based on the above and the literature, one-dimensional nanostructured materials with special morphologies and large surface areas are necessary for potential applications in ES.

(4) Thickness of the electrode layer. As the conductivity of MnO_2 is low, the specific capacitance decreases with increasing thickness of the electrode layer. For example, when the deposited loading of nanostructured MnO_2 was increased from 50 to 200 mg cm^{-2} the specific capacitance decreased from 400 to 177 F g^{-1}[74]. Some researchers have also pointed out that the thicker MnO_2 films deposited at higher potential are different from the thin films obtained at lower potentials. The difference between their specific capacitance can be as large as 100 F g^{-1} [75]. For instance, the specific capacitance of a MnO_2 layer prepared from the oxidation of $MnSO_4$ decreased from 220 to 50 F g^{-1} as the MnO_2 loading was increased from 4 mg cm^{-2} to 100 mg cm^{-2} [76]. Therefore, it is obvious that the thicker the film, the lower is the specific capacitance. The major benefits of thin layers can involve (i) lower series resistance due to

shorter transport paths for the diffusion of protons (low concentration polarization of the electrolyte), (ii) easy access of the electrolyte to the active surface of manganese dioxide, and (iii) higher electronic conductivity. Hence, high specific capacitance and rate capability can be achieved, especially when a thin MnO_2 layer is uniformly dispersed on conductive and porous carbonaceous materials with a high surface area. For example, Prasad and Miura [77] reported a thin amorphous MnO_2 film obtained by potentio-dynamic deposition that exhibited a specific capacitance of 482 F g^{-1}. When this thin layer was used for ES electrodes, high power density and stability were achieved. Most reported MnO_2 thin layers have exhibited specific capacitances as high as 600 F g^{-1} or more within a potential window of 0.9–1.2 V in aqueous electrolytes containing KCl, K_2SO_4, Na_2SO_4, or KOH [59].

(5) Specific surface area and pore structure. Normally, the specific capacitance of a metal oxide material will increase significantly as its surface area increases [78]. For example, a fibrous electrode has a high surface area and contains more active sites for redox reactions. At the same time, electrochemical polarization will be lower as the porous structure of the material can offer more channels for the electrolyte. And due to low electrochemical polarization, dissolution of Mn oxide will be minimum. Furthermore, high porosity has a positive impact to reduce the internal stress created during the charging and discharging processes which automatically act as a protecting system for the electrode from physical damage. Hence, the more fibrous or porous the oxide is, the better is the cycle stability [63]. Both the surface area and the pore-size distribution of MnO_2 electrode are major parameters to inhance the performance of supercapacitors. These parameters can be optimized by manipulating the reaction time and the surfactant content in the aqueous phase [79].

(6) Chemical factors. It is well established that transportation of electrolyte ions is highly beneficial using physically and chemically bound water. Thus, the loss of water can have negative impact on ion transport that means in speicifc capacitance. If the heat treatment temperature is too high, there will be loss of water as a result poor ion conductivity as well as loss of pseudocapacitance will occur [80]. For instance, it was reported that heat treatment at a temperature up to 200 °C could result in the removal of both physically and chemically adsorbed water [81]. There are also suggestion for optimizing the heat treatment to enhance overall pseudocapacitive behavior [82]. The Mn oxidation state is another very critical factor affecting the electrochemical performance of Mn oxides. Owing to the Jahn–Teller distortion of the $Mn(III)O_6$ octahedron, MnO_x involving trivalent Mn(III) shows a rather lower conductivity when compared with MnO_2 or amorphous manganese oxides involving Mn(IV)

[83]. Consequently, specific capacitance reduces due to the presence of Mn^{3+} which maybe synthesized via precipitation technique using $KMnO_4$ and various alcohols [84]. It was reported that when γ-MnO_2 was transformed to α-Mn_2O_3 and Mn_3O_4 by mechanical grinding, the specific capacitance decreased linearly as the amount of γ-MnO_2 decreased [83]. With respect to this issue, the literature also shows that MnO_2 exhibits much better performance than $Mn(OH)_2$, Mn_2O_3, and Mn_3O_4. [59] The factors mentioned above are all related to the MnO_x preparation processes and conditions. To improve Mn oxides' capacitive performance, developing more favorable preparation processes to optimize the microstructure, crystallinity, and the chemical state of Mn oxides should be an important approach. Several typical techniques reported in the literature are thermal decomposition, co-precipitation, sol–gel processes, electrodeposition, mechanical milling processes, and hydrothermal synthesis. Among these, the hydrothermal route has been proven to be an effective and controllable method to produce Mn oxides with various nanostructures such as nanowhiskers, nanoplates, and nanorods. [59] Note that the mechanical milling process can lead to a sequential phase transition from γ-MnO_2 to the thermodynamically stable α-Mn_2O_3 and subsequently to Mn_3O_4, depending on the duration of the mechanical grinding [83].

2.4.2 Challenges for Mn oxides

Though Mn oxides have shown high potential in the field of electrochemical capacitors, there are several challenges that must be addressed to make them usable in practice:

(1) Dissolution problem. Capacitance degradation is a problem for MnO_2 electrodes which occurs due to partial dissolution of MnO_2 in the electrolyte during cycling [70]. The dissolution reactions can be expressed as eqns. 2.3 or 2.4 [85]:

$$Mn_2O_3 + 2H^+ \rightarrow Mn^{2+}(aq) + MnO_2(s) + H_2O \quad (2.3)$$

$$2MnO(OH) \rightarrow Mn^{2+}(aq) + MnO_2(s) + 2OH^- \quad (2.4)$$

Several methods have already been implemented to prevent this dissolution problem of Mn oxides during cycling. For example, scientists have developed electrolyte salts that can avoid forming acidic species in solution [86]. Another method to prevent dissolution problem is to apply a protective shell to the Mn oxide surface. Babakhani and Ivey [87] prepared a Mn oxide/CP coaxial core/shell electrode. Mn oxide rods were first synthesized through anodic deposition from an Mn acetate solution, and then were coated using electro polymerization of a conducting polymer to yield coaxial rods. The presence of a conducting polymer suppresses the dissolution of Mn oxide and improves its resistance to failure, leading to both enhanced capacitance and high cycling rate capability.

(2) Low surface area. Low surface area of MnO_x material is another concern for its use as a supercapacitor. To improve these, several approaches have been carried out in ES material development. For example, a large surface area can be achieved by introducing multilayered film electrodes containing transition metal composite materials [88]. In this way, the formed Mn oxides have high electrochemical activities, leading to excellent electrochemical capacitance and long cycling durability. Besides this method, doping shows positive impact for MnO_x to improve the surface area hence the capacitance. For example, in a nanostructured nickel–manganese oxide composite, surface area and specific capacitance of Mn oxide increases by 46% and 37% respectively due to nickel doping. Adding Co into MnO_x or surfactant component such as sodium lauryl sulfate or Triton X-100, increase in the surface areas of MnO_x materials [89]. In addition, hierarchical hollow nanospheres of MnO_x yielded a specific surface area of 253 m^2 g^{-1}. To address the issue of enhancing manganese oxides' poor electrical conductivity, doping with ruthenium, nickel, and Mo seems to be helpful. In addition to doping, highly conductive supports such as active carbon, CNTs, graphite, and conducting polymers have also been utilized to support manganese oxides in an attempt to promote their conductivity [59]. In reality, both the electrical conductivity and active surface area of MnO_x increases due to the presence of conductive supports. Using a supporting strategy, maximum benefit of MnO_2 dispersion over electrode surface can be attained. By dispersing over a large area, MnO_2 can prevent its further growth by agglomeration. Also, using these highly active materials on electrode surface improved double-layer capacitance can be achieved. The most important feature of the supporting strategy is that these conductive supports can form a three-dimensional porous conducting network to effectively assist electron transfer and ion transport within MnO_x [59]. For instance, a rectangular shape in a cyclic voltammogram and a volumetric specific capacitance of 253 F cm^{-3} can be obtained from a manganese oxide/carbon composite electrode. Mn oxide/CNT composite electrodes reached a specific capacitance of 415 Fg^{-1} because CNTs were able to provide electronic conductive paths and form a network of open mesopores [59]. Li *et al.* [90] reported that when MnO_2 particles were partially coated on the surfaces of MCNTs through a hydrothermal process, a specific capacitance of 550 Fg^{-1} was obtained. The MnO_2/C composite electrode also exhibited highly stable performance up to 10000 cycles. In addition, composites with a single-walled CNT support showed excellent cycling capability even at a high current of 2Ag^{-1}[59]. In summary, to achieve high energy and power densities for ES, MnO_x based electrode materials can be modified through depositing MnO_x

onto carbon materials with high surface areas, highly ordered mesopores, and high electrical conductivity, which can then yield high specific capacitances. However, it should be noted that the specific capacitance of the composite electrode can be compromised by the low faradaic reaction activity of the conductive supports.

(3) Poor ionic conductivity. The poor ionic conductivity of Mn oxides is another challenge that hinders their practical application in ES [81]. To improve their ionic conductivity, great effort has been invested into nanostructured MnO_x materials. For example, MnO_2 electrode with multilayer and macropore surface shows excellent capacitive behaviour with high retention of a rectangular shape during charging/discharging as the interlayer spacing and pore structure yielded high ionic conductivity [62]. In addition, a nanoscopic MnO_2 phase can minimize solid-state transport distances for ions going into the oxide. For example, Mn oxide nanowire arrays with high aspect ratio and high surface area, prepared on anodic aluminium oxide templates, displayed a specific capacitance of 254 Fg^{-1} [91]. A uniformly dispersed fibrous manganese oxide electrode, which had a unique nanoporous structure, was able to deliver a high specific capacitance of 502 Fg^{-1} and excellent cyclic stability [92]. This is because the high porosity structure enhanced electrolyte accessibility, promoting ionic transportation within the electrode, kinetic reversibility, and electrochemical reaction homogeneity.

2.4.3 Recent developments

In the recent years, considerable research is going on how to incorporate MnO_2 in electrodes to improve the performance of supercapacitors. Nanostructured MnO_2 and MnO_2 composites, and even asymmetric ES, have been studied which are described below.

(1) Nanostructured MnO_2. Intensive investigation for Nanostructured MnO_2 materials have been occurring in the recent years [59]. Nano-MnO_2 can exhibit an electrochemical performance superior to its bulk counterpart because it possesses higher specific surface area and the short transport/diffusion path lengths of ions and electrons. Some single-crystal α-MnO_2 nanotubes [93], which were synthesized by a hydrothermal method without the assistance of templates, surfactants and heat-treatment, could possess a high specific capacitance. α - MnO_2 nanowires with a diameter of 30 to 40 nm and mean pore diameter of 3.1 nm could give a specific capacitance of 466 Fg^{-1} and high cycling efficiency as well at a current density of 10 mA cm^{-2} [59]. α - MnO_2 nanorods with a diameter less than 50 nm showed good cycling stabilities and could deliver a maximum capacitance of 166.2 Fg^{-1}. [94] Nano-structured MnO_2 can be prepared from the reduction of $KMnO_4$ which can be done by

alcohols or by structure-directing agents. For example alcohols such as methanol and ethanol [84], ethylene glycol [95], KBH_4, fumaric acid can be used and as a structure-directing agent Pluronic P123 can be used [96]. However, complicated operations, time/energy-consuming and expensive reagents seemed to be serious obstacles for the industrialization of nano-MnO_2. That is why further research is needed to develop simple and cost-effective processes.

(2) MnO_2 composite materials. In addition to nanostructured MnO_2, the combination of MnO_2 with other materials such as graphite and CNTs has also been investigated extensively [97]. The introduction of other materials into MnO_2 can improve the electron conductivity of the electrode, extend the working potential, and guarantee an effective utilization of MnO_2 [98]. As a result, the composite electrodes can display higher specific capacitances, higher energy and higher power densities. Graphene–MnO_2 composites (78 wt% MnO_2), which were prepared by redox reaction between graphene and potassium permanganate under microwave irradiation, displayed a specific capacitance as high as 310 Fg^{-1}at 2 mV s^{-1}, which is almost three times higher than that of pure graphene (104 Fg^{-1}) and birnessite type MnO_2 (103 Fg^{-1}). The improved electrochemical performance might be attributed to the increased electrode conductivity in the presence of graphene network, the increased effective interfacial area between MnO_2 and the electrolyte, as well as the contact area between MnO_2 and graphene.[59] With respect to CNT composite materials, most of the reports dealt with non-aligned and disordered CNTs. Compared to non-aligned CNTs, aligned CNT-based electrodes could show advantages such as low contact resistance, large specific surface area, and fast electron transfer kinetics [59]. For example, Amade *et al.* [99] prepared a nanostructured composite electrode with dense, long and vertically aligned CNTs (with high specific surface area), coupled with a thinner layer of MnO_2 by optimizing the CNT preparing parameters and electrode position processes of MnO_2. A specific capacitance of 642 Fg^{-1} [99], much higher than that of activated carbon/MnO_2 electrodes [98], was obtained at a scan rate of 10 mVs^{-1}. This high capacitance was mainly attributed to CNT's high surface area and conductivity [99]. To simultaneously achieve both high energy and power densities, one of the challenges is to optimize the mass proportion of the composite [98].

(3) Asymmetric cells. Recently, coupling of asymmetric cells with electrodes operating reversibly in different potential ranges have been presented as a promising way to increase voltage in aqueous electrolyte, leading to high energy density. For example, as reported by Gao *et al.*[100], a hybrid electrochemical supercapacitor consists with activated carbon as the negative electrode and a composite of activated carbon and MnO_2 as the positive electrode.

The best performance for asymmetric actived carbon-MnO_2 supercapacitor was obtained with R = 2.5 and V (cell voltage) = 2 V, by optimizing the mass ratio (R) between the positive and negative electrodes allowing the maximum potentials for both electrodes to be close to the acceptable stability values [59]. However, it is a challenge to design a positive electrode with enhanced capacitance according to the following formula to reduce the R value. Eqn. 2.5 is based on the equivalence of charge passed through both electrodes.

$$R = \frac{m_+}{m_-} = \frac{C_- \times \Delta E_-}{C_+ \times \Delta E_+} \tag{2.5}$$

where C_+ and C_- are the specific capacitances, E_+ and E_- are the potential windows for the positive and negative electrodes, m_+ and m_- are the masses of the electrode materials respectively.

CHAPTER 3

Experimental Method

The experimental section in the present study consists of preparation of rGO-MnO_2 in the laboratory and characterizing the synthesized material using Field Emission Scanning Electron Microscopy (FESEM), Energy Dispersive X-ray Spectroscopy (EDX), X-ray Diffraction Spectroscopy (XRD). Electrochemical capacitive behaviour was investigated using Cyclic Voltammetry (CV) and Chronopotentiometry (CP) experiments. The corresponding experimental method has been demonstrated in this chapter.

3.1 Synthesis procedure

3.1.1 Synthesis of GO and rGO

GO was prepared from purified natural graphite powder according to the Modified Hummers method [101]. Graphite powder (1.0 g), $NaNO_3$ (0.5 g) and $KMnO_4$ (3.0 g) were slowly added to a concentrated H_2SO_4 solution (23 ml) within an ice bath. The above-mentioned mixture was properly stirred for 30 min at 35±3 °C after removing the ice bath. After the reaction was completed, the mixture was mixed with deionized water (46 ml) keeping the temperature at 98°C for 15 min. Then the temperature was reduced to 60°C with the addition of warm deionized water (140 ml) and H_2O_2 (30%, 10 ml) and it was stirring continuously for a period of 2 h. The obtained mixture was filtrated to collect the solid product. After that the mixture had been washed with 4 wt.% HCl solution for 5 times and then with deionized water so that neutral p^H of the supernatant had been obtained. Finally, a loose brown powder had been obtained by drying the material in vacuum. The process of preparing Graphene (rGO) from GO involved reducing the material with 5ml NH_4OH and 6ml hydrazine solution and heating in an oil bath at 95 °C for 2 h. After the reaction, the dispersed graphene was filtered and the collected solid was washed several times with deionized water and finally dried at 80°C in an oven under vacuum.

3.1.2 Synthesis of rGO-MnO_2

rGO-MnO_2 was synthesized by in situ chemical reduction of $KMnO_4$ using benzyl alcohol which was initially anchored to rGO in an aqueous suspension [102]. In brief, 80µL benzyl alcohol and then 360 mg rGO is added into 25 mL DI water under mild stirring condition.

The hydrophobic benzyl alcohol was adsorbed on the surface of rGO through ultrasonic treatment for 30 min.60 mg $KMnO_4$ was added into the above solution and kept on mild stirring for 10 h. In neutral or weak alkaline reaction medium, MnO_4^- could be reduced into MnO_2, which involved the following redox reaction. In this process, the benzyl alcohol acts as a linker between RGO and MnO_4^-, and also serves as a sacrificial reductant to reduce the aqueous MnO_4^- ion into insoluble MnO_2 on the surface of rGO.

3.2 Experimental Set-up

The present experimental study has been conducted in the Nanochemistry Research Laboratory, Department of chemistry and Scanning Electron Microscope (SEM) facility, X-Ray Diffraction (XRD) facility at Department of Glass and Ceramic Engineering (GCE), Bangladesh University of Engineering and Technology (BUET). The major lab facilities for characterizing the prepared samples used in the present study include:

3.2.1 Field Emission Scanning Electron Microscopy (FESEM)

FESEM is an advanced tool which is the upgraded form of scanning electron microscope (SEM). This tool is used to examine various properties of materials such as external morphology (texture), crystalline structure and materials orientation in the sample [103]. The term 'SEM' is substituted by 'FESEM' with the use of Field Emission GUN (FEG) instead of

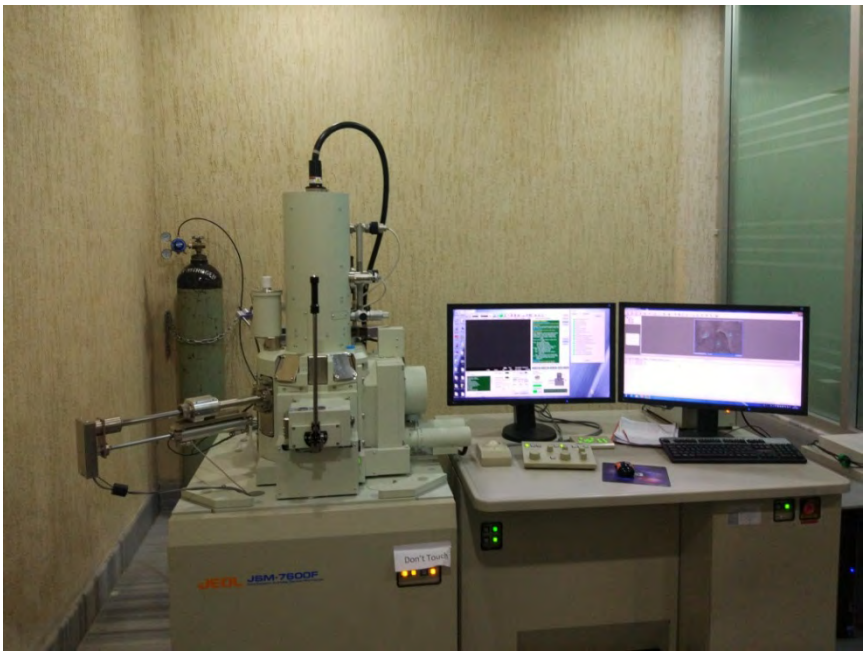

Fig 3. 1: Scanning Electron Microscopy (SEM) setup at Department of Glass and Ceramic Engineering (GCE), BUET.

Thermionic Emission Gun (TEG) as electron emitter gun. In this method, highly energized electrons from a focused beam have been used to generate a variety of signals at the solid surface of specimens.

Among the signals, two of them are commonly used for imaging samples-secondary electrons and backscattered electrons. To show the morphology and topography on samples, the most valuable is secondary electrons. On the other hand, composition in multiphase samples can be determined using backscattered electrons by illustrating contrasts.

In most applications, data are collected over a specific position of sample's surface, which is our point of interest. A two-dimensional black-white image is generated for these positions which will display the spatial variations in properties. Typical SEM method can be used to image areas ranging from approximately 1 cm to 5 microns in width whose spatial resolution can be 50 to 100 nm whereas can magnify objects from 20X to 500000X, approximately.

Advantages of SEM include its wide-range of applications, the versatile information garnered from different detectors and imaging that includes detailed topographical and two-dimensional view. Operation of SEM instrument is easier with the proper training and advances in computer technology and associated software has made operation user-friendly.

3.2.2 Energy Dispersive X-ray Spectroscopy (EDX)

Energy Dispersive X-ray Spectroscopy (EDX), which is also called EDS, is a micro analysis technique used to identify the elemental composition and in chemical characterization of materials. EDX systems are commonly used in conjunction with Electron Microscopy instruments (Scanning Electron Microscopy (SEM) or Transmission Electron Microscopy (TEM)), where the specimen of interest can be identified using imaging capability of the microscope [104].

When the SEM's electron beam bombarded the sample, atoms are excited and eject electrons from the sample's surface. Electrons from a higher state filled the electron vacancies due to bombardment. Therefore, as a result, x-ray emission occurs to stabilize the unbalanced energy between the two electrons' states. The x-ray energy being characteristic of the element from which it was emitted, identity of elements and their relative abundance can be marked by detecting this x-ray radiation.

EDX offers the advantages of quick, ‘ first look’ compositional analysis. Within a few seconds, a user can have full elemental spectrum using the "spot" mode. Software developed to support the experiment, makes it possible to easily identify peaks. As a result, it is possible to identify unknown phases before quantitative analysis which makes EDX a great survey tool. EDX can also be used for calculating chemical composition by comparing the peak-height ration with a standard.

3.2.3 X-Ray Diffraction Spectroscopy (XRD)

XRD is one of the most powerful, reliable, non-destructive techniques for the qualitative and quantitative analysis of the crystalline materials, in form of powder or solid.

XRD is based on a crystalline sample and constructive interference of monochromatic X-rays. Cathode ray tubes are used to generate X-rays and then these rays are filtered to produce monochromatic radiation. Then they are collimated to concentrate and directed toward the sample. By satisfying Bragg's Law, the interaction of the incident rays with the sample produces constructive interference (and a diffracted ray). This law relates the electromagnetic radiation’s wavelength to the diffraction angle and the lattice spacing in a crystalline sample [105].

These diffracted X-rays are then detected, processed and counted. Diffraction directions of the lattice can be occurred by random orientation of the powdered sample, all of them are attained by scanning the sample using a range of 2θ angles. As a set of unique d-spacing is available for each mineral, converting the diffraction peaks to d-spacing gives identification of a mineral. Typically, standard references patterns are used to compare with d-spacing achieve the mineral. The value of d-spacing is obtained from Bragg’s law-

$$2d \sin\theta = n\lambda \qquad (3.1)$$

Fig 3. 2: X-Ray Diffraction Spectroscopy (XRD) setup at Department of Glass and Ceramic Engineering (GCE), BUET.

Where, d is inter-layer spacing, θ is the x-ray angle of incidence (and of diffraction) measured with respect to the crystalline planes, n is an integral value and λ is the wavelength of incident beam.

Crystallite size of crystals are calculated from Scherrer formulae-

$$D = k\lambda / \beta\cos\theta \qquad (3.2)$$

Where D is the crystallite size, k is a shape factor which is dimensionless (typical value 0.9), l is t he x -ray wavelength, β is the line broadening at halfway of the maximum intensity (FWHM) and θ is the Bragg angle (in degrees).

Successful XRD analysis depends largely on proper sample preparation. Typically, samples are grinded to achieve a good S/N ratio, avoid spottiness and minimize preferred orientation. The ideal samples are crystalline powders.

XRD offers many advantages over other available techniques in sample analysis. One of the main advantages is that it is relatively straight forward and easy to analyze and interpret data

in XRD. It acts as a powerful technique to identify an unknown mineral as this method requires very small amount of sample and can provide an unambiguous mineral determination.

3.2.4 Cyclic Voltammetry (CV)

CV is an electro-analytical technique based on the electric current response of a material as a function of potential [106]. In this method, the input parameter is potential of working electrode and the output parameter is the current from the system. By cycling the working electrode potential, current is measured from the experimental domain. It is the modern form of polarography, developed by Jaroslav Heyrovsky in 1922. In the CV experiment, scanning is performed from a starting potential to a final potential which is known as the switching potential for an immersed, stationary electrode. After that, the reverse scan is performed for the same potential range. This gives a 'cyclic' sweep of potentials which can be repeated as per interest. The cyclic voltammogram (CV) curve us defined by the current vs. potential curve derived from the data. The potential extreme ends are termed the 'scan window' whereas first sweep is called the 'forward scan' and the return wave is called the 'reverse scan'.

(a)

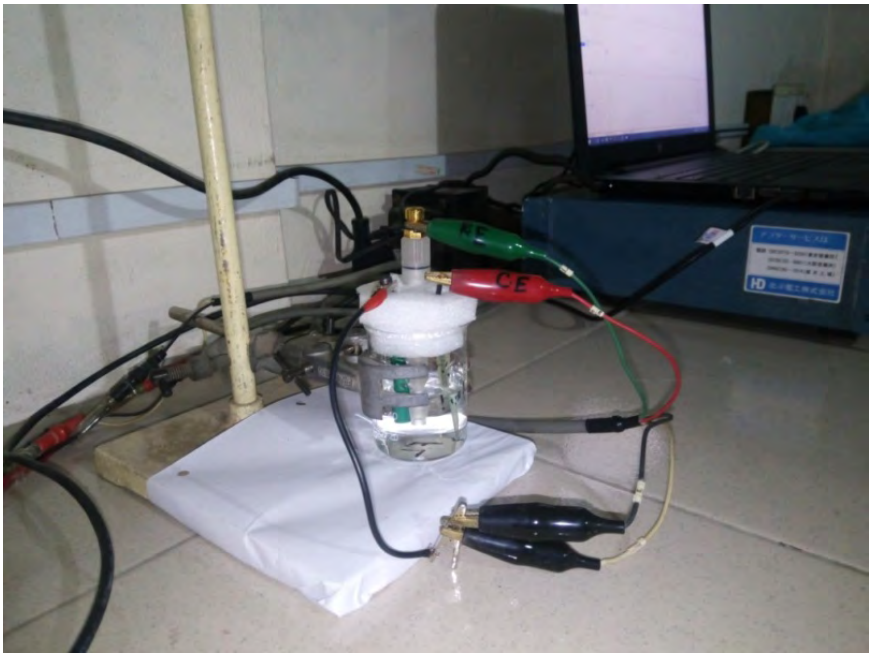

(b)

Fig 3. 3 : Experimental setup of Cyclic Voltammetry and Chronopotentiometry at Advanced Research Laboratory, Department of Chemistry, BUET (a) the control panel for applying voltage and current, and (b) the three electrode setup for experiment.

When potential is allowed to increase, initially current response is defined as capacitive, originating from electrical double layer (EDL) formed at the electrode surface involving diffusion-controlled process. When the potential approaches a specific value favoring the reduction of the active material, current response increases rapidly resulting in an anodic peak and the corresponding current and potential are called anodic peak current and anodic potential. Then current falls off as the maximum rate of mass transfer has been reached and goes down only to reach equilibrium at some steady value. A similar but opposite peak current may be observed when potential meets a value favoring oxidation of the reduced species during its return tour to the initial value.

$$\mathbf{R} + \mathbf{e}^- \leftrightarrow \mathbf{O} \tag{3.3}$$

Current responses from redox reaction are termed as faradic current while the remaining responses are usually attributed to EDL and called non-Faradic current. Thus, the capacitive window of a material can be easily identified from the absence or presence of redox peak in its CV [6].

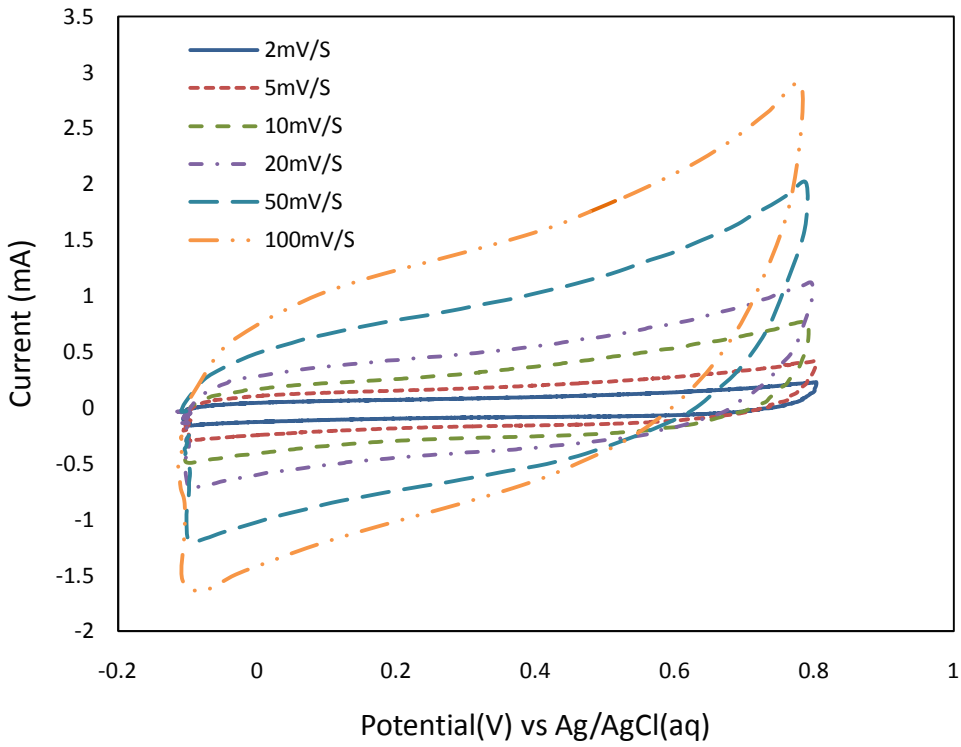

Fig 3. 4: Variation in current response of a material with different scan rates.

One important feature of CV is that, the total current increases with increasing scan rate. The scan rate is expressed as the rate of change of potential with time. The size of the diffusion layer and also the time taken to record the scan can be used to rationalize it.

Analyte natures, concentration, scan rates and experimental conditions are the main features that can vary the magnitude of current response and the shape of the voltammograms. By varying these factors, cyclic voltammetry can yield information regarding dependency of the process, the stability of transition metal oxidation state in the complex form, reversibility of electron transfer reactions, reactivity of active material etc.

3.2.5 Chronopotentiometry (CP)

Chronopotentiometry (CP) is the most widely used constant current experiment. It is an electro-analytical technique in which an unstirred solution of an electroactive species, in presence of excess of a supporting electrolyte, is electrolyzed at a programmed current density between an indicator electrode and a counter electrode and the potential-variation of the former *vs.* a suitable reference is recorded as a function of time [107]. The resulting graphs are current excitation signal and potential response as a function of time.

It is possible to identify the nature of electrode material from the CP. e. g. the potential response of an ideal capacitive material in CP shows discharge/ charge time to be ~ 1 and can be easily marked.

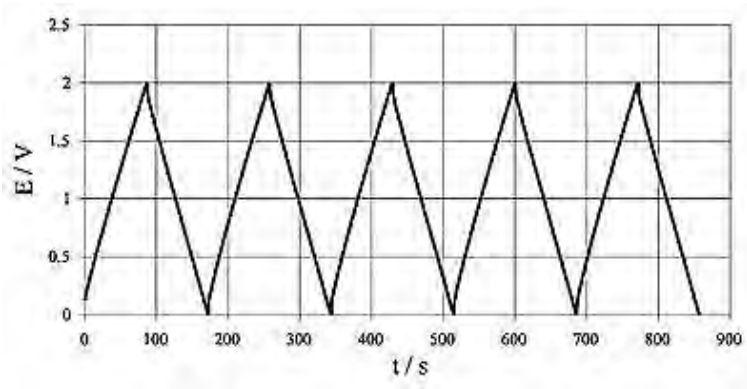

Fig 3. 5: Potential response of an ideal electrochemical capacitor in CP. [108]

The specific capacitance of an electrochemical capacitor can be easily calculated from its potential response in CP on the basis of the relationship-

$$C_{sp} = \frac{i\Delta t}{m\Delta V} \tag{3.4}$$

Where, C_{sp} is the specific capacitance, I is discharge current (cathodic current), m is the mass of active electrode material, Δt is the total time of discharge and ΔV is the potential drop during discharge.

CHAPTER 4

Computational Method

Computational Analysis is used to reproduce the characteristics of a system using a well-established mathematical model. There are several cases where it is difficult to obtain information directly from experiments. Computer models can provide accurate information with fewer difficulties in these cases. The "force field" plays an important role to determine the accuracy of these simulations. The force field parameters actually emulate the underlying physics and describe how the energy of the molecule responds to various events needed for function. In many cases, they imply a considerable amount of simplification in order to eliminate all the complexities invariably associated with real world problems, and make the problem solvable.

4.1 Molecular Dynamics Simulation

The computational analysis of the present study involved Molecular Dynamics simulation which was performed by using Large-scale Atomic/Molecular Massively Parallel Simulator (LAMMPS). Here, molecular dynamics simulations have been performed to explore the impact of a solvent (water) and an ionic liquid electrolyte (NaCl) on the structural and capacitive properties of electrochemical supercapacitor based on graphene-MnO_2 electrode.

4.1.1 Molecular Dynamics Simulation: Large-scale Atomic/Molecular Massively Parallel Simulator (LAMMPS)

Molecular dynamics (MD) is a computer simulation technique which operates by integrating equations of motion for a set of atoms simulating with respect to time.

In molecular dynamics, the classical mechanics laws, and most notably Newton's law are followed:

$$F_i = m_i a_i \tag{4.1}$$

For a system of N atoms, i indicate each atom in it. Here, m_i is the atom mass, $a_i = {d^2 r_i}/{dt^2}$ its acceleration, and F_i is the force acting upon the atom due to the interacting atoms.

Molecular dynamics is a deterministic technique, which gives an initial set of positions and velocities, the subsequent time evolution is in principle completely determined. Atoms will act in a pretty similar way they act in real substance. For instance, atoms in the simulation domain will interact with each other by moving, bumping, wandering around and oscillating in waves in concert with their neighbors. Even some atoms will evaporate from the system if there is a free surface and so on.

LAMMPS operates as a classical molecular dynamics tool which mainly uses on materials modeling. It is distributed as open source code by Sandia National Laboratories, a US Department of Energy laboratory using the GPL terms and conditions. LAMMPS has potentials for several fields on material science. For example, solid-state materials like metals, semiconductors and soft materials like biomolecules, polymers and also coarse-grained or mesoscopic systems can be studied using LAMMPS. It can be used for all atomic, meso or continuum scale not only to design atomic model but also for parallel simulation of particles. LAMMPS runs on single processors or in parallel using message-passing techniques. Spatial-decomposition of the simulation domain is applied while running this application. One of the benefits of using LAMMPS is that the code designed and used can be easily modify or extend with new functionality [109].

4.1.2 Modeling the Physical System

The main ingredient of a simulation is a model for the physical system. For a molecular dynamics simulation, this amounts to choosing the potential: a function V (r_1, ……, r_N) of the positions of the nuclei, representing the potential energy of the system when the atoms are arranged in that specific configuration. This function is invariant for the translation and rotational motion. It is usually constructed from the atoms relative positions in the simulation domain.

Forces are then derived as the gradients of the potential with respect to atomic displacements:

$$F_i = -\nabla_{r_i} V(r_1, \dots\dots\dots, r_N) \tag{4.2}$$

This form implies the presence of a conservation law of the total energy E = K + V, where K is the instantaneous kinetic energy.

The simplest choice for V is to write it as a sum of pair-wise interactions:

$$V(r_1, \dots\dots\dots, r_N) = \sum_i \sum_{j>i} \emptyset(|r_i - r_j|) \tag{4.3}$$

The clause j >i in the second summation has the purpose of considering each atom pair only once. Pair wise interactions were only parameter to constitute most potentials in the past which is changed now. Also, performance of two-body approximation is very poor for many relevant systems i.e. metals and semiconductors. Now-a-days, for condensed matter simulation several kinds of many-body potentials are in use.

4.1.3 The Lennard-Jones Potential

The Lennard-Jones (LJ) 12-6 potential [110] is given by the expression

$$\emptyset(r) = 4\varepsilon\left[\left(\frac{\sigma}{r}\right)^{12} - \left(\frac{\sigma}{r}\right)^{6}\right] \tag{4.4}$$

for the interaction potential between a pair of atoms.

This potential has an attractive tail at large *r,* it reaches a minimum around 1.122σ, and it is strongly repulsive at shorter distance, passing through 0 at r = σ and increasing steeply as *r* is decreased further.

At short distance, the term ~ $1/r^{12}$ dominates and models the repulsion phenomena between atoms when they are brought very close to each other. Pauli principle can give the physical explanation of this: the energy of a system can be modified by the atoms position. When atoms come closer so that the electronic clouds start to overlap, the energy of the system increases drastically. The exponent of the distance, *r* has been chosen on a practical basis. The Lennard-Jones equation is particularly convenient to compute and also on physical grounds an exponential behavior would be more appropriate.

The cohesion phenomena of the system are reflected by the $1/r^6$ term which dominates at large distance. Due to actuating dipoles, dipole-dipole interactions occur which generates the van der Waals dispersion forces and in the LJ potential $1/r^6$ attraction is originated by van der Waals forces. As the interactions are weak it generally dominates for closed-shell systems i.e. rare gases such as Ar or Kr. To fit the physical properties of the material, parameters like ε (depth of potential wall) and σ(finite distance at which the inter-particle potential is zero) are implemented in this potential.

On the other hand, the two-body interactions scheme itself fails for simulation model with open shells and LJ potential is adequate to operate this simulation physics. Phenomena like strong localized bonds (in covalent systems), delocalized “electron sea” (in metals) cannot be performed by physics of LJ potential.

However, the LJ 12-6 potential is an extremely important model system now-a-days to study varieties of geometries like solids, liquids, surfaces, clusters, two-dimensional systems etc. It can be said that to investigate the fundamental issues instead of studying specific properties of material, LJ is the standard potential to use. The research works done on LJ systems is helping in various fields to understand the basics such as in condensed matter physics. So, it can be said that the importance of LJ parameters has already been proved.

In practical applications, a cutoff radius R_c has to be defined and atoms interactions are separated by this cutoff radius in the simulation process. The benefit of this cutoff radius us that is saves computational as the number of atomic pairs separated by a distance r grows as r^2 and it can be large within a small period of time.

A simple truncation of the potential creates a new problem though: whenever a particle pair "crosses" the cutoff distance, the energy makes a little jump. This can spoil energy conservation in a simulation if this happens several times. To avoid this problem, the value of potential for a distance that is lower that cutoff radius:

$$V(r) = \begin{cases} \emptyset_{LJ}(r) - \emptyset_{LJ}(R_c) & if r \leq R_c \\ 0 & if r > R_c \end{cases} \tag{4.5}$$

Physical quantities are of course adversely affected by the potential truncation. This truncation effect of a full-ranged potential can be approximately predicted by assuming the simulation domain as a uniform continuum beyond R_c. For example, there is some additional contribution to the cohesive energy as well as to total pressure by the potential tail (attractive). Truncation effects depend on several factors and are not so easy to estimate. For example, it is difficult to estimate the truncation effects for geometries with free surfaces and where there is lower symmetry in the system.

4.1.4 Periodic Boundary Conditions (PBC)

Periodic boundary condition (PBC) is used to eliminate the surface effects in molecular dynamics simulation. An infinite lattice can be created in PBC using cubical simulation box which will replicate itself throughout the space. In this infinite lattice, movement of molecules is same in all boxes. For example, if a molecule moves in the central box, all the molecules in every other box moves with exactly the same orientation because of periodic image consideration. Also, when molecule moves out from the central box, there will be one of its images in the box which will enter through the opposite face. In PBC system no surface exists and there are no walls at the boundary. Fig. no. 4.1 shows a three-dimensional version of a typical periodic system. From the figure, according to the above-mentioned principle as a

particle moves through a boundary, there are corresponding images of that particle who move across their corresponding boundaries. The number of particles in the central box is fixed which indicates that particles in the entire system are conserved. In our study, we selected p p f (Periodic, Periodic, Non-periodic and fixed) boundary condition as we incorporated Verlet Algorithm with Particle-Particle Particle-Meshstyle (PPPM).

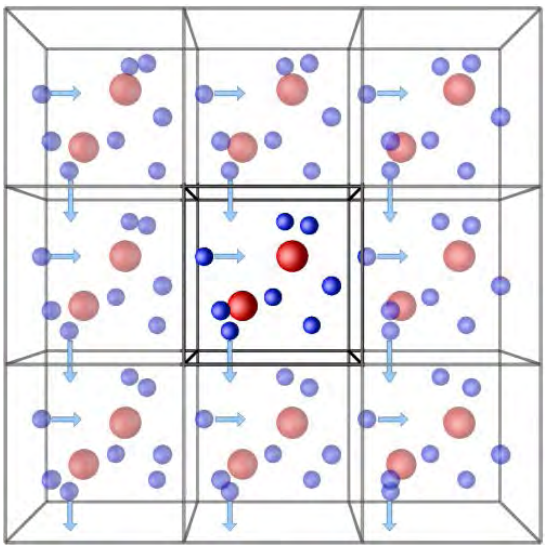

Fig 4. 1: Periodic boundary conditions (The central box is outlined by a thicker line) [111]

4.1.5 Time Integration Algorithm

Time integration algorithm acts as the engine of molecular dynamics simulation. It operates by integrating the equation of motion of the interacting particles and follows their trajectory of motion. Finite difference methods are the basis of this algorithm. Firstly, using the finite grid network time is discretized where the time step Δt is defined as the distance between consecutive points on the grid. Then, the integration scheme provides the position and some of their time derivatives at a final time $t+\Delta t$ by applying the known the data at time t. This process can run for long times by iterating the procedure with respect to time evolution.

There are several popular integration algorithms for MD calculations i.e. Verlet algorithm, predictor-corrector algorithms etc. In this study, Verlet style has been applied which is a standard velocity-Verlet integrator that works with PPPM style.

4.1.5.1 The Verlet Algorithm

In molecular dynamics, Verlet algorithm is defined as the most popular time integration algorithm [112-113]. Here, third-order Taylor expansions for positions r(t) form the basic algorithm .There will be total two equations containing one forward and one backward in

time. Calling *v* the velocities, *a* the accelerations, and *b* the third derivatives of r with respect to *t*, one has:

$$r(t + \Delta t) = r(t) + v(t)\Delta t + (1/2)\, a(t)\, \Delta t^2 + (1/6)\, b(t)\, \Delta t^3 + O(\Delta t^4)$$

$$r(t - \Delta t) = r(t) - v(t)\Delta t + (1/2)\, a(t)\, \Delta t^2 - (1/6)\, b(t)\, \Delta t^3 + O(\Delta t^4) \qquad (4.6)$$

Adding the two expressions gives

$$r(t + \Delta t) = 2r(t) - r(t - \Delta t) + a(t)\Delta t^2 + O(\Delta t^4) \qquad (4.7)$$

This is the basic form of the Verlet algorithm. Since we are integrating Newton's equations, *a(t)* is just the force divided by the mass, and the force is in turn a function of the positions *r(t)*:

$$a(t) = -(1/m)\nabla V(r(t)) \qquad (4.8)$$

As one can immediately see, the truncation error of the algorithm when evolving the system by Δt is of the order of Δt^4. This algorithm is largely popular among molecular dynamics simulators because it is simple to use, accurate and can give stable conditions.

The Verlet algorithm holds a problem with the above-mentioned benefits is that velocities cannot be directly generated. Though velocities are not needed for the time evolution, they are required to compute the kinetic energy K. To test the conservation of the total energy E = K+V, it is necessary to evaluate the kinetic energy. This is one of the most important tests to verify that a MD simulation is proceeding correctly. One could compute the velocities from the positions by using;

$$v(t) = \frac{r(t + \Delta t) - r(t - \Delta t)}{2\Delta t} \qquad (4.9)$$

However, the error associated to this expression is of order Δt^2 rather than Δt^4.

Some variations of the Verlet algorithm have already been developed to overcome this problem related to velocity. Exactly same trajectory can be obtained from these variations, and differ in what variables are stored in memory and at what times. One of the example is the leap-frog algorithm where velocities are handled better than ordinary Verlet algorithm [114].

A further improved implementation of the basic Verlet algorithm is the velocity Verlet scheme. This method incorporates positions, velocities and accelerations at time t+Δt which are obtained from the same quantities at time t in the following way:

$$r(t + \Delta t) = r(t) + v(t)\Delta t + (1/2)a(t)\Delta t^2$$

$$v(t + \Delta t/2) = v(t) + (1/2)a(t)\Delta t$$

$$a(t + \Delta t) = - (1/m)\nabla V(r(t + \Delta t))$$

$$v(t + \Delta t) = v(t + \Delta t/2) + (1/2)a(t + \Delta t)\Delta t \qquad (4.10)$$

4.1.6 Ensembles

An ensemble is a collection of all the possible states of a real system. There are several methods for controlling temperature and pressure. Depending on which state variables (the energy E, enthalpy H (that is, U+PV), number of particles N, pressure P, stress S, temperature T, and volume V) are kept fixed, different statistical ensembles can be generated as follows:

Constant Number of particles, constant temperature and constant pressure (NPT)

Constant Number of particles, constant temperature and constant volume (NVT)

Constant Number of particles, constant volume and constant energy (NVE)

Constant Number of particles, constant pressure and constant enthalpy (NPH)

4.1.6.1 NPT Ensemble

This ensemble enables control over both the temperature and pressure using constant number of particles, constant temperature, constant pressure (NPT). This process allows the unit cell vectors to change and the volume is adjusted by pressure adjustment. Berendsen, Andersen, or Parrinello-Rahman method can be used to control pressure. To control temperature Nose-Hoover, Andersen, or Berendsen method can be used. NPT ensemble can be chosen when priorities are given to correct pressure, volume and densities in the simulation.

4.1.6.2 NVT Ensemble

NVT ensemble is attained through constant number of particles, constant volume and constant temperature. Direct temperature scaling has been applied in this process during the initialization stage to control the temperature. Also, temperature-bath coupling has been applied during the data collection phase. Temperature controlled MD simulation is important in several types of systems.

4.1.6.3 NVE Ensemble

The pressure and temperature are not controlled during the simulation. The main objective is to conserve the energy. However, this might cause the pressure or temperature overshoot during time integration process. Typically, a system with higher stability is suitable for NVE. Thermodynamically systems following NVE ensemble are insulated from the surrounding environment.

4.1.6.4 NPH Ensemble

This ensemble is attained through constant number of particles, constant pressure and constant enthalpy H which is the sum of U and PV. In this process, the pressure is kept fixed without any temperature control. Although NPH dynamics do not control the temperature, it is possible to use these conditions during the equilibration phase of simulation. For this purpose, it is possible to hold the temperature within specified tolerances by periodic scaling of the velocities.

In our study, NVT ensemble has been adopted to perform temperature controlled simulation by keeping constant the number of particles and volume.

4.1.7 Particle-Particle Particle-Meshstyle (PPPM) & kspace_style command

The pppm style invokes a particle-particle particle-mesh solver [115] and this method maps atom charge to a 3d mesh. For this, Poisson's equation is solved using 3d FFTs on the mesh which then interpolates electric fields on the mesh points back to the atoms. This technique is close to the particle-mesh Ewald method (PME) [116] used in AMBER and CHARMM. Scaling of traditional Ewald summation can be described as $N^{(3/2)}$ where N is the number of atoms in the system. On the other hand, Nlog(N) scaling is used in PPPM solver due to the FFTs, which indicates that PPPM is always a faster choice [117]. The boundary condition for applying PPPM is that it must be 3d and periodic in all dimensions.The only exception where the above-mentioned boundary condition can be modified is slab option which has to be set with kspace_modify. In this case, the xy dimensions must be periodic and the z dimension must be non-periodic.

A long-range solver for LAMMPS to use each time step has to be defined to compute long-range Coulombic interactions or long-range $\frac{1}{r^6}$ interactions. The name of this command is "kspace_style command" as K-space is used by most of the long-range solvers perform their computation [118]. The cut-off for Coulombic or $\frac{1}{r^N}$ interactions is effectively infinite for

such a solver when used with an appropriate pair style. For the Coulombic case using this process simulation domain will be infinite. Because an infinite array of periodic images of the simulation domain will be created where each charge in the system interacts with charges in periodic image. Note that, to perform consistent short-range pairwise calculations using a long-range solver requires use of a matching pair style. This indicates that for each pair style there is a matching keyword for the Kspace_style i.e.for pppm solver pair style must be coul/long. In our study, lj/cut/coul/long pair style has been implemented with a global cut-off for LJ parameters.

4.1.8 General Procedure of Molecular Dynamics Simulation

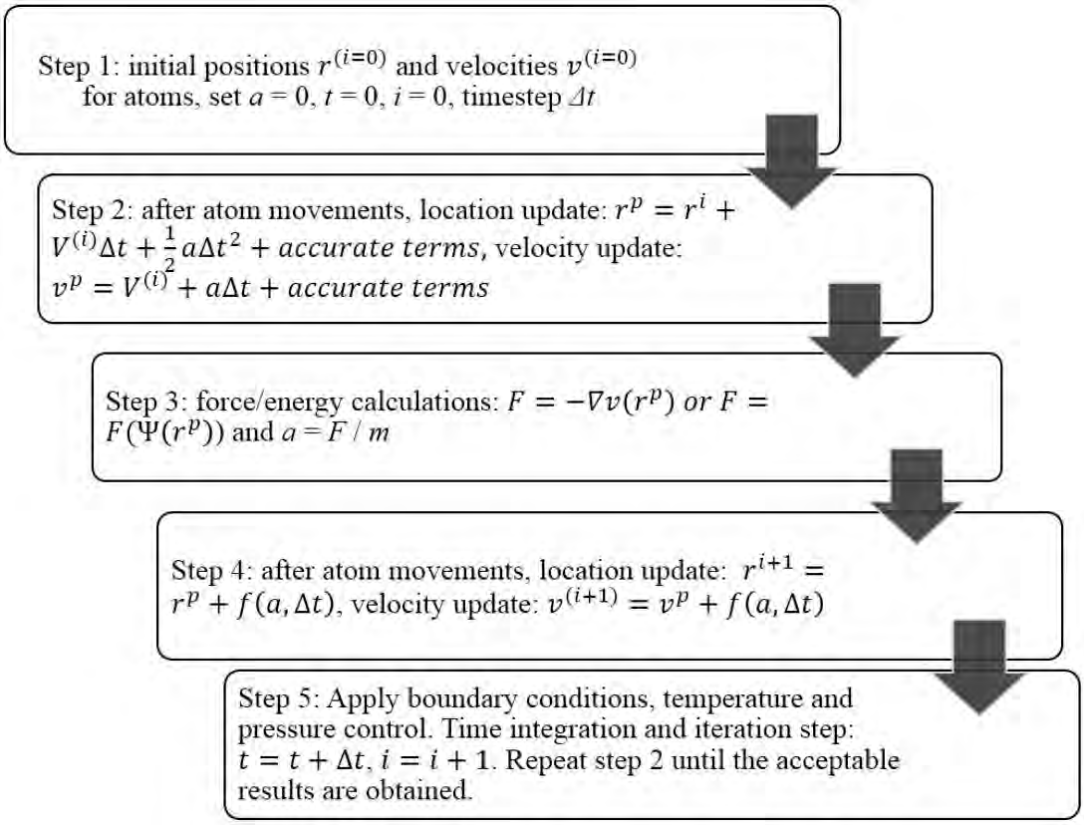

Fig 4. 2: Schematic diagram of a basic MD code. [119]

4.1.9 Limitations of MD Simulations:

Molecular dynamics is a very powerful technique but has limitations. We quickly examine the most important of them.

4.1.9.1 Use of Classical Forces

There can be some questions regarding the validity of molecular dynamics process as it uses Newton's law to move atoms. But it is well established that quantum laws are more relatable at the atomistic level rather than classical laws.

A simple test of the validity of the classical approximation is based on the de Broglie thermal wavelength [120], defined as:

$$\Lambda = \sqrt{\frac{2\pi\hbar^2}{M\kappa_B T}} \tag{4.11}$$

where M is the atomic mass and T the temperature. This approximation is justified for the condition $\Lambda \ll a$, where a is the mean nearest neighbor separation. If one considers for instance liquids at the triple point, Λ/a is of the order of 0.1 for light elements such as Li and Ar, decreasing further for heavier elements. For very light systems i.e. H_2, Ne the classical approximation is less effective.

4.1.9.2 Realism of forces

In molecular dynamics, due to atoms interaction among each other, instantaneous forces generate. These instantaneous forces act upon atoms and as a result, atoms move. The relative positions and forces change due to this movement.

In order to define the dominating parameter on the physics of simulation system, these instantaneous forces act as an essential ingredient. A simulation can be said as realistic if it mimics the behavior of the real system. This can only be judged by the interatomic forces if they are similar to the real values when arranged in the same configuration.

In molecular dynamics simulation, forces depend on the particles position and are usually obtained as the gradient of a potential energy function. Therefore, the realism of the simulation largely depends on appropriate potential. Potential must be chosen to reproduce the practical behavior of the material under the conditions of simulation's operation.

4.1.9.3 Time and Size Limitation

Typical MD simulations can be performed on systems containing thousands – or, perhaps, millions – of atoms, and for simulation times ranging from a few picoseconds to hundreds of nanoseconds. While these numbers are certainly respectable, it may happen to run into conditions where time and/or size limitations become important.

A simulation is safe from the point of view of its duration when the simulation time is much longer than the relaxation time of the quantities, we are interested in. However, different properties have different relaxation times. In particular, phase transitions make the systems slower and sluggish. As a result, there are possibilities of cases where simulation time is less than the relaxation time of a physical property.

Sizing of simulation domain is another crucial variable as limited system size can create problem. In this case, one has to compare the size of the MD cell with the correlation lengths of the spatial correlation functions of interest. Again, in the proximity of phase transitions correlation lengths may increase or even diverge. As a result, correlation lengths are no longer reliable to compare with the box dimension.

4.2 Modeling of the Simulation Domain for the present study

4.2.1 Graphene Models

Graphene shows significant electric conductivity along the basal plane which makes the charge/discharge process easier by promoting ion motion and electron propagation. By modifying the surface morphography, adding defects, designing pore structure power density, energy density and lifetime of EDLCs can significantly be enhanced. Molecular dynamics simulation of super capacitor electrode has two proposed models, which are a planer model and a slit-type model.

4.2.1.1 'Planer' Model

Planer simulation domain consists of two oppositely charged parallel plates which are separated by several nanometers distance. From Fig. no. 4.3, the light-yellow atoms indicate graphene sheet, blue and pink atoms combination over graphene sheet indicates the nanostructured MnO_2, the deep yellow atoms indicate the NaCl electrolyte and red-blue-white atoms indicate the water molecules.

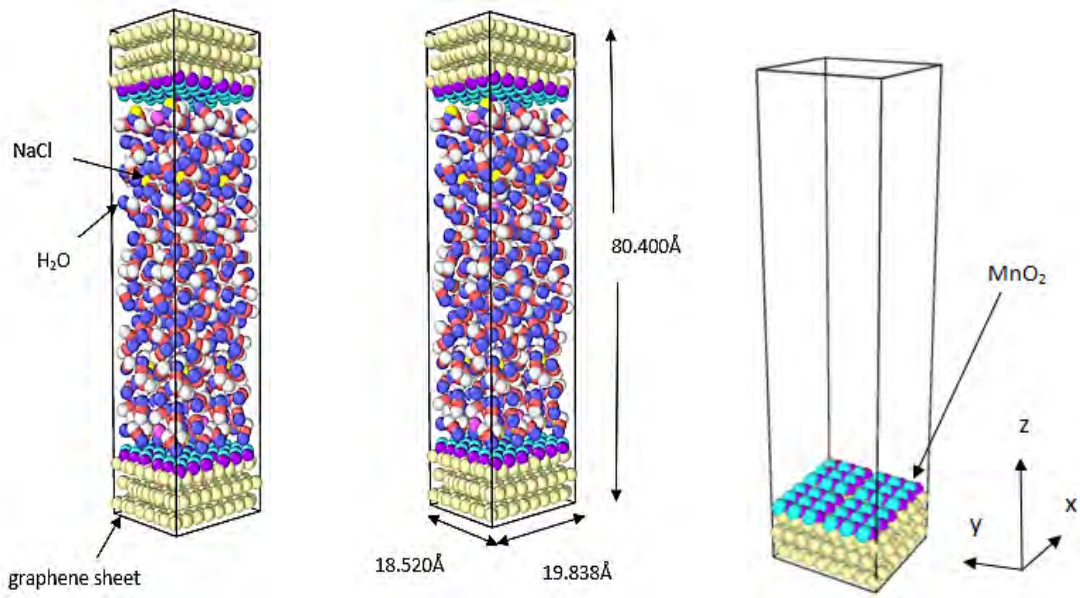

Fig 4. 3: Simulation domain of Planer model.

4.2.1.2 'Nano-pore' Simulation Model

Nano slit-pore simulation domain consists of also with two oppositely charged parallel plates but there will be pore in the parallel electrodes. The electrodes of each side can be made of two or more parallel plates with same sign of charge. From Table 4.1 and Fig. no. 4.4 three variations in Nano slitpore width have been implemented in this study

Table 4. 1: Nano-pore variations in graphene-MnO_2 electrodes

Pore width variation, δ (Å)
3.55
7.1
9.23

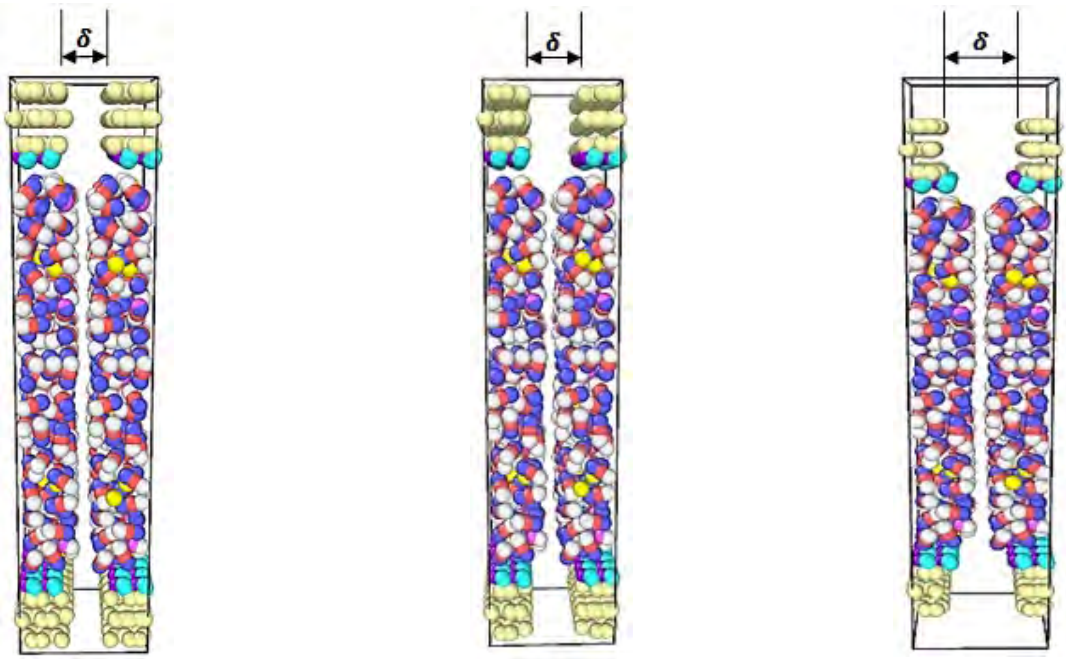

3.5 Å 7.1 Å 9.23 Å

Fig 4. 4: Simulation domain of Nano slitpore model.

4.3 Simulation Physics employed in the present study

- Columbic interaction in the simulation domain has been calculated using the Particle-particle particle-mesh (PPPM) algorithm of LAMMPS.

- Water interaction is determined by using the TIP3P (transferable intermolecular potential 3P) model and shake algorithm. This algorithm can reproduce the experimental dielectric constant of water better than any other model.
- Lenard-Jones (LJ) potential parameters are used to produce the van- der-Waals interactions among the ions, carbon atoms and water molecules.
- Molecular Dynamics simulation is used to find the number density ρ(x) of particles which is widely used to represent the electric double layer structure. As for electrolytes, higher number density ρ(x) indicates concentrated electrolytes, which are required to reduce the equivalent series resistance and maximize power output.
- Constant surface charge and constant electric potential method can be used on electrodes. Both methods show negligible difference in EDL structure for low electric potential (<2V). Also, constant electric potential method is more preferable for experimental conditions. In this study, constant surface charge method is adopted to apply on electrodes.

4.4 Simulation Time step

Simulation domain temperature has been controlled by Berendsen thermostat. Temperature was increased from 298K to 373K using a period of 10ps, kept at 373K for another 10ps and then gradually cooled to 298K over a period of 10ps. Using NVT ensemble MD simulations are carried for another 1.2ns at 298K. The full simulation timestep in LAMMPS code:

```
fix 1 sol nvt temp 298.0 373.0 100.0
run 10000
unfix 1
fix 1 sol nvt temp 373.0 373.0 100.0
run 10000
unfix 1
fix 1 sol nvt temp 373.0 298.0 100.0
run 10000
unfix 1
fix 1 sol nvt temp 298.0 298.0 100.0
run 1200000
```

Here, the actual code is: fix fix-ID group-ID nvt temp T_{start} T_{stop} T_{damp}

Where, T_{start}, T_{stop} = external temperature at start/end of run

T_{damp} = temperature damping parameter (time units)

Nose-Hoover style non-Hamiltonian equations of motion are used for time integration in these commands. Through this integration process positions and velocities are generated forcanonical (nvt), isothermal-isobaric (npt), and isenthalpic (nph) ensembles.

4.5 Simulation Domain

4.5.1 Simulation Cell

The distance between the inner most electrode layers of simulation cell is 6.105 nm. Table 4.2 presents the summary of simulation cell formation where the electrolyte solution consists of 16 NaCl and 320 water molecules for 1.00 M solution concentration. The total dimensions of the simulation domain are 1.9838, 1.8520 and 8.04 nm.

Table 4. 2: Number and types of atoms, bonds, angles in the simulation cell

Total atoms	**2056**
Total bonds	656
Total Angles	320
Atom types	8
Bond types	3
Angle types	1
Size of simulation cell (nm)	1.9838 * 1.8520 * 8.04

4.5.2 Electrolyte solution

Water molecules have accordingly filled in the simulation cell to generate a pressure close to 1 bar. The determining factors for electrolyte ions numbers are the concentration and charge neutrality of the whole system.The numbers of water molecules and solvent ions (NaCl) used in our Molecular Dynamics simulation system has been summarized in Table 4.3.

Table 4. 3: Ionic strength of solution used in EDLC simulation

Number of molecules		**Ionic strength / molar concentration (for mono charged ions both are same) (M)**
Water	Na^+ and Cl^-	
320	16	1.08 ≈ 1.0
320	18	1.21
320	26	1.75
320	29	1.96 ≈ 2.0

4.6 Simulation Parameters employed

4.6.1 Atoms

Seven types of atoms have been chosen from the periodic table for the Gaphene-MnO_2 based supercapacitor system developed in our study. Table 4. 4 represents the atoms with their atomic radius used in the simulation process.

Table 4. 4: Number of atoms and their size used in the simulation

Atom Type	**Atom**	**Radius (nm)**
1	C	0.077
2	Mn	0.126
3	O	0.066
4	H	0.037
5	O	0.066
6	Na	0.186
7	Cl	0.099

4.6.2 Force Field parameters – bond coefficients

LAMMPS uses to compute bond interactions between pairs of atoms. Bonds are defined between specified pairs of atoms by bond coefficients and remain in force for the duration of the simulation. In our study, harmonic bond style has been used where r_0 is the equilibrium

bond distance and k is the bond energy/distance^2. Atomic masses of all atoms have to be specified along with the bond coefficients for LAMMPS input file. All parameters have been summarized in Table 4.5 and 4.6.

Table 4. 5: bond coefficients of atoms in electrolyte and solvent molecules

Bond Coefficients		
Atom	**K (kcal Å^{-1})**	**r_0 (Å)**
Na - Cl	799.280	1.40
water O-H	554.135	1.0

Table 4. 6: Atomic mass of the atoms used in simulation

Element	Mass (AMU)
O	15.999000
H	1.0079000
C	12.010700
Na	22.989769
Cl	35.453002
Mn	54.938044

4.6.3 Lennard-Jones parameters

The van der Waals interactions among the electrolyte ions, carbon atoms, MnO_2 molecules and the water molecules have been described by using the modified Lenard-Jones (LJ) potential. As Transferable intermolecular potential 3P (TIP/3P) model can best reproduce the experimental dielectric constant of water among the popular water models, it has been employed for water. The SHAKE algorithm has been employed to keep the bond lengths and angles in water molecules fixed. The Lorentz-Berthelot mixing rule has been adopted to determine the LJ potential parameters between electrolyte ions, waters, MnO_2 molecules and carbon atoms. Table 4.7 presents the pair coefficients of all atoms used in this study.

Combining rules for the Lennard-Jones potential: Lorentz-Berthelot rule

The Lorentz rule was proposed by H. A. Lorentz in 1881: $\sigma_{ij}=\frac{\sigma_{ii}+\sigma_{jj}}{2}$

The Lorentz rule is only analytically correct for hard sphere systems.

The Berthelot rule (Daniel Berthelot, 1898) is given by: $\varepsilon_{ij}=\sqrt{\varepsilon_{ii}\,\varepsilon_{jj}}$

Table 4. 7: Pair coefficients and valence of atoms used in simulation [118]

Pair Coefficients			
Atom	**ε (depth of potential wall) kcal mol^{-1}**	**σ (finite distance at which the inter-particle potential is zero) Å**	**Valence (e)**
O (TIP3P)	0.15540000	3.16550000	- 0.834
H(TIP3P)	0.00000000	0.00000000	0.417
C (graphene)	0.12000000	3.29630000	0 - 0.0637
Na	0.13010000	2.35020000	+1
Cl	0.10000000	4.40000000	-1
Mn	0.03180000	2.09880000	+4
O	0.15540000	3.16550000	-2

4.6.4 Surface Charge density

As commonly done in molecular dynamics simulations, the applied voltage is presented as a uniform distribution of electrical charges on the carbon atoms. Applying positive and negative charges on opposite electrodes, Fig. no. 4.3 and 4.4 represent formation of a capacitor. From Table 4.8, different surface charge densities such as 40, 30, and 20 μC/cm^2 can be obtained by varying the electronic charges on the carbon atoms which are used in this study. These surface charges are chosen by keeping consistency with previous studies. The estimated maximum charge per carbon atom is 0.0685 e/C-atom using theoretical graphene capacitance of 21 μF/cm^2 and potential difference of 1V for aqueous electrolytes [121].

Table 4. 8: Numeric values of charge imposed on carbon atoms in graphene-MnO_2 electrode

Maximum charge per carbon atom to be 0.0685 e/C atom (estimated)	
Neutral graphene surface	0 e/C
40 μC / cm^2	.0637 e/C
30 μC / cm^2	0.0477 e/C
20 μC / cm^2	0.03185 e/C

In the MD simulation proposed here, two key features have been taken into account: (1) a realistic atomistic structure for a microporous carbon electrode (2) the polarization of the electrode atoms by the ionic charges. The second approach can perform simulations using constant applied electrical charge under (conducting) electrodes of arbitrary geometry.

In order to perform a fair comparison, the constant charges were assigned based on the average total charge measured during constant potential simulations for various applied potential differences. This total charge was equally distributed among the carbon atoms, and the self-consistency of the procedure was checked by calculating the potential difference arising from the so-built constant charge simulations. It is worth mentioning that the variation of the charge with respect to the potential drop at the electrode/electrolyte interface obtained with the constant charge simulations agrees very well with that obtained with the constant potential simulation ones, resulting in similar values for the differential capacitance. The performance of supercapacitors in terms of power (i.e. how fast the charge can be delivered) can be assessed by modelling the polarization relaxation during transient regimes. This is done by performing simulations where the applied potential difference or the charge is suddenly changed and by characterizing the processes which occur before the new steady-state is reached. The difference between constant potential and constant charge simulations is then much more spectacular.

These authors concluded that constant potential simulations provided much more reasonable double layer relaxation times. In the case of constant applied potential simulations, the charge on the electrode atoms varies in response to the ionic liquid; as a consequence, the charging of the initially empty pores occurs gradually while they become wetted, resulting in much slower relaxation times [122]. However, constant potential method is highly computational

demanding than the popular constant surface charge method. In addition to this, according to several studies EDL structures showed a negligible difference in simulation between these methods specially at electric potential lower than 2 V. Therefore, in this study, we adopted the conventional constant surface charge method [121].

4.7 Electric Potential Calculation

In this study, the channels have been divided into a set of bins (of 5 Å in width) along the direction (x) perpendicular to the graphene surface. The averaged number density of particles (e.g., water, electrolyte ions) has been calculated in each bin. Theses averaged number densities have been represented the number densities ρ(x) of the corresponding particles. To represent the EDL structures in simulation models, number density ρ(x) is widely used in. The resultant electric potential V (x) can be computed by integrating the following one-dimensional Poisson equation [118]

$$\frac{\delta^2 V(x)}{\delta x^2} = -\frac{q(x)}{A_G \varepsilon_0} \tag{4.12}$$

Where x is the distance to the graphene surface (x > 0), q(x) is the total charge quantity at x, A_G is the cross-section area of MD simulation, namely the size of graphene sheet, and ε_0 is the vacuum dielectric constant. Note that, the total charge quantity term includes the electrode charge, electrolyte ion charge and also the charges of hydrogen and oxygen atoms of water molecules. The V(x) value in the middle of the channel (x = ± L/2) was used as a reference. Since the channel is symmetrical, the dv/dx value at x = L/2 should be equal to zero. The integral of the above eqn. 4.12 yields the potential V(x):

$$V(x) = -\iint_{\frac{L}{2}}^{x} \frac{q(x)}{A_G \varepsilon_0} dx^2 \tag{4.13}$$

To find the electric potential from eqn. 4.13,

$$V(x) = -\iint_{\frac{L}{2}}^{x} \frac{q(x)}{A_G \varepsilon_0} dx^2$$

Where, $A_G = 367.39976 * (10^{-10})^2\ m^2$

$\varepsilon_0 = 8.854*10^{-12}$ F/m (vacuum permittivity)

Bin size, h = 5 Å

Numerical integration using Simpson's 1/3rd rule at x = -27.7 Å,

$$V(x) = -\frac{q(x-2h)+8q(x-h)+18q(x)+8q(x+h)+q(x+2h)}{A*\varepsilon} * \frac{(h*h)}{9} \tag{4.14}$$

Charge, q = 288 + 432*A + B*(0 or 1) + (0.834*(C/2)) + (2*0.417*(C/2))

A = 0/0.0637 /0.47 etc.

B = number of atoms from density-NaCl

C = number of atoms from density-water

Form x = -27.7 Å to x = -2.7Å

Simpson's 1/3rd rule has been used to numerically calculate the induced or resultant electric potential in the system. From eqn. 4.14 it can be observed that, the resultant potential depends on charge counts of graphene surface, electrolytes and water. Also, dielectric constant of electrolyte and solvent is a key factor to manipulate the resultant potential.

CHAPTER 5

Results and Discussion

The energy storage behavior of graphene-MnO_2 electrode in aqueous electrolyte has been investigated both experimentally and numerically. The computational model used in the molecular dynamics (MD) has been validated using simulation tool like radial distribution function (RDF). The validated computational model has been used to investigate the atomic behavior of electric double layer supercapacitor (EDLC) and an optimized, improved model has been proposed from this study. The results and findings have been discussed in this chapter.

5.1 Experimental Analysis

5.1.1 Scanning Electron Microscope (SEM) Analysis

The FESEM image of graphene-MnO_2 nanocomposite is shown in Fig. no. 5.1. From the surface morphology of the prepared graphene-MnO_2 composite, it is seen that there is no aggregation of particles as in the case of MnO_2 and the MnO_2 nano fibers are uniformly and densely distributed covering almost whole of the graphene sheet.

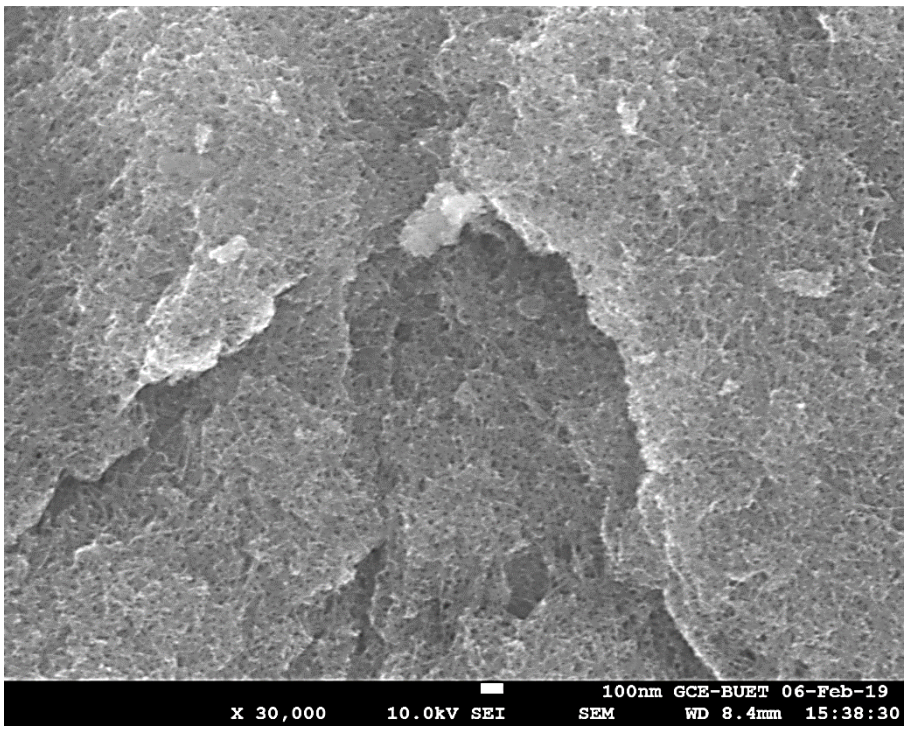

(a)

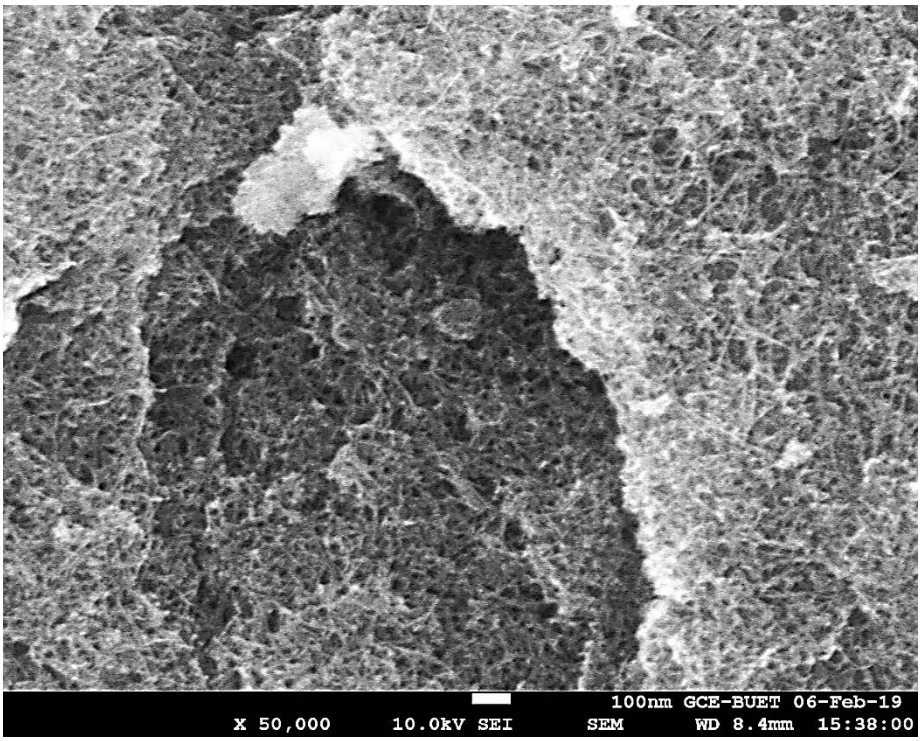

(b)

Fig 5. 1 : SEM image of expected rGO-MnO_2 nanocomposite (a) 30,000 magnification and (b) 50,000 magnification.

Moreover, the MnO_2 nano-fibres homogeneously locate on graphene sheets and act as spacers to effectively prevent the agglomeration of graphene sheets, keeping their high active surface. It can be seen here that the small and thick fibre like structure of MnO_2 are more visible than before probably due to the no aggregation of the nanoparticle which in turn may be due to the interatomic or intermolecular interaction between MnO_2 particle and graphene. The surface of graphene-MnO_2 nanocomposite is porous in nature which is responsible for the increased functionality of the graphene-MnO_2 nanocomposite.

5.1.2 Energy Dispersive X-Ray Spectroscopy (EDX) Analysis

The elemental composition of the prepared sample was analyzed using Energy Dispersive X-ray (EDX) analysis. The EDX spectrum of graphene-MnO_2 is shown in Fig. no. 5.2. The lines observed at 0.55, 5.8 and 6.5 keV are associated with L and K (α, β) lines of the Mn element, respectively. The EDX line at 0.25 and 0.50 keV represents K line of the C and O element. The quantification results of the EDX data provided the percentage of each element with energy distribution present in the matrix which allowed us to obtain directly the composition of the samples.

The EDX result of the graphene-MnO_2 binary composite confirms the presence of graphene C, in addition to significant amount of Mn and O of MnO_2 in the sample suggesting a MnO_2 nanoparticle loaded graphene surface. The EDX analysis shows the presence of manganese and oxygen in the prepared sample and their atomic composition were found to be 16.20 and 32.02 %, respectively, indicating the ratio of Mn:O as 1:2 which attributed that the synthesized manganese oxide was MnO_2.

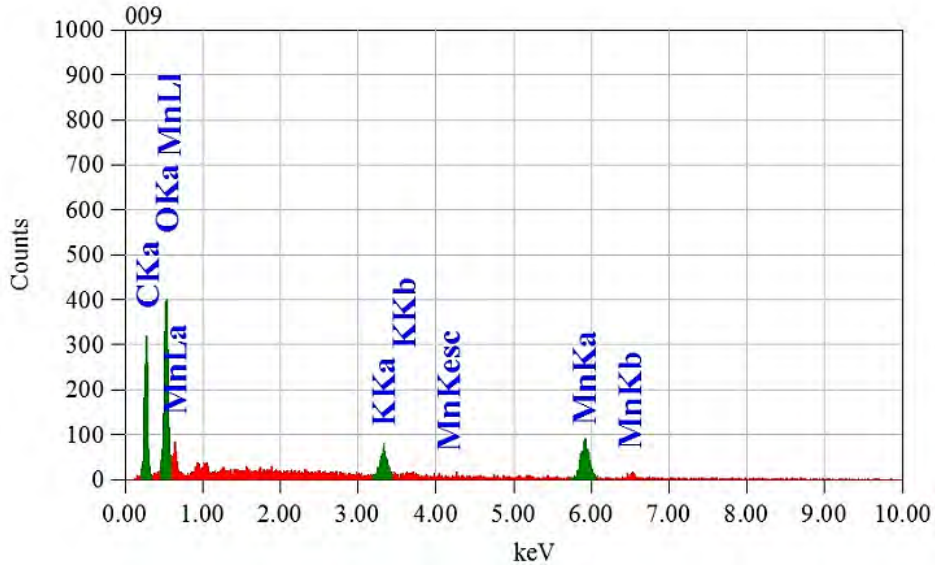

ZAF Method Standardless Quantitative Analysis
Fitting Coefficient : 0.1331

Element	(keV)	Mass%	Sigma	Atom%	Compound	Mass%	Cation	K
C K	0.277	27.81	0.32	48.76				18.3680
O K	0.525	24.33	0.45	32.02				26.6328
K K	3.312	5.60	0.29	3.01				7.2488
Mn K	5.894	42.26	1.70	16.20				47.7504
Total		100.00		100.00				

Fig 5. 2: EDX spectra of rGO-MnO_2 nanocomposite.

5.1.3 X-Ray Diffraction (XRD) Analysis

The XRD analysis of the prepared graphene-manganese oxide composite (Fig. no. 5.3) shows poor crystalline nature of MnO_2 on the surface of graphene.

The slight shifting of the diffraction angles (2θ = 24.8, 36.6, 44.8, 65.5) as well as peak intensity in the XRD patterns of graphene-MnO_2 composite may be attributed to the effect of graphene and is the evidence that MnO_2 nanoparticle have been incorporated successfully on graphene sheet. The peak positions can be identified easily following the Bragg's law: $2d \sin\theta = n\lambda$. From the relation, it can be seen that if there is a change in the inter-layer distance (d) value which means that change in the lattice parameter, theta (θ) value will be changed

reciprocally assuming the experimental condition is same for all the samples. The intensity of XRD peak of graphene is too low compared to MnO_2 to be seen in the pattern. The XRD pattern of graphene-manganese oxide composite shows two very weak broad diffused peak at 2θ = 13.14° and 2θ = 36.6° with a decreased 2θ angle, probably due to formation of composite. Moreover, the absence of any sharp peak related to graphene in the composite indicates that the surface was fully covered with high amount of manganese oxide with poor crystalinity [123].

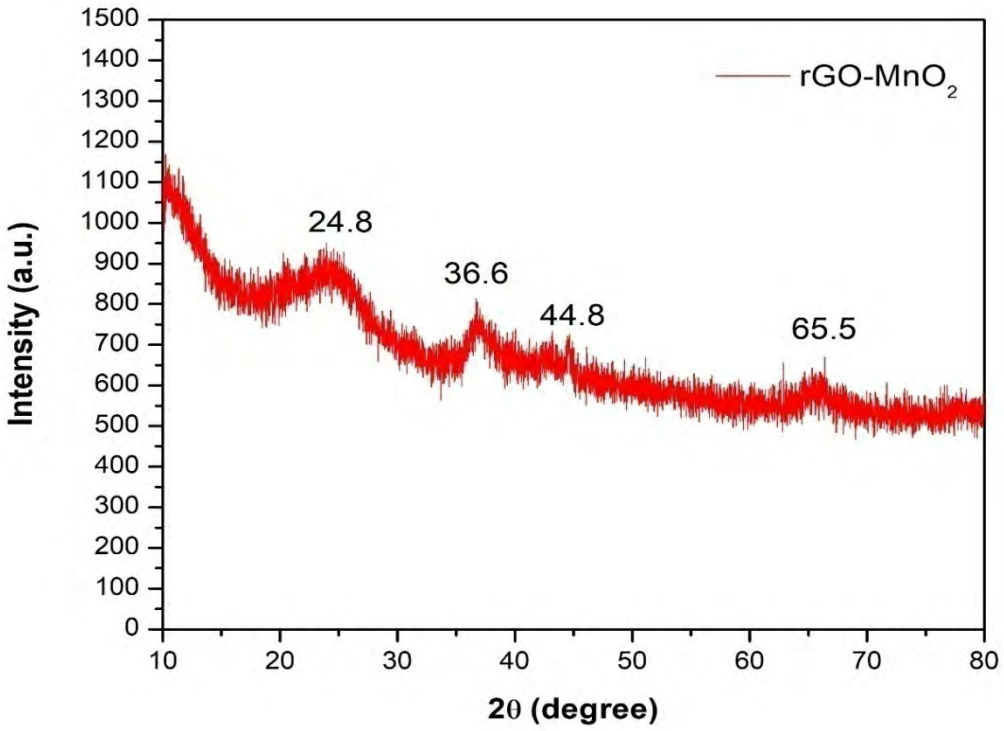

Fig 5. 3: XRD pattern of rGO-MnO_2 nanocomposite with broad diffused peak at 2θ = 13.14° and 2θ = 36.88°, indicating absence of crystalline peak as a result of amorphous GO-MnO_2.

5.1.4 Electrochemical Analysis

The electrochemical characterization of the nanocomposites was carried out in a computer controlled electrochemical working station (HANKO HAB 151 Galvanostate and Potentiotate). Two electrochemical techniques namely cyclic voltammetry (CV) and chronopotentiometry (CP) had been employed in this endeavor. The focuses of these experiments were to find out the capacitive behavior of the graphene-MnO_2 nanocomposite in NaCl electrolyte.

5.1.4.1 Cyclic Voltammetry (CV)

The CV of the samples was performed to find the potential window within which they show capacitive behavior and its dependency on scan rate. Initially, in each case, CV was taken within -100 mV to 800 mV which was later adjusted to the symmetric shape of cyclic voltammogram that corresponds to capacitive behaviour. Then, CV was performed at different scan rate, starting from 2 mV/s to up to 100 mV/s.

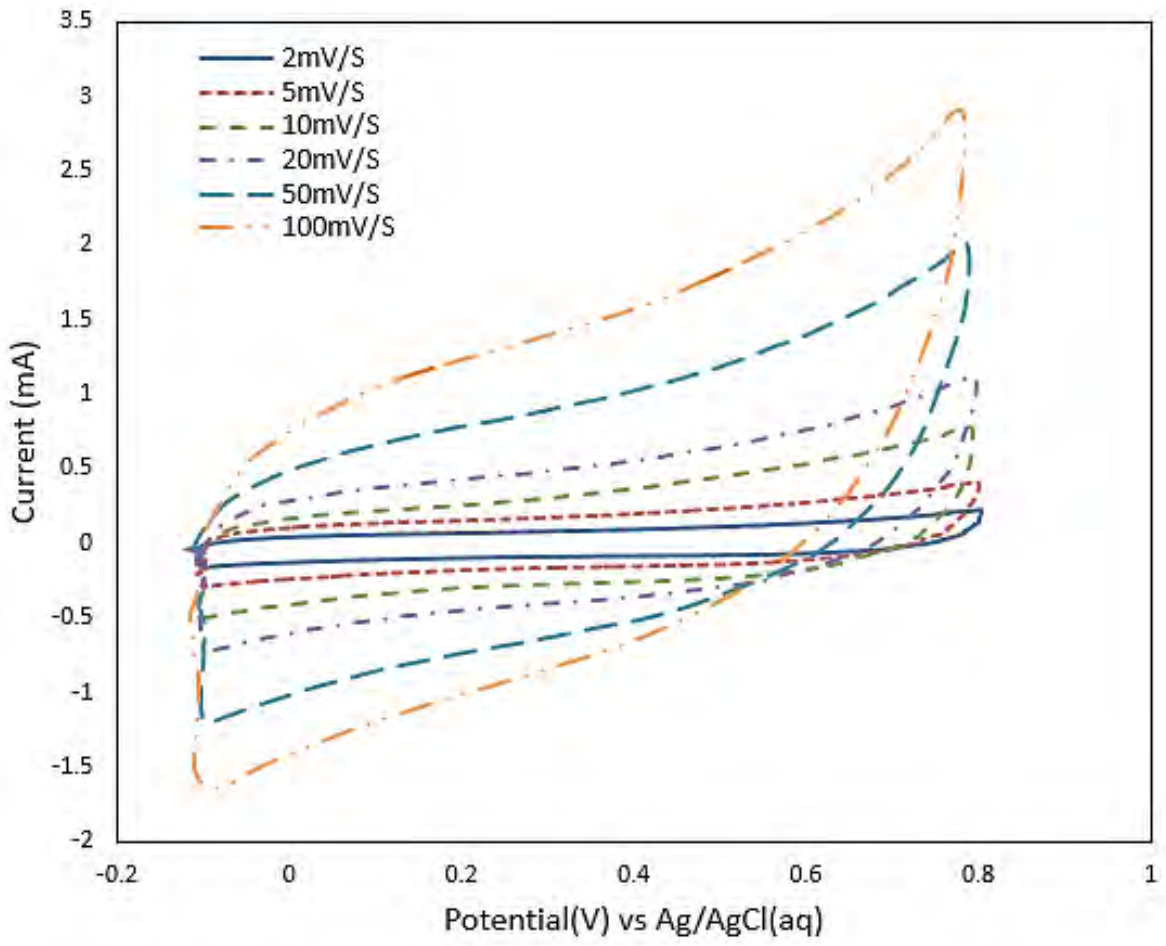

Fig 5. 4: Cyclic Voltammetry curve for various scan rates for rGO-MnO_2 composite at Potential Window: -100-800mV and active mass 0.000405g.

Table 5. 1: Specific capacitance for various scan rates for rGO-MnO_2 composite at Potential Window: -100-800mV and active mass 0.000405g

Active Mass(mg)	Potential Window(mV)	Scan Rate(mV/s)	Specific Capacitance(F/g)
0.405	-100-800	2	110
		5	86
		10	74
		20	53
		50	35
		100	25

The CV curve of graphene - MnO_2 nanocomposite at different scan rates is shown in Fig. no. 5.4. The specific capacitance value of 110, 86, 74, 53, 35 and 25 Fg^{-1} are found for graphene-MnO_2 composite within the potential range from -100 to 800mVat the scan rates of 2, 5, 10, 20, 50 and 100 m Vs^{-1} respectively. The highest specific capacitance value of 110 Fg^{-1} is found for graphene-MnO_2 composite within -100 to 800mV at 2 mVs^{-1} scan rate (Fig. no. 5.4).

As revealed from all figures of the CV curves of the graphene - MnO_2 at different scan rates, the shapes of the CV curves were significantly influenced by the scan rate. At a low scan rate, the CV curves shows an ear-ideal rectangular shape, which indicates that charging and discharging took place at a constant rate over the applied voltage range [124]. From Table 5.1, it can be seen that the specific capacitance gradually decreases as the potential scan rate is increased. This may be because at high scan rates, diffusion limits the movement of electrolyte (Na^+ ions) by the time constant, and only the outer active surface is utilized for the charge storage. However, at lower scan rates, all the active surface area can be utilized for charge storage [125].

5.1.4.2 Chronopotentiometry (CP)

Chronopotentiometric technique also known as Galvanostatic Charging Discharging (GCD), was used to evaluate the specific capacitance of the samples with different charging-

discharging c urrent o r c urrent d ensity varying from 0.07 $mAcm^{-2}$ to 72 $mAcm^{-2}$ within suitable potential window chosen from CV.

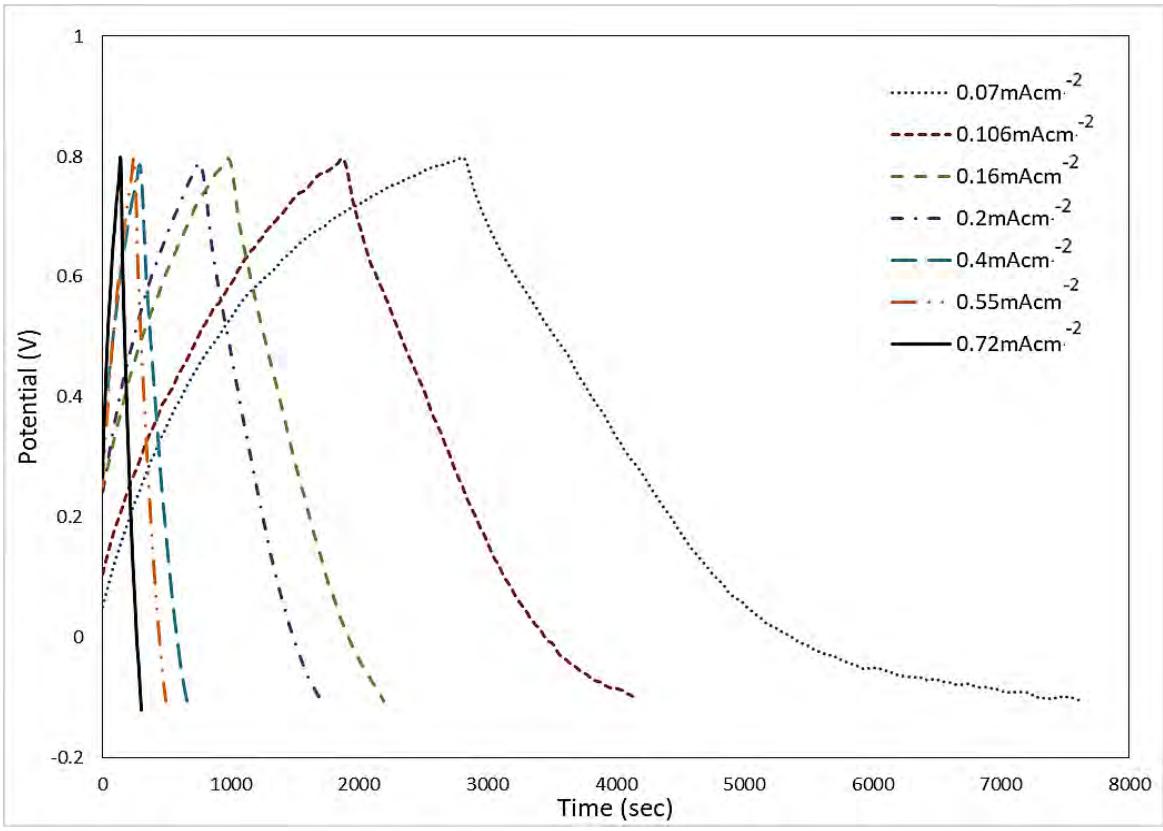

Fig 5. 5: Charge-discharge curve for various current density for rGO-MnO_2 composite at potential window -100-800 mV and active mass 0.000405g.

Table 5. 2: Specific capacitance from Galvanostatic Charging Discharging and Cyclic Voltammetry for rGO-MnO_2 composite at potential window -100-800mV and active mass 0.000405g

Active Mass(mg)	Potential Window(mV)	Current Density ($mAcm^{-2}$)	Specific Capacitance(F/g) from CV	Specific Capacitance(F/g) from GCD
0.405	-100-800	.07354	110	261
		0.106103	86	187
		0.166228	74	154
		0.201596	53	145
		0.406728	35	110
		0.555273	25	103

The GCD curve of MnO_2-graphene composite at different magnitude of current densities is shown in Fig. no. 5.5. From the curve, the values of specific capacitance for MnO_2-graphene nanocomposite are found as 261, 187, 154, 145, 110 and 103 Fg^{-1} at current densities of 0.07, 0.106, 0.16, 0.2, 0.4, 0.55 $mAcm^{-2}$, respectively. The highest specific capacitance value for MnO_2-graphene has been found from the GCD curve at 0.07 $mAcm^{-2}$ current density as shown in Fig. no. 5.5 which is equal to 261 Fg^{-1}.

In the chronopotentiometric study at different currents, it is observed from Table 5.2 that the discharge capacitance was monotonically decreased with an increase in current density. This may be due to the low penetration of the ions into the inner region of pores due to fast potential changes. In other words, the decrease in capacitance value at higher current density is attributed to the restriction arise from faster movement of electrolyte ions towards adsorption sites [126].The supercapacitors exhibited appreciably-high specific capacitance even at a high current density. The lower values of capacitance at high current rates might be due to less ionic penetration in the electrode surface compared to the case at a low current rate. As expected, the capacitance of the cell decreases linearly with increasing current densities, which is the typical behavior of electrochemical supercapacitors [127-128].

Several research works have been going on the graphene-MnO_2 nanocomposite to understand its capability as energy storage material. Depending on the preparation method, graphene-MnO_2 nanocomposite's energy storage behavior (specific capacitance) varies dramatically. In our study, 'Modified Hummers method' has been used for preparing graphene oxide and reduced graphene oxide - manganese dioxide was synthesized by in situ chemical reduction of $KMnO_4$. Table 5.3 gives an idea by comparing specific capacitance of graphene-MnO_2 nanocomposite prepared by different methods in different research projects. Comparing these research projects it can be stated that graphene-MnO_2 supercapacitors have high potential in energy storage sector.

Table 5. 3: Comparison of specific capacitance of different graphene-MnO_2 supercapacitors

Researches on graphene-MnO_2 supercapacitors	**Specific Capacitance (F/g)**
From Present Study	261
Study of MnO_2-Graphene Oxide nanocomposites for supercapacitor applications by Singhal, R. *et al.*(2019)	350
Construction of hierarchical holey graphene/MnO_2 composites as potential electrode materials for supercapacitors by Chai, Y. *et al.* (2019)	192.2
Compounding δ-MnO_2 with modified graphene nanosheets for highly stable asymmetric supercapacitors by Wang, X. *et al.* (2019)	270
Three-Dimensional Graphene/MnO_2 Nanowalls Hybrid for High-Efficiency Electrochemical Supercapacitors by Xiong. C. *et al.* (2018)	266.75

5.2 Molecular Dynamics Analysis

5.2.1 Validation

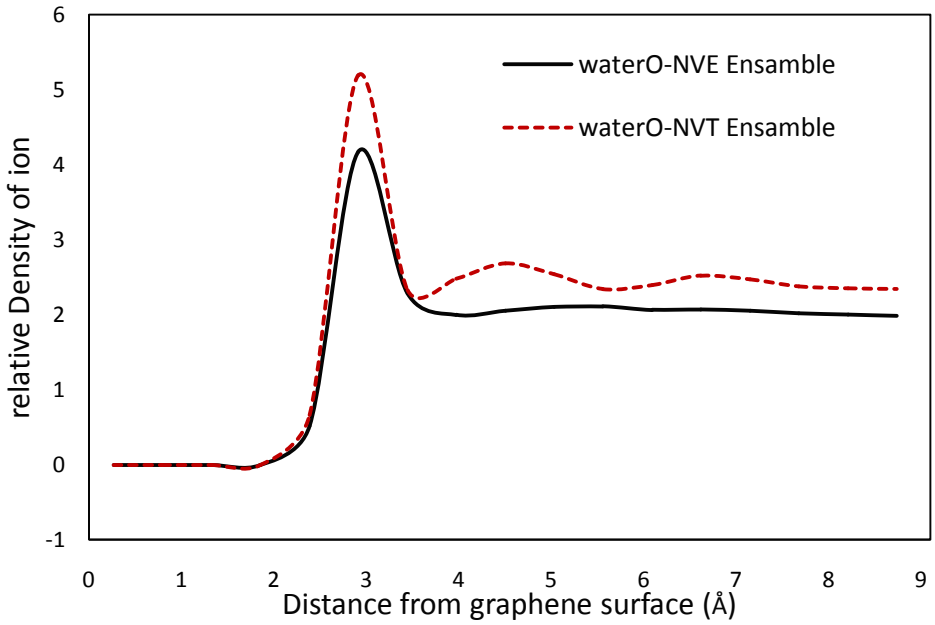

(a)

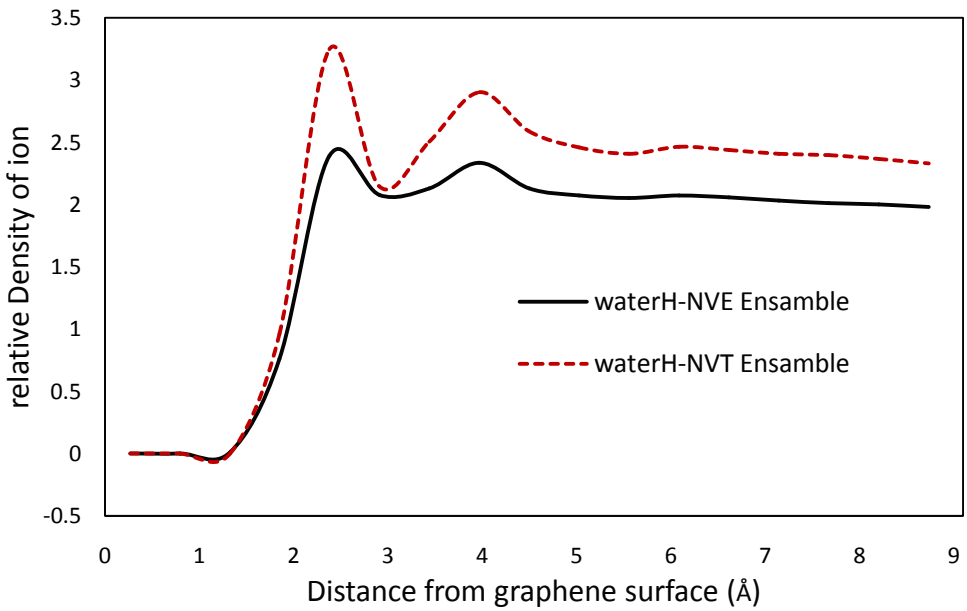

(b)

Fig 5. 6: Radial Distribution functions of 1M concentration planer model of neutral graphene electrode (a) for water-oxygen atom, and (b) at water-hydrogen atom.

In order to verify the simulation design of present study, we tried to compare our findings with well established and published studies. There are several molecular dynamics researches

to study the water models (structure and dynamics). If our present simulation domain is properly designed, solvent (water) will give density peak at same position of previous studies. All different water models, the TIP3P (original, modified), SPC (original, refined), and SPC/E (original) were compared using identical microcanonical (NVE) or NVT simulations. In our study, NVT ensemble has been adopted for temperature controlled simulation of electric double layer supercapacitor.

Radial distribution functions (RDF) can identify the density peaks from electrode surface in simulation domain. From Fig. no. 5.6, simulations performed at NVE ensemble for MnO_2-graphene electrode with aqueous NaCl are closer to experimental and computational results [126]. According to previous studies, without electrode surface charge, the RDF density peak of oxygen of water molecule is about 3 and the distance from the electrode surface is about 3.2 Å. In our case, the RDF density peak of oxygen is about 4 and the distance from the electrode surface is about 3.2 Å for NVE ensemble, which is in good agreement with previous MD results [129]. In the present study, all simulations are conducted using the package LAMMPS in the NVT ensemble keeping consistency with previous simulation studies [130].

From the above sections, it is clear that our proposed simulation design showing similar RDF distance and peaks comparing with previous studies. It can be said that due to composite of graphene and MnO_2, water oxygen and hydrogen ions are more attracted to the electrode surface and density peaks increases slightly than previous results.

5.2.2 'Planer' Model

The planer model of Molecular Dynamics (MD) simulation consists of graphene-MnO_2 electrodes where MnO_2 is nanostructured in the graphene sheet. Without MnO_2, graphene sheet alone can show significant electric double layer (EDL) properties. That is why the impact of graphene electrode in EDL before and after adding MnO_2 is the first step of this study. Addition of MnO_2 on graphene electrodes increases the surface contact area for electrolytes which is visible in our simulation domain. According to previous studies, the surface area increases up to 1.5 times for graphene-activated carbon surfaces than only graphene surfaces [131]. It can be concluded that a large number of micropores and a low fraction of interconnected mesopores featured by narrow orifice, large inner cavity and limited fraction of macropores have coexisted in the MnO_2-graphene composites. The versatile porous texture of MnO_2-graphene is extremely advantageous for its application as

supercapacitor electrode materials [131], as high surface area resulted from micropores is highly beneficial for the accumulation of electrolyte ions.

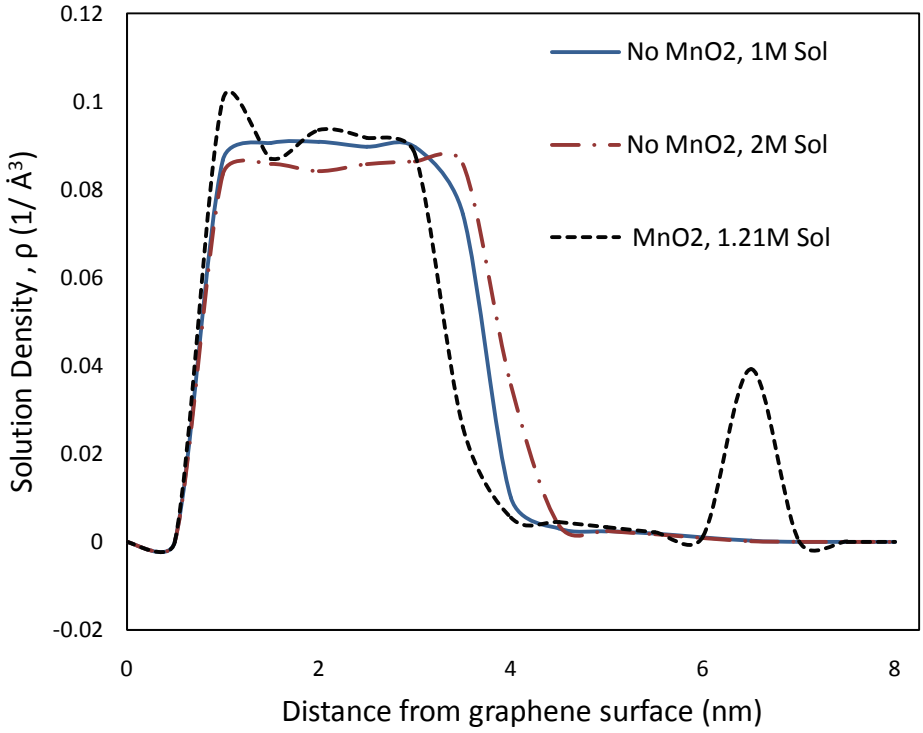

Fig 5. 7: Density profiles of Planer model with neutral graphene-MnO_2, and graphene electrode at different solution concentrations.

Density profiles indicate the number density of electrolyte ions and solvent with distance from the electrode surface. As for EDLC, the number density of ions near the electrode is the prime concern that is why density profiles have been studied in this research. From Fig. no. 5.7, the solution ions (waterO, waterH, Na^+, Cl^-) are more attracted to electrode when consists of MnO_2 and graphene rather than only graphene. As a result, the first density peak of solution for graphene electrode is less than that of MnO_2-graphene electrode. Also, solution ions shift more towards bulk region in case of graphene electrode than graphene-MnO_2 electrode. All the results indicate that adding MnO_2 in graphene electrode shows positive impact to attract electrolyte and solvent ions.

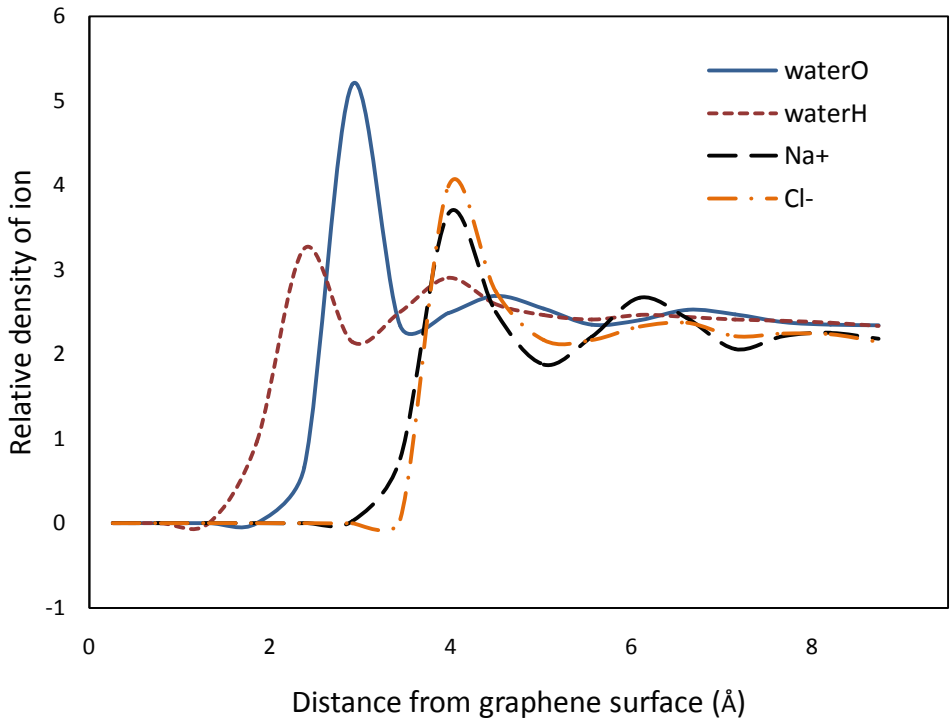

Fig 5. 8: Radial Distribution functions (RDF) for Planer model with neutral graphene electrode at 1M solution concentration.

The radial distribution function (RDF, also known as pair correlation function), g(r) is a very useful tool in molecular dynamics simulation. This quantity represents the average distribution of atoms around any given atom within the system. The g(r) can also be present as a quantity that multiplies the bulk density ρ to get the local density ρ(r). This implies that the radial distribution function gives the density distribution of a system if one looks radially outwards from an atom. Thus at a distance corresponding to the first coordination sphere, the radial distribution shows a peak which is also true for the distances corresponding to second, third, etc., coordination spheres. The fluctuations in the radial distribution function die out after the second or third peak if the material is not perfectly crystalline . From Fig. no. 5.8, the sharp relative number density peaks represent accumulation of electrolyte ions as a result of electrical interactions with both neutral and charged electrode surfaces. The regions between the peaks and the electrode surface are regarded as the impact of Helmholtz layers (HLs) in the Grahame model [130]. The ionic density gradually decreases as the distance increases from the electrode surface and ultimately to the nominal density in the bulk solution, this region is known as diffusion layer according to the classic GCS model [130]. The relative number density of O atom is predicted between 3 and 4 depending on the electrode surface

charge and conditions which is called the first water layer [132]. The density profiles of hydrogen atoms are slightly closer to the graphene surface than those of oxygen atoms, indicating the water molecules having one of its O-H bonds pointing toward the graphene surface. The first water layer hinders the hydrated cations from moving towards the charged graphene surface, resulting in the first density peaks of Na^+ located behind the first water layer. Such a concentrated hydrated cation layer is known as the outer Helmholtz layer (OHL) [133]. An ionic density peak appears next to electrode surface just after the first water layer which is called the inner Helmholtz layer (IHL) [133] which arise from the distortion of the weak hydration shell of larger sized ions when approaching to an electrode surface under a strong external electrical field. The different graphene surface charges significantly change the EDL structures as well as the first water layers.

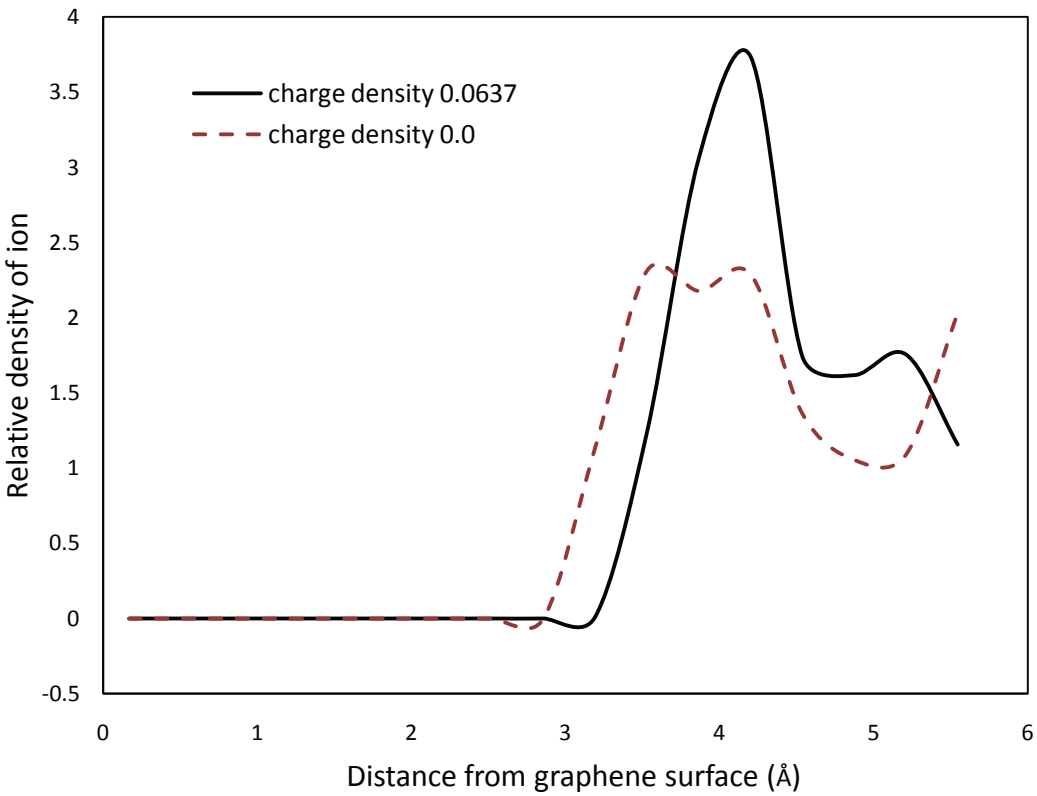

(a)

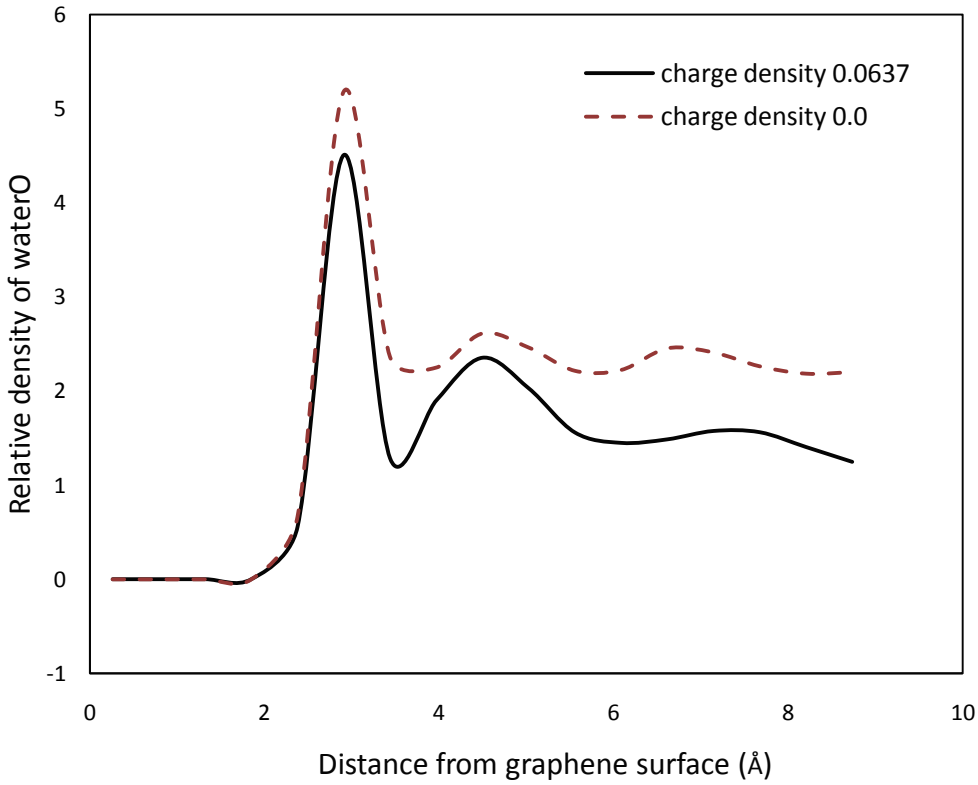

(b)

Fig 5. 9: Radial Distribution functions (RDF) of Planer model with graphene-MnO_2 electrode at 1M solution concentration (a) sodium ion, and (b) water oxygen atom.

As RDF helps to find structural changes determining the atomic positions in crystalline and amorphous materials, the effect of surface charge on EDLC structure has been studied in Fig. no. 5.9. From the graph, it can be said that with the increase of surface charge density, relative density peaks of water hydrogen and oxygen ions decreases. But in the case of electrolytes, relative density peaks of electrolyte ions (Na^+ and Cl^-) increases with increase with surface charge density. The overall impact shows a decrease in potential and as well as capacitance due to the increase of surface charge density for graphene-MnO_2 electrodes.

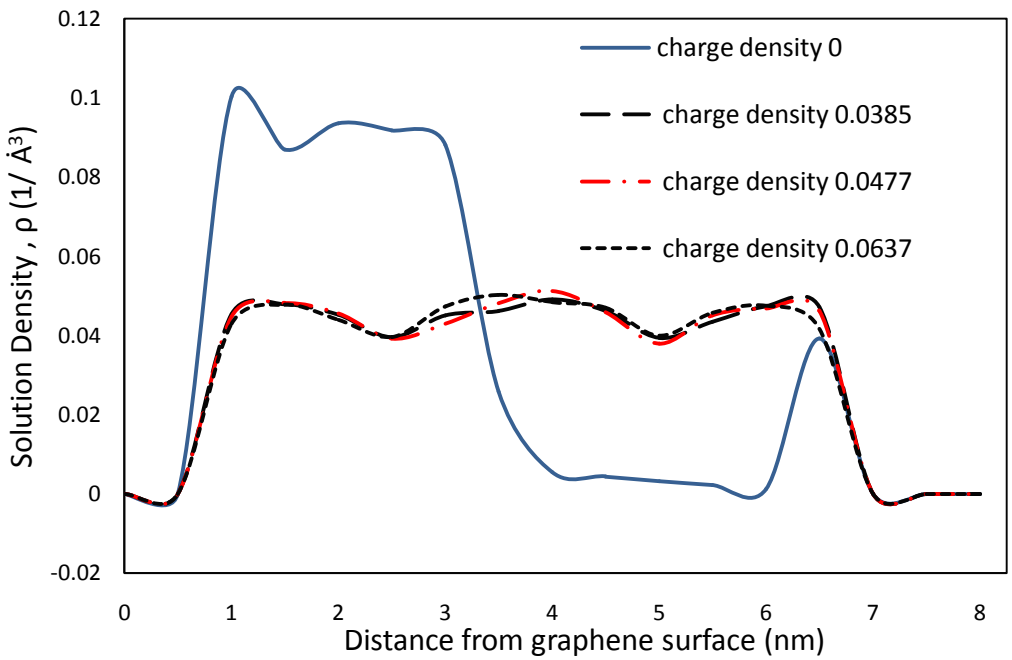

(a)

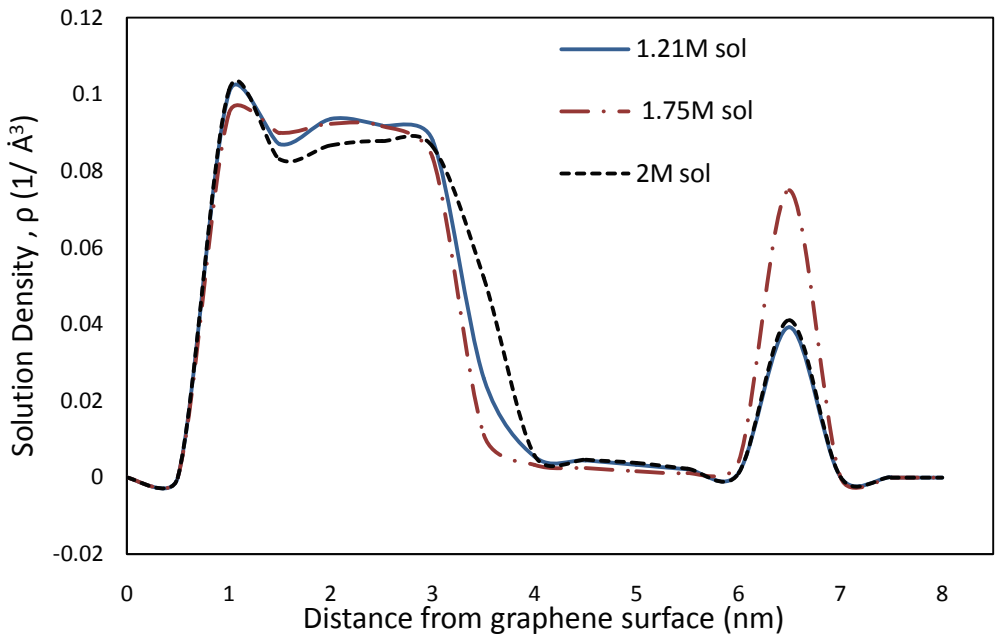

(b)

Fig 5. 10: Density profiles of Planer model with graphene-MnO_2 electrode (a) at 1M solution concentration with different surface charge density, and (b) at neutral surface with different solution concentration.

Structure of electric double layer (EDL) has largely influenced by surface charge density and solution concentration shown in Fig. no. 5.10. It is observed that with the increase of density, thickness of Helmholtz layer increases. For all the cases discussed in Fig. no. 5.10, increasing

the electrode surface charge density effects adversely on electric double layer. Due to this adverse effect of surface charge density, solution density decreases near the electrodes.

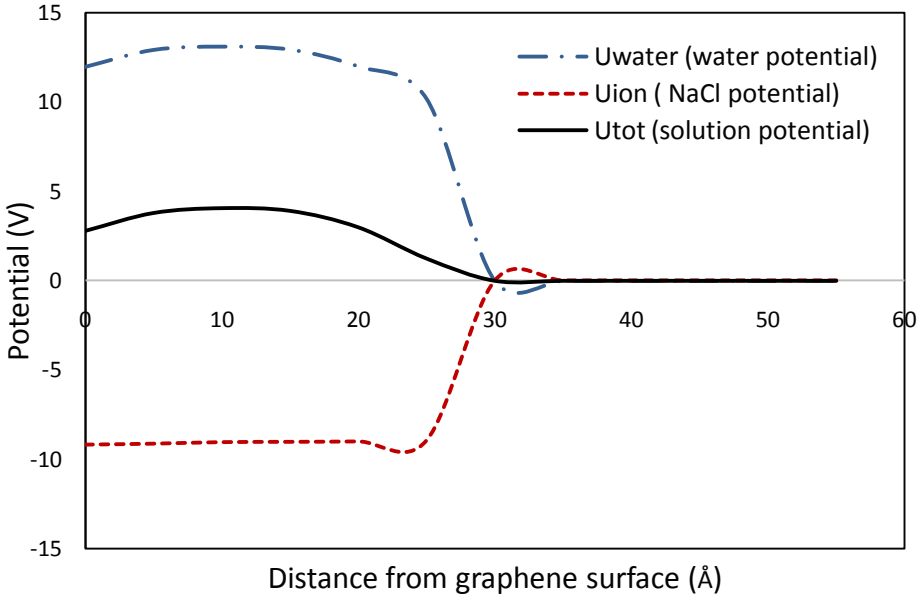

Fig 5. 11: Potential profiles of Planer model with neutral graphene-MnO_2 at 1.75M solution concentration.

The capacitance of electric double layer supercapacitor (EDLC) is voltage-dependent. The total charge stored in an EDLC structure is proportional to the square of voltage at EDLC electrodes while the charge on electrodes increases linearly with the voltage on EDLC electrodes. The Helmholtz capacitance increases linearly with the bias voltage while a sub-linear increase of total capacitance was found. The voltage on EDLC increases after the discharge of electrodes due to diffusion of charges from the electrolyte to the electrodes.

That is why Electric potential U_{tot} distribution with distance is very important to understand the performance of a supercapacitor. U_{tot} is calculated to examine the roles of electrolyte ions and water solvent on capacitance results. Resultant electric potential, U_{tot} consists of ionic EDL capacitance (U_{ion}) and water solvent capacitance (U_{water}) [130].

U_{ion} = potential from ionic Electric Double Layer and electrode surface charge

U_{water} = potential from polarized water molecules

For neutral surface with 1.75M solution in planer model, MD simulation shows that U_{water} exhibits a significant electric potential plateau between the electrode surface and the first water layer and then a sharp potential drop in U_{water} from 25 to 30 Å in Fig. no. 5.11. This drop in potential occurs due to reorientation of water molecules which creates dipoles in water molecules. U_{water} and U_{ion} have opposite signs and for higher U_{ion} values there will be

higher U_{water} values [130]. The dielectric nature of water solvent has reflected from these findings. For the U_{ion}, a linear relation is observed in the EDL region 1–20 Å from graphene surface. This region corresponds to the OHL/IHL in Fig. no. 5.10. It can be treated as a parallel plate capacitor composed of the Holmholtz layer and the charged electrode, manifested by the linear electric potential. In the diffusive layer, U_{ion} gradually approaches zero in bulk electrolyte (*i.e.*, sometime called the reference state).

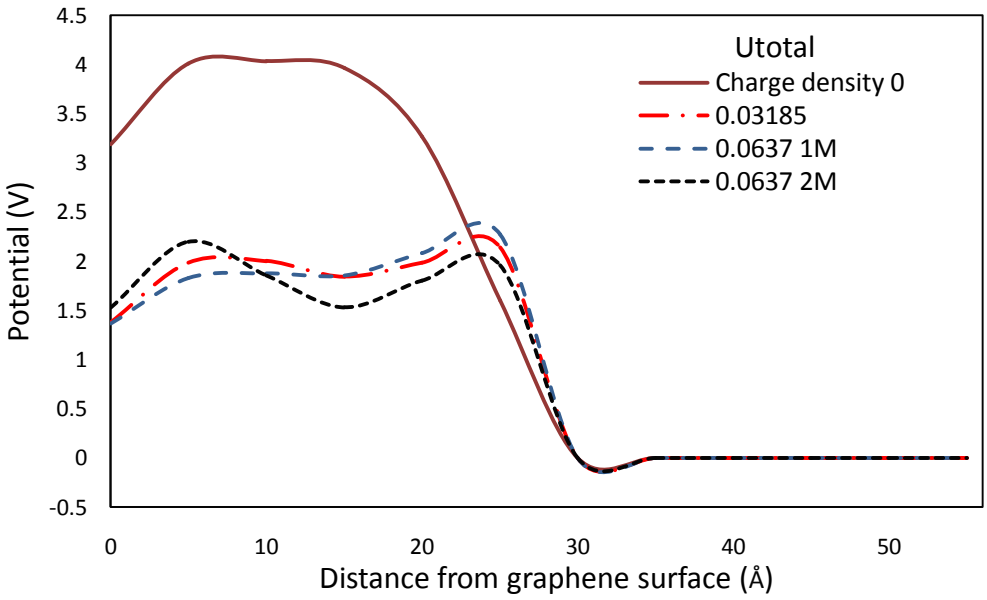

Fig 5. 12: Potential profiles of Planer model with graphene-MnO_2 at 1M solution concentration for different surface charge density.

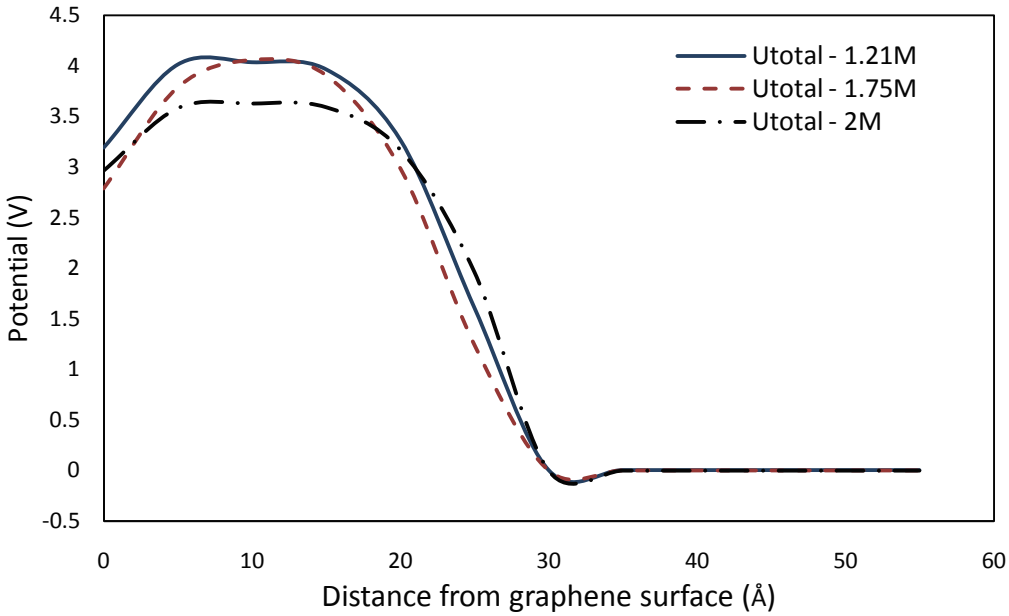

Fig 5. 13: Potential profiles of Planer model with neutral graphene-MnO_2 at different solution concentrations.

The surface charging conditions also affect the electric potential as well as the overall capacitance values. From Fig. no. 5.12, it can be seen that with the increase of surface charge density, potential area decreases which indicates that the overall capacitance also decreases. From Fig. no. 5.13, potential variation with density indicates 1.75M solution has better potential area than others as it has the highest peak and less moved to bulk region than other concentrations. The increase of U_{ion} (ion potential) is less proportional to the increase of surface charge, but proportional to the capacitive enhancement. For graphene cathode, the dielectric saturation dominates at strong surface charging and hence obtained a significantly reduced capacitance (about 30 -40%). When a high electric field is applied the water, molecules are highly oriented / ordered thus have lower capability to reorient. Dielectric constant in the high electric field is smaller than those in the weak electric field which is called 'dielectric saturation' [130].

5.2.3 'Nano Slit-pore' Model

Absence of charge-transfer resistance is one of the key criteria for high capacitance and high performance in low temperature in EDLC. Energy stored in supercapacitor is linearly proportional to the capacitance of its electrode, making material optimization crucial. The capacitance of sub-nm pores is strongly potential dependent. According to the classical double layer theory, pores those size is smaller than a specific value (hence called cut-off pore width) do not contribute to the total capacitance because of electric double layer overlapping. The double layer thickness, and thus the cut-off pore width decreases with increasing electrolyte concentration.

Within the simulation box, two graphite slabs were considered facing each other along the z direction to represent slit-shaped pores. In this study, three nano-pore sizes of 3.55, 7.1, and 9.23 Å has considered. The initial configuration is built with water and ions placed outside of the slit pore, in the "bulk" region. As the simulation progresses, water and ions fill the pore. Simulations have been performed for three different surface charge densities and three different concentrations.

Partition Coefficient, PC (Γ) is the ratio of ionic concentration in the pore (C_{pore}) versus that in the bulk (C_{bulk}). C_{pore} is calculated by counting the number of electrolyte ions and water molecules in the nanoslit-pore and C_{bulk} is calculated by counting them outside the pore [134].

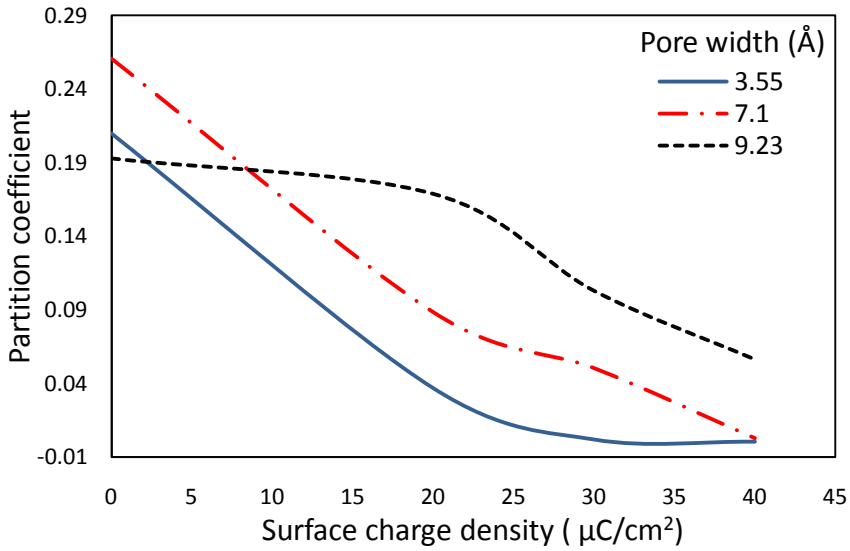

Fig 5. 14: Partition coefficients of different Nano slit–pore model at different surface charge densities.

For the simulation domain we considered, best performance of EDLC is achieved when the pores are neither too wide nor too narrow. Properties of hydrated and non-hydrated ions and their tendency of attraction due to electrostatic effect are linked to the optimum design of electrodes. Size of the ions employed in the pores has direct impact to attain enhanced partition coefficients and to determine the width of carbon slit pores. Optimal pore width size has to be determined for maximum favorable ion-ion interaction. To minimizes the energy penalty while entering the pores, hydration shell has to be mildly perturbed in an optimum way. Gogotsi and co-workers suggest that ions can penetrate sub-nanometers pores upon losing the hydration shell [135]. From Fig. no. 5.14, in case of small pores (H= 3.55 Å) the ions must lose their hydration shell, which need to overcome a large energetic barrier. Our results show that the partition coefficient is maximum for 7.1 Å pores which indicate such pores might be optimal for the production of EDLCs when aqueous NaCl solutions are employed as electrolytes in MnO_2-Graphene electrodes. The reason behind this is that these pores are larger than necessary for the complete loss of hydration shell for NaCl electrolytes and because the partition coefficient obtained is much larger than that obtained for narrower as well as wider pores. This phenomenon is analogous to the capillary action of fluid. Capillary action consists of adhesion and cohesion force of fluid which causes an upward motion in capillary tube. Best performance of capillary action is achieved if the diameter of the capillary tube is not too wide or too narrow. Smaller diameter indicates more length of the capillary tube as drop in pressure of the fluid that passes through it. Again for wider diameter

capillary action cannot act properly which indicates similar type of natural phenomenon occurring in our nano slit pore model.

Both from simulation and experiment it is suggested that to design optimum electrodes for electric double layer capacitors (EDLC), the properties of the hydrated and nonhydrated ions, and their tendency to associate because of electrostatic effects have to be carefully considered [134]. The width of the carbon-slit pores necessary to attain enhanced partition coefficients most likely depends on the composition of the aqueous electrolyte and, in particular, on the size of the ions employed. In our study, for NaCl electrolytes 7.1 Å nano-slit pore shows the maximum optimized performance.

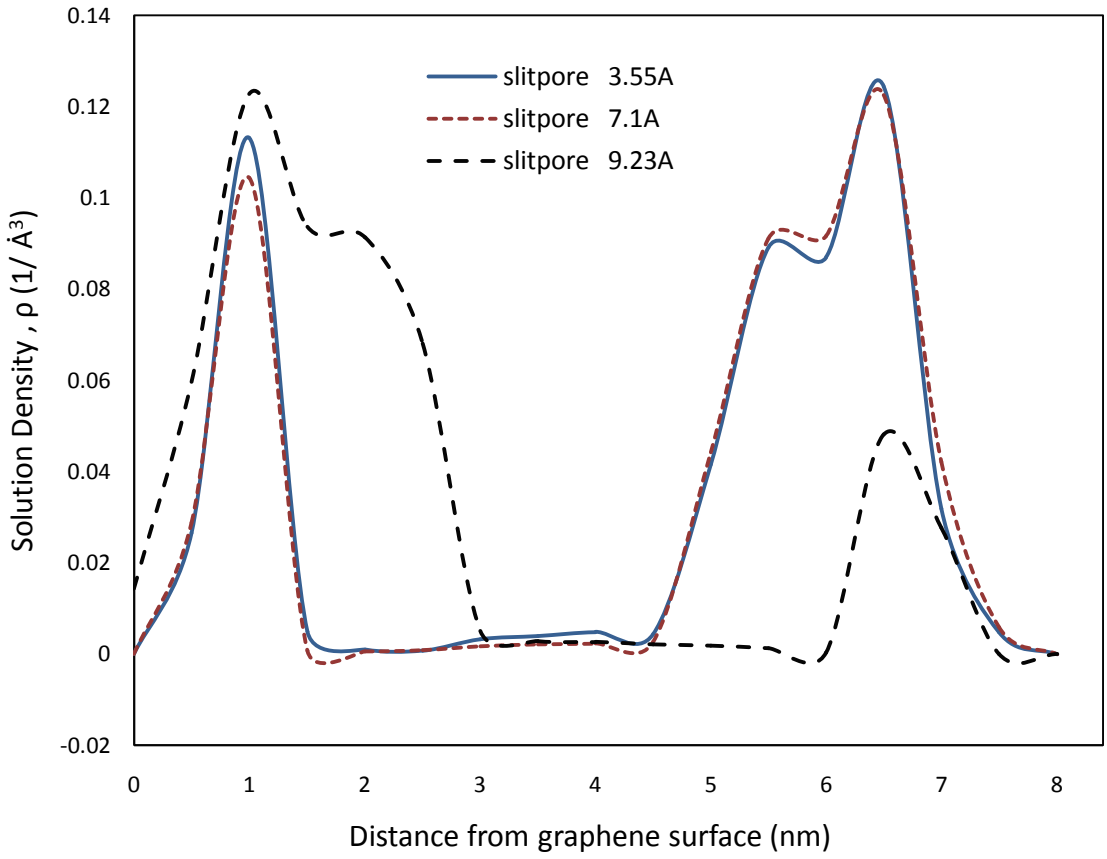

(a)

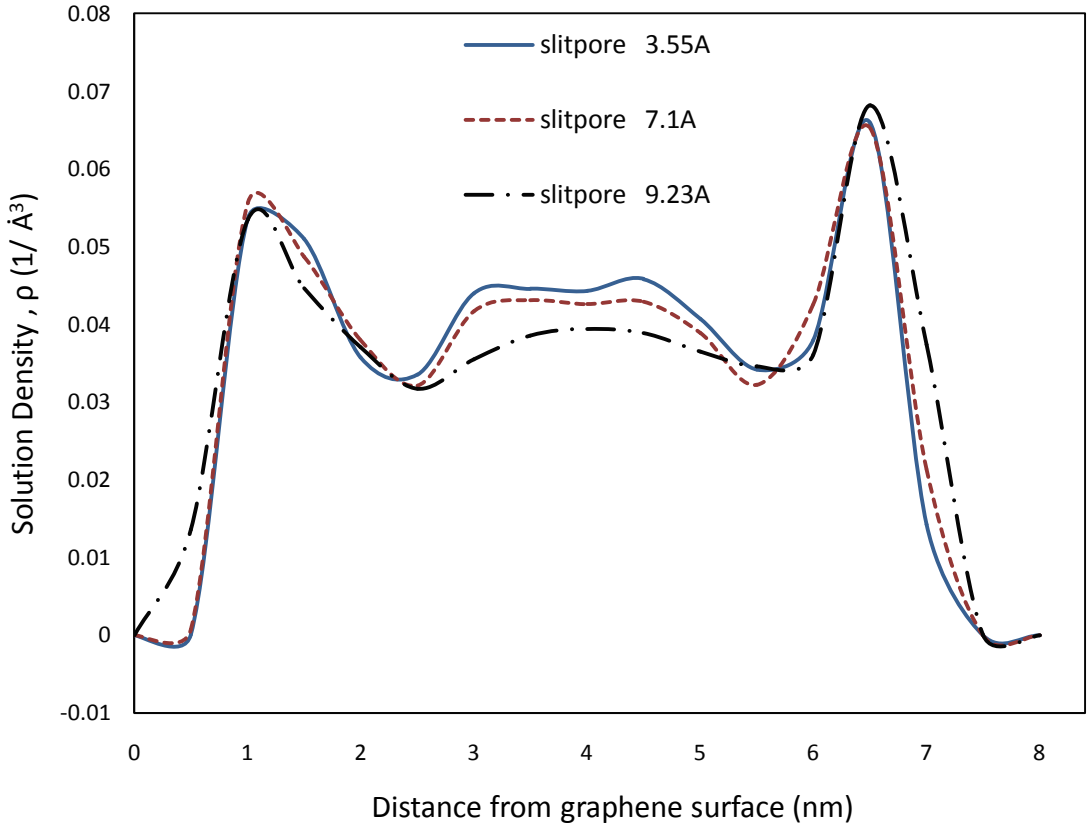

(b)

Fig 5. 15: Density profiles of different 1.21 M Nano slit–pore model of graphene-MnO_2 electrode (a) at neutral surface, and (b) at 0.0637e/C surface charge density.

For all slit-pore results including Fig. no. 5. 15, the pore depth along z direction is approximately 6.7 Å from graphene surfaces situated in the two end of simulation box. From Fig. no. 5. 15, with the increase of pore width, solution density in pore increases for both neutral and charged surface. Similar impact has been observed for different pore width. Again, with the increase of surface charge density, first density peak decreases indicating less capacitance for high surface charge conditions. The reason behind this is that the solution density will shift to bulk region whereas solution density is minimum at the bulk for neutral surface.

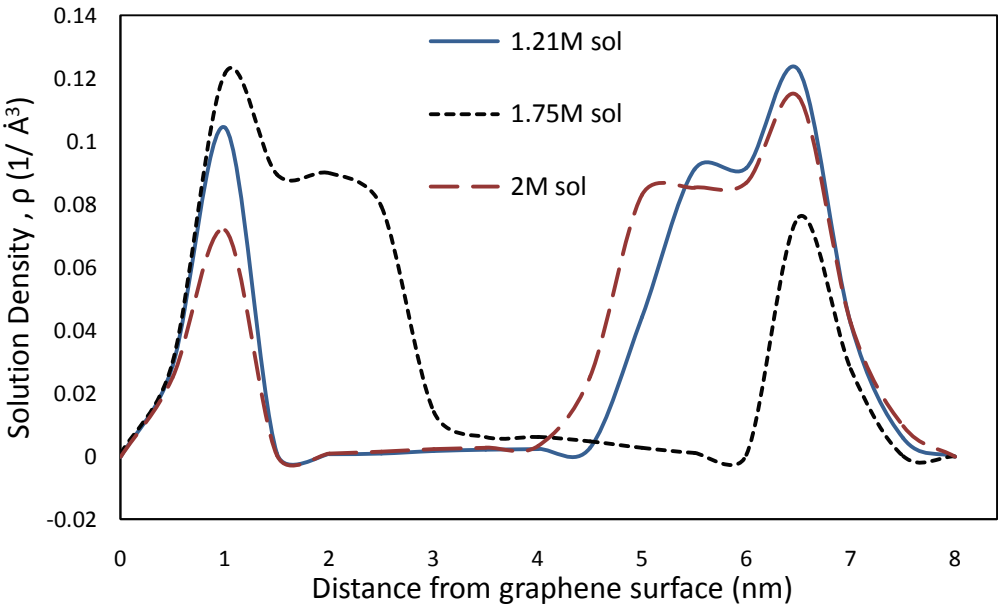

(a)

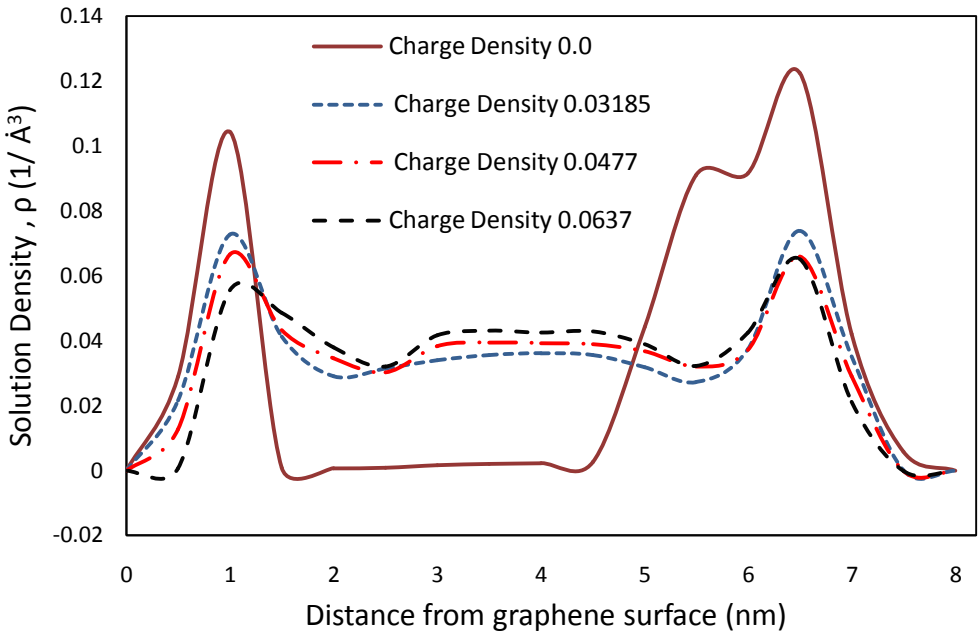

(b)

Fig 5. 16: Density profiles of different Nano slit–pore model of graphene-MnO_2 electrode (a) at different solution densities with neutral surface, and (b) at different surface charge densities with 1.21M solution concentration.

It can be said that with the increase of density of solution, solution density shifts towards bulk region after an optimum density range from Fig. no. 5.16. The optimum density range in this case is up to 1.75M for neutral surface as it shows highest density in slit-pore. Here for the 2M solution first density peak decreases and density of solution shifts to the bulk region. For

charged surfaces, with the increase of surface charge, the density of solution increases in the bulk region. As a result, density peaks decrease which indicates a reduction of capacitance.

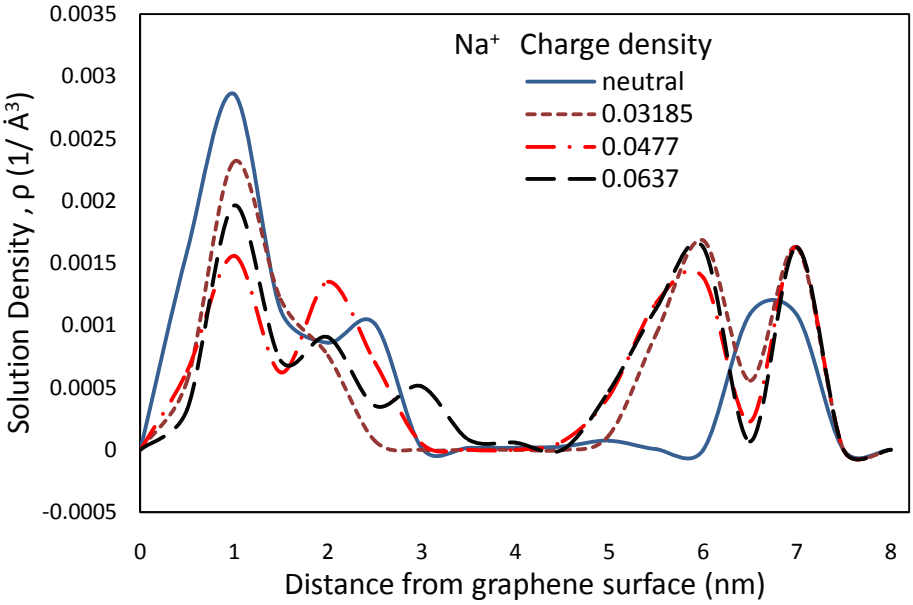

(a)

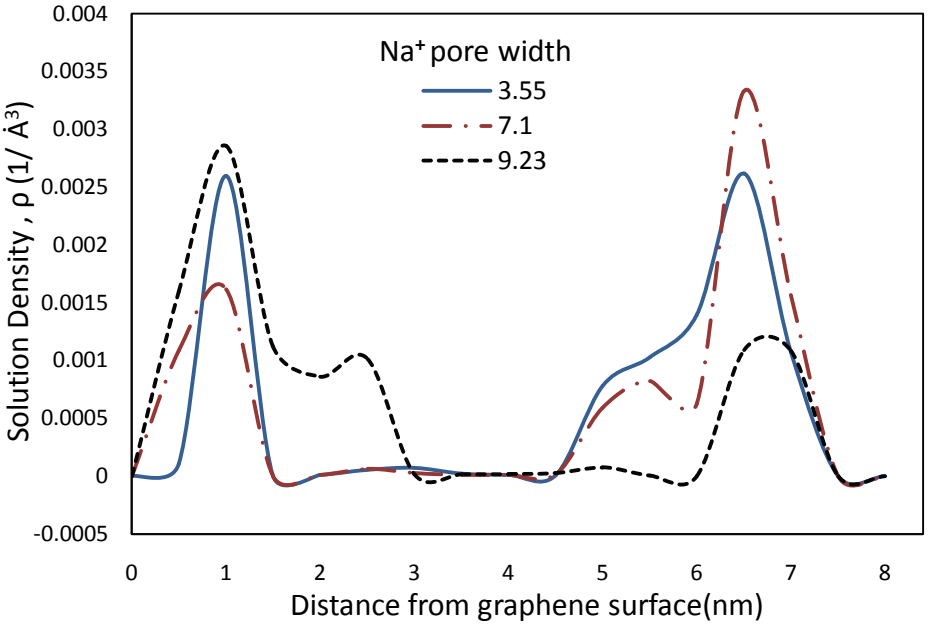

(b)

Fig 5. 17: Density profiles of Na^+ ion in 1.21 M Nano slit–pore model of graphene-MnO_2 electrode (a) at different surface charge densities with 9.23Å pore, and (b) at different pore widths.

To study specifically the electrolyte ions and their behavior in the nano slit-pore, density of Na^+ ions has been observed in Fig. no. 5.17. Density of Na^+ ion decreases with the increase of

surface charge density in the first density layer. Also, density of Na^+ ion increases with the increase of carbon slit pore width in the first density layer. This observation indicates that an optimum pore width exists for density peaks. Our results indicate that Na^+ ion is in increase at the contact of negatively charged surface in the first density layer. Both completely hydrated and partially dehydrated sodium ions clustered near the negatively charged surface.

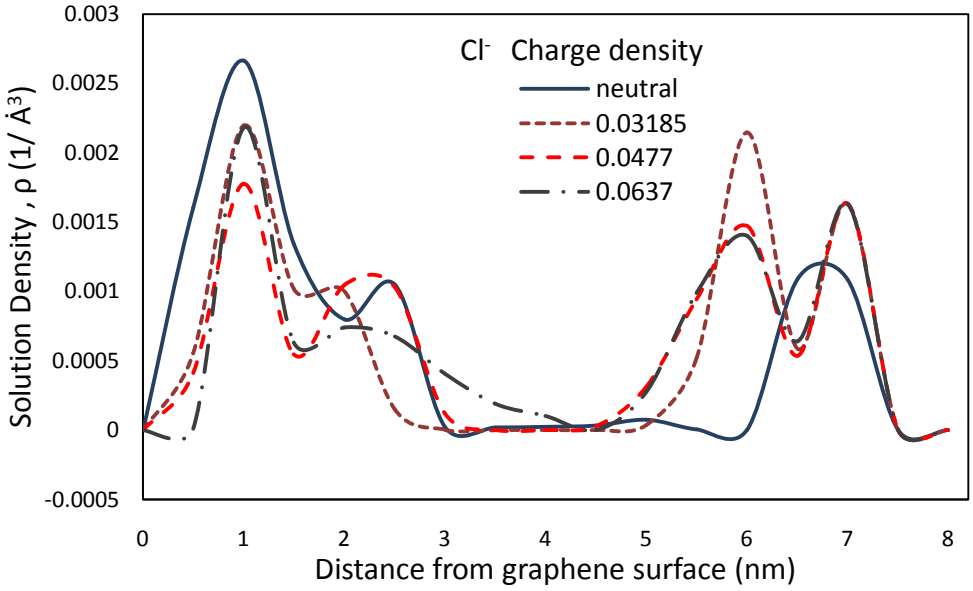

(a)

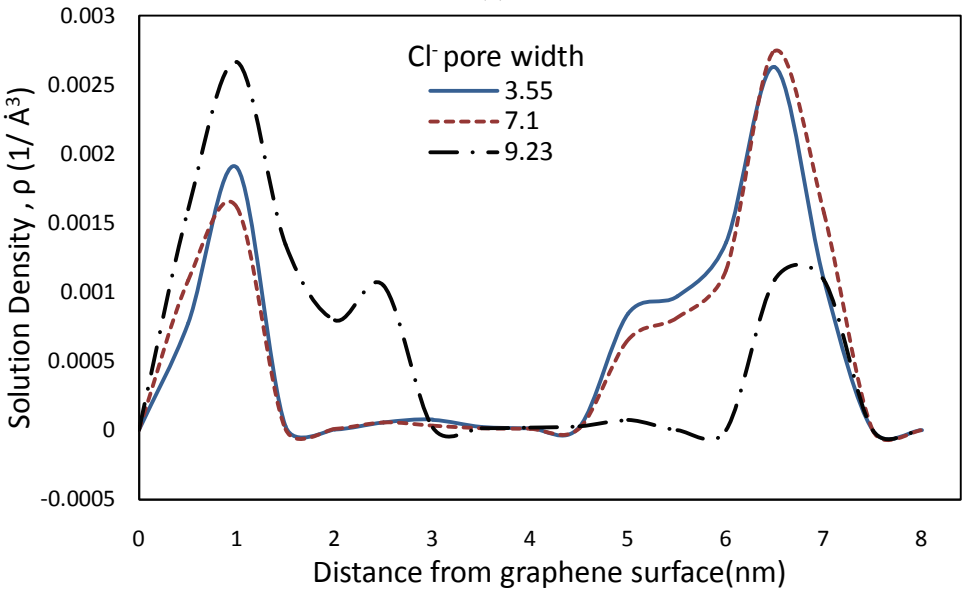

(b)

Fig 5. 18: Density profiles of Cl^- ion in 1.21M Nano slit–pore model of graphene-MnO_2 electrode (a) at different surface charge densities with 9.23Å pore, and (b) at different pore widths.

Again for the Cl^- ion of NaCl electrolytes, from Fig. no. 5.18 it can be said that density of Cl^- ion decreases with the increase of surface charge density in first density layer. Also, density of Cl^- ion increases with the increase of carbon slit pore width in the first density layer indicating an optimum pore width for chloride ions. Our results indicate that the Cl^- ion exhibits nearly similar density at the contact of negatively and positively charged surfaces in the first density layer. Both completely hydrated and partially dehydrated chloride ions clustered near both the charged surfaces.

From Figs. No. 5.17 and 5.18 it can be said that both Na^+ and Cl^- ions exhibits attraction for negatively charged surface rather than positively charged surface indicating higher capacitance for negatively charged surface.

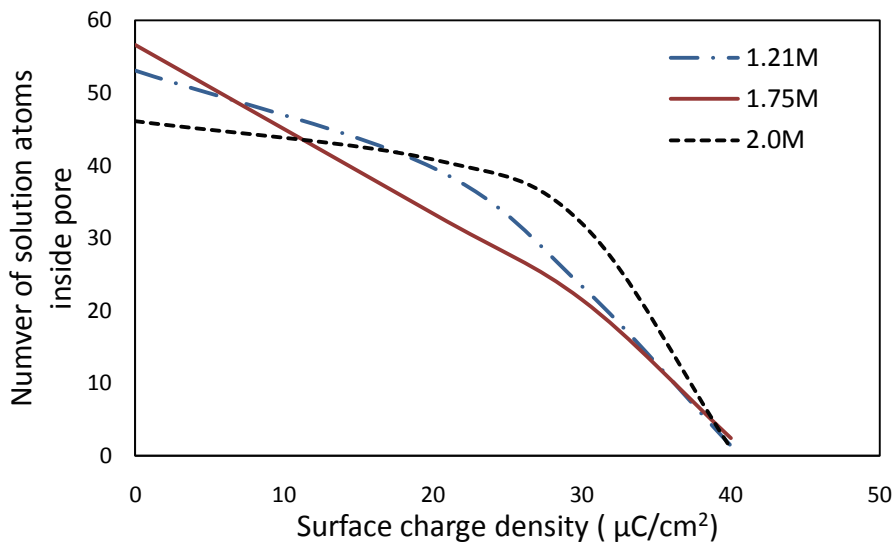

(a)

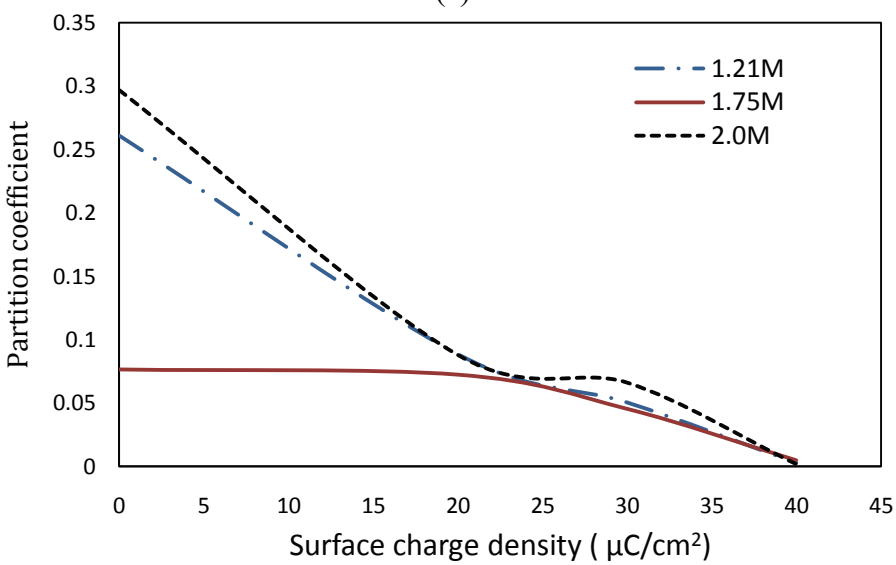

(b)

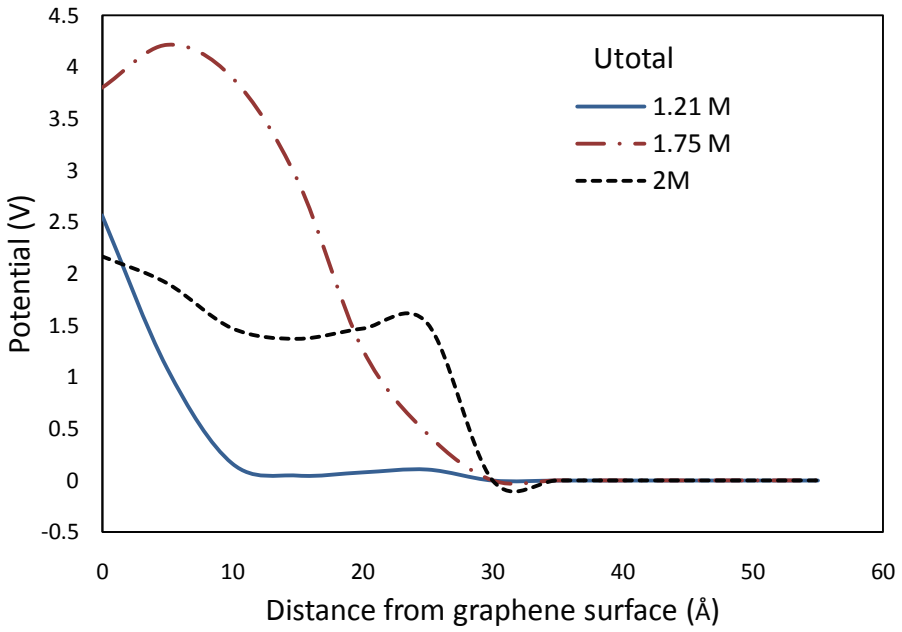

(c)

Fig 5. 19: 7.1Å Nanoslit–pore model of graphene-MnO_2 electrode (a) number of solution atoms inside pore at different surface charge densities (b) partition coefficients at different surface charge densities (c) potential profiles at different concentrations.

As the previous results indicate that 7.1Å nanoslit-pore shows better performance than others, in Fig. no. 5.19 extensive study for 7.1Å pore has been performed. From Fig. no. 5.19(a), number of atoms inside the pore decreases with increase of charge density which is maximum for 1.75M solution density at the neutral surface. With the increase of density of solution, solution density shifts towards the bulk region after an optimum density range. Here for the 2M solution first density peak decreases and density of solution shifts to bulk region. That is why fewer atoms enter inside the pore with respect to 1.75M solution. Though number of atoms inside pore is more for 1.75M than 2M solution, partition coefficient for 2M is higher because of solution density shifting to the bulk solution. From the potential curve, 1.75M solution clearly shows the highest potential peak than the other density variations for 7.1 Å pore width indicating higher capacitance than others.

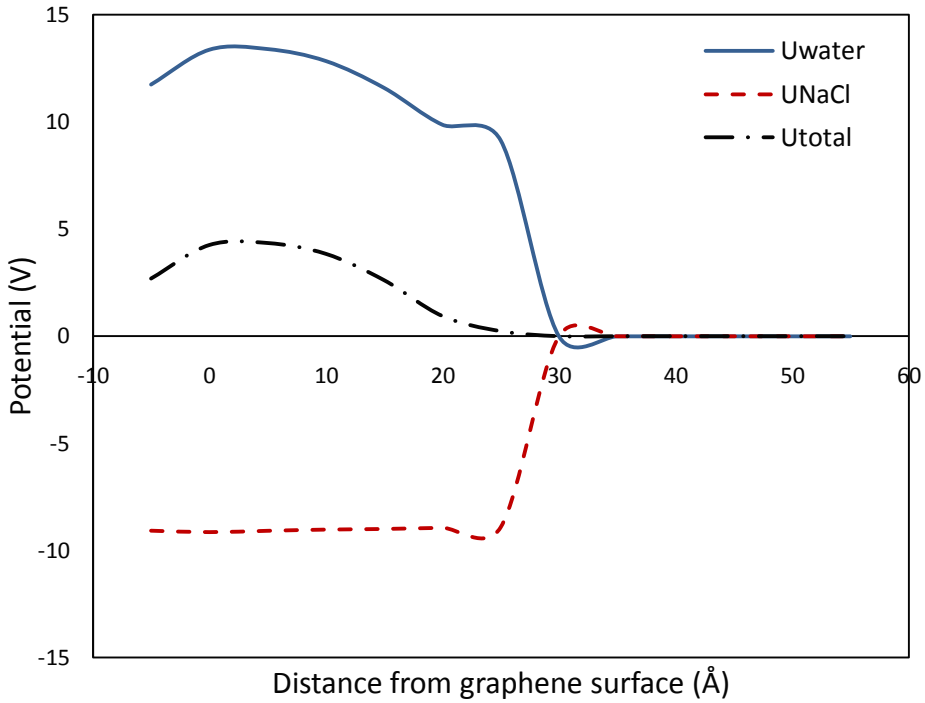
15
10
5
0
-5
-10
-15
-10
0
10
20
30
40
50
60
Potential (V)
Distance from graphene surface (Å)
Uwater
UNaCl
Utotal

(a)

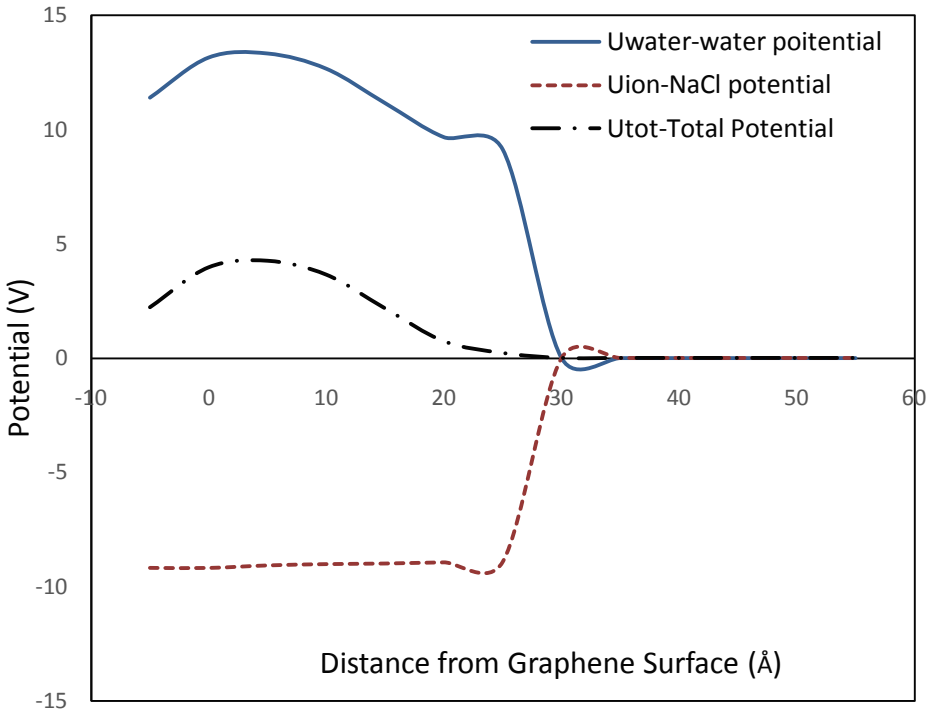
15
10
5
0
-5
-10
-15
-10
0
10
20
30
40
50
60
Potential (V)
Distance from Graphene Surface (Å)
Uwater-water poitential
Uion-NaCl potential
Utot-Total Potential

(b)

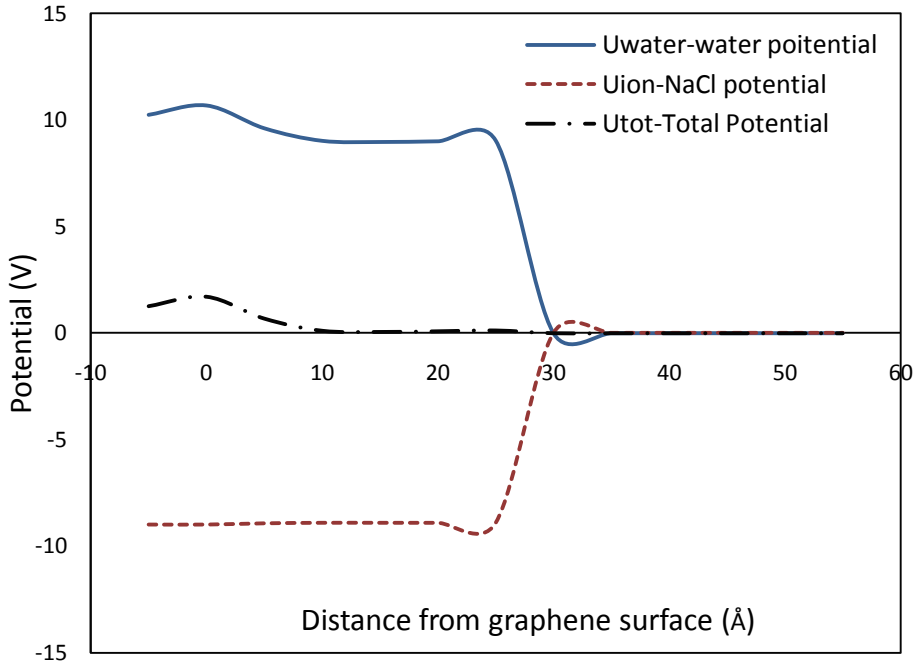
Uwater-water poitential
Uion-NaCl potential
Utot-Total Potential
Potential (V)
Distance from graphene surface (Å)
15
10
5
0
-5
-10
-15
-10
0
10
20
30
40
50
60

(c)

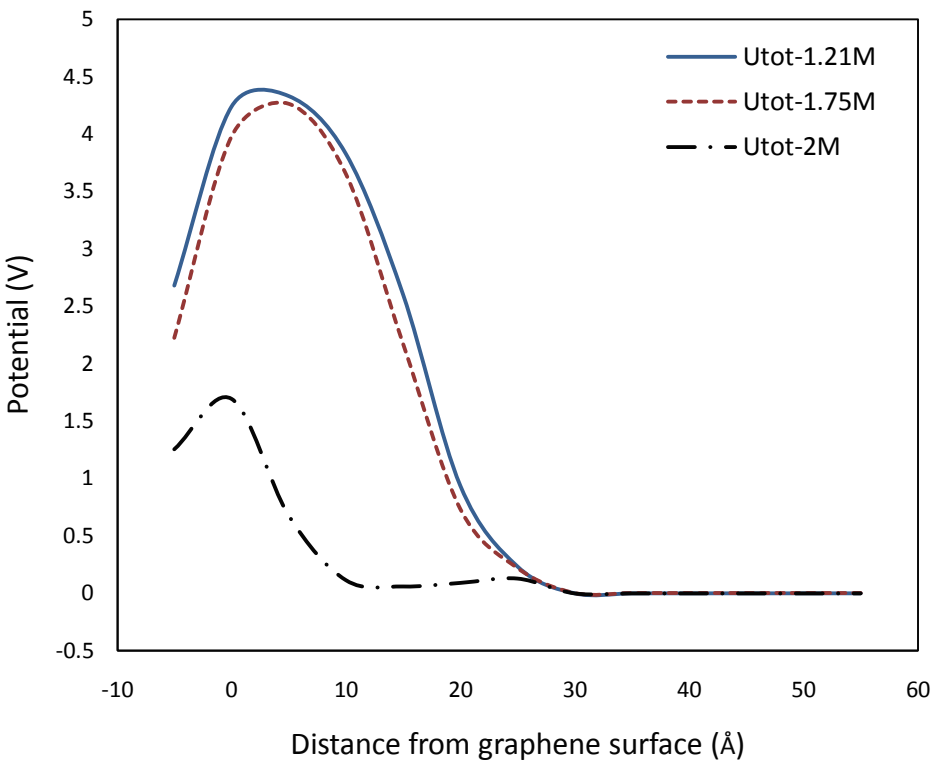
Utot-1.21M
Utot-1.75M
Utot-2M
Potential (V)
Distance from graphene surface (Å)
5
4.5
4
3.5
3
2.5
2
1.5
1
0.5
0
-0.5
-10
0
10
20
30
40
50
60

(d)

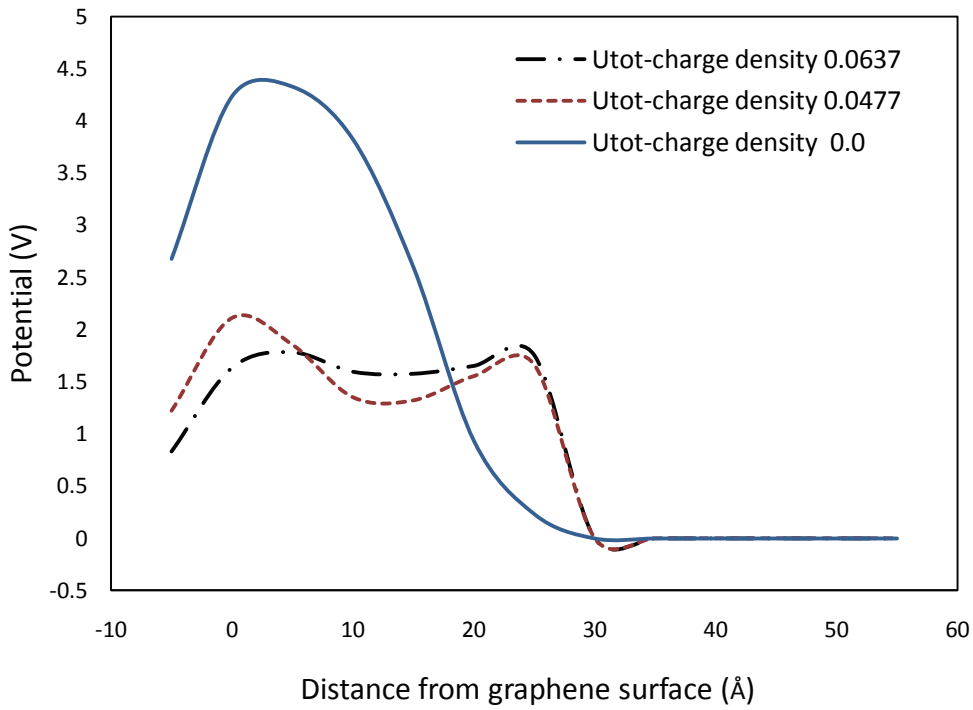

(e)

Fig 5. 20: Potential profiles of 9.23Å, 1.21 M Nano slit–pore model of graphene-MnO_2 electrode (a) at 1.21M, zero charge density, (b) at 1.75M, zero charge density, (c) at 2M solution concentration, zero charge density, (d) at different concentrations, zero charge density, and (e) at different surface charge densities, 1M solution concentration.

From Fig. no. 5.20, total potential area decreases with the increase of density of NaCl. This is because the resultant potential is the subtraction of water potential and electrolytes potential. This is because for a nanopore of 9.23Å, the numbers of electrolyte ions that can perturb the hydration shell to enter the pore increases which indicate more water hydrogen and oxygen atoms inside and near the pore. As a result, the water potential increase more than NaCl potential and that is why the total potential decreases. Again, with the increase of surface charge density, total potential area decreases. Comparing both Slitpore and non-slitpore potential curves, slitpore potential curves (peak at 4. 5V) show more potential than non slitpore cases (peak at 4V). As electrolytes enter slit-pores for this model, the potential curve starts from the pore of the electrodes and as a result total potential increases [136]. As, the Helmholtz capacitance increases linearly with the bias voltage, it can be said that capacitance increases for nano slit-pore model.

In this study, an improved electrode has been proposed which can be called the 'nano slit-pore model'. For better understanding, this improved model can be divided into two sections.

First section is the slit-pores. The slit-pores are surrounded by graphene electrode surface as border. Second section consists of graphene-MnO_2 electrode surface perpendicular to first section which is similar to without slit-pore model (planer model). In case of this model, both the inner edges of graphene and the flat surface of graphene-MnO_2 is simultaneously attracts solvent electrolytes ions. As a result, combined effect of two electrode-electrolytes interaction will significantly increases the specific capacitance as shown in potential curves than the typical planer model.

CHAPTER 6

Conclusion and Recommendation

6.1 Conclusion

A comprehensive study for the better understanding of the graphene-MnO_2 supercapacitor has been performed using computational and experimental tools in this study. The computational analysis has been performed using molecular dynamics tool (LAMMPS) and the experimental part associates experiments like cyclic voltammetry (CV) and chronopotentiometry. The main objectives of this study are to provide the inside view of graphene-MnO_2 structure in supercapacitor applications and to provide an optimized model for better performance. From the present analysis, following conclusions can be drawn:

i. From the experimental analysis, nanostructured MnO_2 over graphene sheet shows a specific capacitance of 261 F/g at current density 0.07 $mAcm^{-2}$ which indicates a good potential of graphene-MnO_2 electrode for EDLC application. Atomistic study using MD simulation replicating the experimental study provides a better insight to optimize the system to enhance its energy storage capability.

ii. Form MD simulation, with the increase of surface charge, first density peak of solvent atoms (water) decreases for all concentrations and for all pore width due to dielectric saturation.

iii. Charging conditions affect the overall capacitance values. High electrode surface charges will enhance the attraction of counter ions towards graphene-MnO_2 electrode and thus reduce the thickness of EDLs.

iv. Higher surface charging condition will reduce the water dielectric constants and thus cause a significant drop of capacitance, which is also observed within the experiments.

v. Enhanced partition coefficient indicates higher specific capacitance which depends on optimum pore width, composition of aqueous electrolytes and size of ions.

vi. The MnO_2-graphene electrode demonstrates outstanding capacitive behavior with low charge transfer resistance owing to the double layer charge storage and also with the

implementation of unique pore structure (nanopores). The high surface area resulted from nanopores was very beneficial for the accumulation of electrolyte ions.

vii. The slitpore model studied in this work offers an improved design which consists of two sections. First section is the pores with graphene electrode surface as border. Second section consists of graphene-MnO_2 electrode surface perpendicular to first section which is similar to without slitpore (planer) model. Combined effect of two electrode-electrolytes interaction significantly increases the specific capacitance.

viii. Thinner EDL from electrolytes ion will provide small electrolyte potential (U_{ion}), thus a reduction in dielectric constant that largely cancels out the beneficial effect on capacitance from a thinner EDL.

ix. The water solvent also plays an important role in determining the capacitance values at graphene-MnO_2 cathodes and anodes. NaCl has a weaker electrolyte potential (U_{ion}) of graphene-MnO_2 anode than that of graphene-MnO_2 cathode, yet the total potential (U_{tot}) shows an opposite trend. This is because the calculated dielectric constants of water (ε_{water}) in anode side are significantly lower than the results for that in cathode. This might be understood in terms of the re-orientation of the water molecules in the first water layer under different electrical fields. The water molecules in the first water layer naturally have one of its O–H bonds pointing toward the graphene-MnO_2 surface (with zero charge). At the anode surface, the positive charge has to overcome such a tendency to re-orientate the O-H bond pointing away from the anode surface. In other words, the water molecules near the anode surface are relatively more difficult to be polarized and thus the dielectric constant is smaller. In the end, the calculated capacitance values of graphene-MnO_2 anodes are lower than that of cathodes.

x. In the diffusive layer, U_{ion} gradually approaches the reference state (i.e., zero in bulk electrolyte).

xi. Our findings clearly highlight that the inclusion slitpore using edged efects in graphene-MnO_2 electrodes can dramatically improve EDL capacitance and therefore the overall performance of supercapacitors.

6.2 Recommendation

The following recommendations can be suggested for further work for analyzing atomistic structure of EDLC in a more comprehensive manner:

i. The present study has adopted constant surface charge method for the simulation domain though constant potential simulations can provide more reasonable double layer relaxation times. As constant potential simulations require high computational power, future studies might include this method to achieve more accurate results for ion-ion interaction.

ii. The nano-slit pore model developed in this present study should be studied with different electrolytes and with larger simulation domain to understand its maximum capability for capacitance enhancement.

iii. The present study has incorporated MnO_2 layer over graphene sheet and observed improvement of energy storage performance. Incorporating MnO_2 inside the pore of nano-slit pore model can be another potential research idea in the field of improving performance of electric double layer supercapacitor.

iv. Specific capacitance may be calculated from the dielectric constant and layer thickness using different mean-field theory (MFT) such as the Gouy–Chapman (GC) EDL model and Gouy–Chapman–Stern (GCS) model which can give further information to compare the performance of simulation models.

REFERENCES

[1] Simon, P., and Gogotsi, Y., "Materials for electrochemical capacitors.", *Nature Materials*, no. **7**, pp. 845–854, 2008.

[2] Miller, J. R., and Simon, P., "Electrochemical Capacitors for Energy Management," *Science*, vol. 321, no. 5889, pp. 651–652, Aug. 2008.

[3] Zhai, Y., Dou, Y., Zhao, D., Fulvio, P. F., Mayes, R. T., and Dai, S., "Carbon Materials for Chemical Capacitive Energy Storage," *Adv. Mater.*, vol. 23, no. 42, pp. 4828–4850, Nov. 2011.

[4] Zheng, J. P., "Theoretical Energy Density for Electrochemical Capacitors with Intercalation Electrodes," *J. Electrochem. Soc.*, vol. 152, no. 9, pp. A1864–A1869, Sep. 2005.

[5] Nelson, P. A., and Owen, J. R., "A High-Performance Supercapacitor/Battery Hybrid Incorporating Templated Mesoporous Electrodes," *J. Electrochem. Soc.*, vol. 150, no. 10, pp. A1313–A1317, Oct. 2003.

[6] Kim, I. H., and Kim, K.B., "Electrochemical Characterization of Hydrous Ruthenium Oxide Thin-Film Electrodes for Electrochemical Capacitor Applications," *J. Electrochem. Soc.*, vol. 153, no. 2, pp. A383–A389, Feb. 2006.

[7] Pandolfo, A. G., and Hollenkamp, A. F., "Carbon properties and their role in supercapacitors," *J. Power Sources*, vol. 157, no. 1, pp. 11–27, Jun. 2006.

[8] Wu, X. L., and Xu, A.W., "Carbonaceous hydrogels and aerogels for supercapacitors," *J. Mater. Chem. A*, vol. 2, no. 14, pp. 4852–4864, Mar. 2014.

[9] Bard, A. J., and Faulkner, L. R.,"Electrochemical Methods: Fundamentals and Applications, 2nd Edition," *Wiley.com*, December 2000.

[10] "The Electrical Double Layer," Retrieved February 11, 2019 from https://www.ceb.cam.ac.uk/research/groups/rg-eme/Edu/the-electrical-double-layer.

[11] Yike, H., Xiaohong, L., Shu, L., and Tianying., Y., " Development of mean-field electrical double layer theory.", *Chinese Physics B*, 25(1), 2016.

[12] Chmiola, J., Yushin, G., Gogotsi, Y., Portet, C., Simon, P., and Taberna, P. L., "Anomalous increase in carbon capacitance at pore sizes less than 1 nanometer," *Science*, vol. 313, no. 5794, pp. 1760–1763, Sep. 2006.

[13] Chapman, D. L., "LI. A contribution to the theory of electrocapillarity," *Lond. Edinb. Dublin Philos. Mag. J. Sci.*, vol. 25, no. 148, pp. 475–481, Apr. 1913.

[14] Stern, O., "Zur Theorie Der Elektrolytischen Doppelschicht," *Z. Für Elektrochem. Angew. Phys. Chem.*, vol. 30, no. 21–22, pp. 508–516, 1924.

[15] Pan, H., Li, J., and Feng, Y., "Carbon Nanotubes for Supercapacitor," *Nanoscale Res. Lett.*, vol. 5, no. 3, p. 654, Mar. 2010.

[16] Helmholtz, H., "Studien über electrische Grenzschichten," *Ann. Phys.*, vol. 243, no. 7, pp. 337–382, Jan. 1879.

[17] Bagotsky, V. S., "Fundamentals of Electrochemistry, 2nd Edition," *Wiley.com*, November 2005.

[18] Uzunoglu, M., and Alam, M. S., "Modeling and Analysis of an FC/UC Hybrid Vehicular Power System Using a Novel-Wavelet-Based Load Sharing Algorithm," *IEEE Trans. Energy Convers.*, vol. 23, pp. 263–272, Mar. 2008.

[19] Thounthong, P., Chunkag, V., Sethakul, P., Davat, B., and Hinaje, M., "Comparative Study of Fuel-Cell Vehicle Hybridization with Battery or Supercapacitor Storage Device," *IEEE Trans. Veh. Technol.*, vol. 58, no. 8, pp. 3892–3904, Oct. 2009.

[20] Wang, G., Zhang, L., and Zhang, J., "A review of electrode materials for electrochemical supercapacitors," *Chem. Soc. Rev.*, vol. 41, no. 2, pp. 797–828, Jan. 2012.

[21] Burke, A., "Ultracapacitors: why, how, and where is the technology," *J. Power Sources*, vol. 91, no. 1, pp. 37–50, Nov. 2000.

[22] Miller, J.R. and Burke, A.F., "Electrochemical capacitors: challenges and opportunities for real-world applications. ", *The Electrochemical Society Interface*, no. 1, p.53, 2008.

[23] Chuang, C.M., Huang, C.W., Teng, H., and Ting, J.M., "Effects of Carbon Nanotube Grafting on the Performance of Electric Double Layer Capacitors," *Energy Fuels*, vol. 24, no. 12, pp. 6476–6482, Dec. 2010.

[24] Lai, J., Levy, S., and Rose, M. F., "High energy density double-layer capacitors for energy storage applications," *IEEE Aerosp. Electron. Syst. Mag.*, vol. 7, no. 4, pp. 14–19, Apr. 1992.

[25] Chen, H., Cong, T.N., Yang, W., Tan, C., Li, Y. and Ding, Y., "Progress in electrical energy storage system: A critical review," *Progress in natural science*, no. 3, pp.291-312, 2009.

[26] Kötz, R., and Carlen, M., "Principles and applications of electrochemical capacitors," *Electrochimica Acta*, vol. 45, no. 15, pp. 2483–2498, May 2000.

[27] Zhai, Y., Dou, Y., Zhao, D., Fulvio, P. F., Mayes, R. T., and Dai, S., "Carbon Materials for Chemical Capacitive Energy Storage," *Adv. Mater.*, vol. 23, no. 42, pp. 4828–4850, Nov. 2011.

[28] Xie, X. and Gao, L., "Characterization of a manganese dioxide/carbon nanotube composite fabricated using an in situ coating method," *Carbon*, vol. 45, no. 12, pp. 2365–2373, Oct. 2007.

[29] Dong, X., Shen, W., Gu, J., Xiong, L., Zhu, Y., Li, H., and Shi, J., "MnO_2-embedded-in-mesoporous-carbon-wall structure for use as electrochemical capacitors," *J. Phys. Chem. B*, vol. 110, no. 12, pp. 6015–6019, Mar. 2006.

[30] Patel, M. N., Wang, X., Wilson, B., Ferrer, D. A., Dai, S., Stevenson, K. J., and Johnston, K. P., "Hybrid MnO_2–disordered mesoporous carbon nanocomposites: synthesis and characterization as electrochemical pseudocapacitor electrodes," *J. Mater. Chem.*, vol. 20, no. 2, pp. 390–398, Dec. 2009.

[31] Kong, X., Lu, D., Liu, Z., and Wu, J., "Molecular dynamics for the charging behavior of nanostructured electric double layer capacitors containing room temperature ionic liquids," *Nano Res.*, vol. 8, no. 3, pp. 931–940, Mar. 2015.

[32] Fedorov, M. V., and Kornyshev, A. A., "Ionic Liquids at Electrified Interfaces," *Chem. Rev.*, vol. 114, no. 5, pp. 2978–3036, Mar. 2014.

[33] Péan, C., Merlet, C., Rotenberg, B., Madden, P. A., Taberna, P.L., Daffos, B., Salanne, M., and Simon, P., "On the dynamics of charging in nanoporous carbon-based supercapacitors.," *ACS Nano*, vol. 8, no. 2, pp. 1576–1583, Feb. 2014.

[34] Kondrat, S., Wu, P., Qiao, R., and Kornyshev, A. A., "Accelerating charging dynamics in subnanometre pores," *Nat. Mater.*, vol. 13, no. 4, pp. 387–393, Apr. 2014.

[35] Kondrat, S., Pérez, C. R., Presser, V., Gogotsi, Y., and Kornyshev, A. A., "Effect of

pore size and its dispersity on the energy storage in nanoporous supercapacitors," *Energy Environ. Sci.*, vol. 5, no. 4, pp. 6474–6479, Mar. 2012.

[36] Aparicio, S., and Atilhan, M., "Choline-Based Ionic Liquids on Graphite Surfaces and Carbon Nanotubes Solvation: A Molecular Dynamics Study," *J. Phys. Chem. C*, vol. 116, no. 22, pp. 12055–12065, Jun. 2012.

[37] Burt, R., Birkett, G., and Zhao, X. S., "A review of molecular modelling of electric double layer capacitors," *Phys. Chem. Chem. Phys.*, vol. 16, no. 14, pp. 6519–6538, Mar. 2014.

[38] Merlet, C., Rotenberg, B., Madden, P. A., Taberna, P.L., Simon, P., Gogotsi, Y., and Salanne, M., "On the molecular origin of supercapacitance in nanoporous carbon electrodes," *Nat. Mater.*, vol. 11, no. 4, pp. 306–310, Mar. 2012.

[39] Nishihara, H., Itoi, H., Kogure, T., Hou, PX., Touhara, H., Okino, F., and Kyotani, T., "Investigation of the Ion Storage/Transfer Behavior in an Electrical Double-Layer Capacitor by Using Ordered Microporous Carbons as Model Materials," *Chem. – Eur. J.*, vol. 15, no. 21, pp. 5355–5363, 2009.

[40] Largeot, C., Portet, C., Chmiola, J., Taberna, P.L., Gogotsi, Y., and Simon, P., "Relation between the Ion Size and Pore Size for an Electric Double-Layer Capacitor," *J. Am. Chem. Soc.*, vol. 130, no. 9, pp. 2730–2731, Mar. 2008.

[41] Chmiola, J., Yushin, G., Gogotsi, Y., Portet, C., Simon, P., and Taberna, P. L., "Anomalous increase in carbon capacitance at pore sizes less than 1 nanometer," *Science*, vol. 313, no. 5794, pp. 1760–1763, Sep. 2006.

[42] Huang, J., Sumpter, B. G., and Meunier, V., "Theoretical model for nanoporous carbon supercapacitors," *Angew. Chem. Int.* Ed Engl., vol. 47, no. 3, pp. 520–524, 2008.

[43] Henderson, D., "Oscillations in the capacitance of a nanopore containing an electrolyte due to pore width and nonzero size ions.," *J. Colloid Interface Sci.*, vol. 374, no. 1, pp. 345–347, May 2012.

[44] Yang, L., Fishbine, B. H., Migliori, A., and Pratt, L. R., "Molecular simulation of electric double-layer capacitors based on carbon nanotube forests," *J. Am. Chem. Soc.*, vol. 131, no. 34, pp. 12373–12376, Sep. 2009.

[45] Wang, Y., Jiang, W., Yan, T., and Voth, G. A., "Understanding Ionic Liquids through Atomistic and Coarse-Grained Molecular Dynamics Simulations," *Acc. Chem. Res.*, vol. 40, no. 11, pp. 1193–1199, Nov. 2007.

[46] Merlet, C., Péan, C., Rotenberg, B., Madden, P. A., Simon, P., and Salanne, M., "Simulating Supercapacitors: Can We Model Electrodes As Constant Charge Surfaces?," *J.*

Phys. Chem. Lett., vol. 4, no. 2, pp 264–268, 2013.

[47] Parr, R.G., and Yang, W.(1989), *Density-functional theory of atoms and molecules.*, Oxford University Press, New York, Oxford.

[48] Taboada-Serrano, P., Yiacoumi, S., and Tsouris, C., "Behavior of mixtures of symmetric and asymmetric electrolytes near discretely charged planar surfaces: A Monte Carlo study," *J. Chem. Phys.*, vol. 123, no. 5, p. 054703, Aug. 2005.

[49] Wang, H., and Pilon, L., "Mesoscale modeling of electric double layer capacitors with three-dimensional ordered structures," *J. Power Sources*, vol. 221, pp. 252–260, Jan. 2013.

[50] Wang, H., Varghese, J., and Pilon, L., "Simulation of electric double layer capacitors with mesoporous electrodes: Effects of morphology and electrolyte permittivity," *Electrochimica Acta*, vol. 56, no. 17, pp. 6189–6197, Jul. 2011.

[51] Lukatskaya, M. R., Mashtalir, O., Ren, C. E., Dall'Agnese, Y., Rozier, P., Taberna, P. L., Naguib, M., Simon, P., Barsoum, M. W., Gogotsi, Y.,"Cation intercalation and high volumetric capacitance of two-dimensional titanium carbide," *Science*, vol. 341, no. 6153, pp. 1502–1505, Sep. 2013.

[52] Spoel, D. V. D., Maaren, P. J. V., and Berendsen, H. J. C., "A systematic study of water models for molecular simulation: Derivation of water models optimized for use with a reaction field," *J. Chem. Phys.*, vol. 108, no. 24, pp. 10220–10230, Jun. 1998.

[53] Tang, Y. W., Chan, K.Y., and Szalai, I., "Structural and Transport Properties of an SPC/E Electrolyte in a Nanopore," *J. Phys. Chem. B*, vol. 108, no. 47, pp. 18204–18213, Nov. 2004.

[54] Feng, G., Qiao, R., Huang, J., Sumpter, B. G., and Meunier, V., "Ion Distribution in Electrified Micropores and Its Role in the Anomalous Enhancement of Capacitance," *ACS Nano*, vol. 4, no. 4, pp. 2382–2390, Apr. 2010.

[55] Feng, G., Qiao, R., Huang, J., Sumpter, B. G., and Meunier, V., "Atomistic Insight on the Charging Energetics in Subnanometer Pore Supercapacitors," *J. Phys. Chem. C*, vol. 114, no. 41, pp. 18012–18016, Oct. 2010.

[56] Wander, M. C. F., and Shuford, K. L., "Molecular Dynamics Study of Interfacial Confinement Effects of Aqueous NaCl Brines in Nanoporous Carbon," *J. Phys. Chem. C*, vol. 114, no. 48, pp. 20539–20546, Dec. 2010.

[57] Kalluri, R. K., Konatham, D., and Striolo, A., "Aqueous NaCl Solutions within Charged Carbon-Slit Pores: Partition Coefficients and Density Distributions from Molecular Dynamics Simulations," *J. Phys. Chem. C*, vol. 115, no. 28, pp. 13786–13795, Jul. 2011.

[58] Lee, H. Y., and Goodenough, J. B., "Supercapacitor Behavior with KCl Electrolyte,"

J. Solid State Chem., vol. 144, no. 1, pp. 220–223, Apr. 1999.

[59] Wang, G., Zhang, L., and Zhang, J., "A review of electrode materials for electrochemical supercapacitors," *Chem. Soc. Rev.*, vol. 41, no. 2, pp. 797–828, Jan. 2012.

[60] Hu, C.C., and Tsou, T.W., "Ideal capacitive behavior of hydrous manganese oxide prepared by anodic deposition," *Electrochem. Commun.*, vol. 4, no. 2, pp. 105–109, Feb. 2002.

[61] Toupin, M., Brousse, T. and Bélanger, D., "Charge storage mechanism of MnO_2 electrode used in aqueous electrochemical capacitor." *Chemistry of Materials*, no. 16, pp.3184-3190, 2004.

[62] Nakayama, M., Kanaya, T., and Inoue, R., "Anodic deposition of layered manganese oxide into a colloidal crystal template for electrochemical supercapacitor," *Electrochem. Commun.*, vol. 9, no. 5, pp. 1154–1158, May 2007.

[63] Chang, J.K., Huang, C.H., Lee, M.T., Tsai, W.T., Deng, M.J., and Sun, I.W., "Physicochemical factors that affect the pseudocapacitance and cyclic stability of Mn oxide electrodes," *Electrochimica Acta*, vol. 54, no. 12, pp. 3278–3284, Apr. 2009.

[64] Wei, J., Nagarajan, N., and Zhitomirsky, I., "Manganese oxide films for electrochemical supercapacitors," *J. Mater. Process. Technol.*, vol. 186, no. 1, pp. 356–361, May 2007.

[65] Chang, J.K., Chen, Y.L., and Tsai, W.T., "Effect of heat treatment on material characteristics and pseudo-capacitive properties of manganese oxide prepared by anodic deposition," *J. Power Sources*, vol. 135, no. 1, pp. 344–353, Sep. 2004.

[66] Donne, S.W., Hollenkamp, A. F., and Jones, B. C., "Structure, morphology and electrochemical behaviour of manganese oxides prepared by controlled decomposition of permanganate," *J. Power Sources*, vol. 195, no. 1, pp. 367–373, Jan. 2010.

[67] Subramanian, V., Zhu, H., and Wei, B., "Nanostructured MnO2: Hydrothermal synthesis and electrochemical properties as a supercapacitor electrode material," *J. Power Sources*, vol. 159, no. 1, pp. 361–364, Sep. 2006.

[68] Wang, H., Lu, Z., Qian, D., Li, Y., and Zhang, W.,"Single-crystal α-MnO_2 nanorods: synthesis and electrochemical properties," *Nanotechnology*, vol. 18, no. 11, p. 115616, Feb. 2007.

[69] Chou, S., Cheng, F., and Chen, J.,"Electrodeposition synthesis and electrochemical properties of nanostructured γ-MnO_2 films," *J. Power Sources*, vol. 162, no. 1, pp. 727–734, Nov. 2006.

[70] Brousse, T., Toupin, M., Dugas, R., Athouël, L., Crosnier, O., and Bélanger, D.,

"Crystalline MnO_2 as Possible Alternatives to Amorphous Compounds in Electrochemical Supercapacitors," *J. Electrochem. Soc.*, vol. 153, no. 12, pp. A2171–A2180, Dec. 2006.

[71] Athouël, L., Moser, F., Dugas, R., Crosnier, O., Bélanger, D., and Brousse, T., "Variation of the MnO_2 Birnessite Structure upon Charge/Discharge in an Electrochemical Supercapacitor Electrode in Aqueous Na_2SO_4 Electrolyte," *J. Phys. Chem. C*, vol. 112, no. 18, pp. 7270–7277, May 2008.

[72] Beaudrouet, E., Salle, A. L. G. L., and Guyomard, D., "Nanostructured manganese dioxides: Synthesis and properties as supercapacitor electrode materials," *Electrochimica Acta*, vol. 54, no. 4, pp. 1240–1248, Jan. 2009.

[73] Wu, M.S.,"Electrochemical capacitance from manganese oxide nanowire structure synthesized by cyclic voltammetric electrodeposition," *Appl. Phys. Lett.*, vol. 87, no. 15, p. 153102, Oct. 2005.

[74] Nagarajan, N., Cheong, M., and Zhitomirsky, I., "Electrochemical capacitance of MnOx films," *Mater. Chem. Phys.*, vol. 103, no. 1, pp. 47–53, May 2007.

[75] Huang, Q., Wang, X., and Li, J., "Characterization and performance of hydrous manganese oxide prepared by electrochemical method and its application for supercapacitors," *Electrochimica Acta*, vol. 52, no. 4, pp. 1758–1762, Dec. 2006.

[76] Broughton, J. N., and Brett, M. J., "Variations in MnO_2 electrodeposition for electrochemical capacitors," *Electrochimica Acta*, vol. 50, no. 24, pp. 4814–4819, Aug. 2005.

[77] Prasad, K. R., and Miura, N., "Potentiodynamically deposited nanostructured manganese dioxide as electrode material for electrochemical redox supercapacitors," *J. Power Sources*, vol. 135, no. 1, pp. 354–360, Sep. 2004.

[78] Devaraj, S., and Munichandraiah, N., "High Capacitance of Electrodeposited MnO_2 by the Effect of a Surface-Active Agent," *Electrochem. Solid-State Lett.*, vol. 8, no. 7, pp. A373–A377, Jul. 2005.

[79] Yang, X., Wang, Y., Xiong, H., and Xia, Y., "Interfacial synthesis of porous MnO_2 and its application in electrochemical capacitor," *Electrochimica Acta*, vol. 53, no. 2, pp. 752–757, Dec. 2007.

[80] Prasad, K. R., and Miura, N., "Electrochemically synthesized MnO_2-based mixed oxides for high performance redox supercapacitors," *Electrochem. Commun.*, vol. 6, no. 10, pp. 1004–1008, Oct. 2004.

[81] Toupin, M., Brousse, T., and Bélanger, D., "Influence of Microstucture on the Charge Storage Properties of Chemically Synthesized Manganese Dioxide," *Chem. Mater.*, vol. 14, no. 9, pp. 3946–3952, Sep. 2002.

[82] Chin, S.F., Pang, S.C., and Anderson, M. A., "Material and Electrochemical Characterization of Tetrapropylammonium Manganese Oxide Thin Films as Novel Electrode Materials for Electrochemical Capacitors," *J. Electrochem. Soc.*, vol. 149, no. 4, pp. A379–A384, Apr. 2002.

[83] Taguchi, A., Inoue, S., Akamaru, S., Hara, M., Watanabe, K., and Abe, T.,"Phase transition and electrochemical capacitance of mechanically treated manganese oxides," *J. Alloys Compd.*, vol. 414, no. 1, pp. 137–141, Apr. 2006.

[84] Subramanian, V., Zhu, H., and Wei, B., "Alcohol-assisted room temperature synthesis of different nanostructured manganese oxides and their pseudocapacitance properties in neutral electrolyte," *Chem. Phys. Lett.*, vol. 453, no. 4, pp. 242–249, Mar. 2008.

[85] Pang, S.C., Anderson, M. A., and Chapman, T. W., "Novel Electrode Materials for Thin-Film Ultracapacitors: Comparison of Electrochemical Properties of Sol-Gel-Derived and Electrodeposited Manganese Dioxide," *J. Electrochem. Soc.*, vol. 147, no. 2, pp. 444–450, Feb. 2000.

[86] Xu, W., and Angell, C. A., "Weakly Coordinating Anions, and the Exceptional Conductivity of Their Nonaqueous Solutions," *Electrochem. Solid-State Lett.*, vol. 4, no. 1, pp. E1–E4, Jan. 2001.

[87] Babakhani, B., and Ivey, D. G., "Improved capacitive behavior of electrochemically synthesized Mn oxide/PEDOT electrodes utilized as electrochemical capacitors," *Electrochimica Acta*, vol. 55, no. 12, pp. 4014–4024, Apr. 2010.

[88] Zheng, H., Tang, F., Lim, M., Mukherji, A., Yan, X., Wang, L., Lu, G. Q.,"Multilayered films of cobalt oxyhydroxide nanowires/manganese oxide nanosheets for electrochemical capacitor," *J. Power Sources*, vol. 195, no. 2, pp. 680–683, Jan. 2010.

[89] Kim, H., and Popov, B. N., "Synthesis and Characterization of MnO_2-Based Mixed Oxides as Supercapacitors," *J. Electrochem. Soc.*, vol. 150, no. 3, pp. D56–D62, Mar. 2003.

[90] Li, L., Qin, Z.Y., Wang, L.F., Liu, H.J., and Zhu, M.F., "Anchoring alpha-manganese oxide nanocrystallites on multi-walled carbon nanotubes as electrode materials for supercapacitor," *J. Nanoparticle Res.*, vol. 12, no. 7, pp. 2349–2353, Sep. 2010.

[91] Xu, C.L., Bao, S.J., Kong, L.B., Li, H., and Li, H.L., "Highly ordered MnO_2 nanowire array thin films on Ti/Si substrate as an electrode for electrochemical capacitor," *J. Solid State Chem.*, vol. 179, no. 5, pp. 1351–1355, May 2006.

[92] Chang, J.K., Hsu, S.H., Tsai, W.T., and Sun, I.W., "A novel electrochemical process to prepare a high-porosity manganese oxide electrode with promising pseudocapacitive performance," *J. Power Sources*, vol. 177, no. 2, pp. 676–680, Mar. 2008.

[93] Xiao, W., Xia, H., Fuh, J. Y. H.,and Lu, L., "Growth of single-crystal α-MnO_2 nanotubes prepared by a hydrothermal route and their electrochemical properties," *J. Power Sources*, vol. 193, no. 2, pp. 935–938, Sep. 2009.

[94] Li, Y., Xie, H., Wang, J., and Chen, L., "Preparation and electrochemical performances of α-MnO_2 nanorod for supercapacitor," *Mater. Lett.*, vol. 65, no. 2, pp. 403–405, Jan. 2011.

[95] Ragupathy, P., Park, D. H., Campet, G., Vasan, H. N., Hwang, S.J., Choy, J.H., and Munichandraiah, N., "Remarkable Capacity Retention of Nanostructured Manganese Oxide upon Cycling as an Electrode Material for Supercapacitor," *J. Phys. Chem. C*, vol. 113, no. 15, pp. 6303–6309, Apr. 2009.

[96] Jiang, R., Huang, T., Liu, J., Zhuang, J., and Yu, A., "A novel method to prepare nanostructured manganese dioxide and its electrochemical properties as a supercapacitor electrode," *Electrochimica Acta*, vol. 54, no. 11, pp. 3047–3052, Apr. 2009.

[97] Nam, K.W., Lee, C.W., Yang, X.Q., Cho, B.W., Yoon, W.S., and Kim, K.B., "Electrodeposited manganese oxides on three-dimensional carbon nanotube substrate: Supercapacitive behaviour in aqueous and organic electrolytes," *J. Power Sources*, vol. 188, no. 1, pp. 323–331, Mar. 2009.

[98] Malak-Polaczyk, A., Matei-Ghimbeu, C., Vix-Guterl, C., and Frackowiak, E., "Carbon/ λ-MnO_2 composites for supercapacitor electrodes," *J. Solid State Chem. Fr.*, vol. 183, pp. 969–974, Apr. 2010.

[99] Amade, R., Jover, E., Caglar, B., Mutlu, T., and Bertran, E. "Optimization of MnO_2/vertically aligned carbon nanotube composite for supercapacitor application," *J. Power Sources*, vol. 196, no. 13, pp. 5779–5783, Jul. 2011.

[100] Gao, P.C., Lu, A.H., and Li, W.C., "Dual functions of activated carbon in a positive electrode for MnO_2-based hybrid supercapacitor," *J. Power Sources*, vol. 196, no. 8, pp. 4095–4101, Apr. 2011.

[101] Li, B., Cao, H., Shao, J., Qu, M., and Warner, J. H.,"Superparamagnetic Fe_3O_4 nanocrystals@graphene composites for energy storage devices," *J. Mater. Chem.*, vol. 21, no. 13, pp. 5069–5075, Mar. 2011.

[102] Wu, S., Chen, W., and Yan., L., "Fabrication of a 3D MnO_2/graphene hydrogel for high-performance asymmetric supercapacitors." *Journal of materials chemistry A*, no. 8, pp 2765-2772, 2014

[103] Egerton, R. F., *Electron Energy-Loss Spectroscopy in the Electron Microscope*. Springer Science & Business Media, 2011.

[104] Bell, D. C., and Garratt-Reed, A. J., *Energy Dispersive X-ray Analysis in the Electron Microscope*. Garland Science, 2003.

[105] Suryanarayana, C., and Norton, M. G., *X-Ray Diffraction: A Practical Approach*. Springer US, 1998.

[106] Wang, J., *Analytical Electrochemistry*. John Wiley & Sons, 2006.

[107] Bard, A. J., and Faulkner, L. R., "Electrochemical Methods: Fundamentals and Applications, 2nd Edition," *Wiley.com*, December 2000.

[108] Frackowiak, E., "Supercapacitors based on carbon materials and ionic liquids," *J. Braz. Chem. Soc.*, vol. 17, no. 6, 2006.

[109] Plimpton, S., "Fast Parallel Algorithms for Short-Range Molecular Dynamics," *J. Comput. Phys.*, vol. 117, pp. 1–19, 1995.

[110] Tee, L. S., Gotoh, S., and Stewart, W. E., "Molecular Parameters for Normal Fluids. Lennard-Jones 12-6 Potential," *Ind. Eng. Chem. Fundam.*, vol. 5, no. 3, pp. 356–363, Aug. 1966.

[111] "Model Box Periodic Boundary Conditions - P.B.C.," Retrieved May 9, 2019 from http://isaacs.sourceforge.net/phys/pbc.html.

[112] Pastor, R. W., Brooks, B. R., and Szabo, A., "An analysis of the accuracy of Langevin and molecular dynamics algorithms," *Mol. Phys.*, vol. 65, no. 6, pp. 1409–1419, Dec. 1988.

[113] Verlet, L., "Computer 'Experiments' on Classical Fluids. I. Thermodynamical Properties of Lennard-Jones Molecules," *Phys. Rev.*, vol. 159, no. 1, pp. 98–103, Jul. 1967.

[114] Greenspan, D.,*Particle Modeling*. Springer Science & Business Media, 2013.

[115] Hockney, R. W., Eastwood, J. W.,and Eastwood, J. W.,*Computer Simulation Using Particles*. CRC Press, 1988.

[116] Darden, T., York, D., and Pedersen, L., "Particle mesh Ewald: An N.log(N) method for Ewald sums in large systems," *J. Chem. Phys.*, vol. 98, no. 12, pp. 10089–10092, Jun. 1993.

[117] Pollock, E. L., and Glosli, J., “Comments on P3M, FMM, and the Ewald method for large periodic Coulombic systems,” *Comput. Phys. Commun.*, vol. 95, no. 2, pp. 93–110, Jun. 1996.

[118] “kspace_style command — LAMMPS documentation.” Retrieved February 11, 2019 from https://lammps.sandia.gov/doc/kspace_style.html.

[119] Yao, H. , Dai, Q., You, Z., Bick , A., Wang, M., and Guo, S., “Property Analysis of Exfoliated Graphite Nanoplatelets Modified Asphalt Model Using Molecular Dynamics (MD) Method,” *Appl. Sci,*vol. 7, no. 1, 2017.

[120] Hansen, J.P., and McDonald, I.R. (2013), *Theory of Simple Liquids - 4th Edition*, Academic Press.

[121] Jiang, G., Cheng, C., Li, D., and Liu, J. Z., “Molecular dynamics simulations of the electric double layer capacitance of graphene electrodes in mono-valent aqueous electrolytes,” *Nano Res.*, vol. 9, no. 1, pp. 174–186, Jan. 2016.

[122] Merlet, C., Péan, C., Rotenberg, B., Madden, P.A., Simon, P. and Salanne, M., " Simulating supercapacitors: can we model electrodes as constant charge surfaces? " *The journal of physical chemistry letters*, no 2, pp.264-268, 2012.

[123] Li, Z., Wang, J., Liu, S., Liu, X., and Yang, S., “Synthesis of hydrothermally reduced graphene/MnO_2 composites and their electrochemical properties as supercapacitors,” *J. Power Sources*, vol. 196, no. 19, pp. 8160–8165, Oct. 2011.

[124] Reddy, Ravinder, N., and Reddy, R.G.,"Sol–gel MnO_2 as an electrode material for electrochemical capacitors." *Journal of Power Sources*, no. 1, pp 330-337, 2003.

[125] Reddy, R. N., and Reddy, R. G.,“Porous structured vanadium oxide electrode material for electrochemical capacitors,” *J. Power Sources*, vol. 156, no. 2, pp. 700–704, Jun. 2006.

[126] Hu, Z., Zu, L., Jiang, Y., Lian, H., Liu, Y., Li, Z., Chen, F., Wang, X. and Cui, X., “High specific capacitance of polyaniline/mesoporous manganese dioxide composite using Ki-H_2SO_4 electrolyte.” *Polymers*, no. 10, pp.1939-1953, 2015.

[127] Karthikeyan, K., Kalpana, D., Amaresh, S., and Lee, Y. S., “Microwave synthesis of graphene/magnetite composite electrode material for symmetric supercapacitor with superior rate performance,” *RSC Adv.*, vol. 2, no. 32, pp. 12322–12328, Nov. 2012.

[128] Li, Z., Wang, J., Liu, X., Liu, S., Ou, J., and Yang, S., "Electrostatic layer-by-layer self-assembly multilayer films based on graphene and manganese dioxide sheets as novel electrode materials for supercapacitors," *J. Mater. Chem.*, vol. 21, no. 10, pp. 3397–3403, Feb. 2011.

[129] Ren, Y., Sun, C., Song, M., and Wang, L., "Preparation of Porous Carbon-Manganese Dioxide Nanocomposite as a Supercapacitor Electrode," *Int. J. Electrochem. Sci.*, vol. 11, no. 12, pp. 10706 – 10714, 2016.

[130] Jiang, G., Cheng, C., Li, D., and Liu, J. Z. ,"Molecular dynamics simulations of the electric double layer capacitance of graphene electrodes in mono-valent aqueous electrolytes," *Nano Res.*, vol. 9, no. 1, pp. 174–186, Jan. 2016.

[131] Falk, K., Sedlmeier, F., Joly, L., Netz, R.R. and Bocquet, L., " Molecular origin of fast water transport in carbon nanotube membranes: superlubricity versus curvature dependent friction. ", *Nano letters*, no. 10, pp.4067-4073, 2010

[132] Schoch, R. B., Lintel, H. V., and Renaud, P., "Effect of the surface charge on ion transport through nanoslits," *Phys. Fluids*, vol. 17, no. 10, p. 100604, Oct. 2005.

[133] Kalluri, R. K., Konatham, D., and Striolo, A., "Aqueous NaCl Solutions within Charged Carbon-Slit Pores: Partition Coefficients and Density Distributions from Molecular Dynamics Simulations," *J. Phys. Chem. C*, vol. 115, no. 28, pp. 13786–13795, Jul. 2011.

[134] Chmiola, J., Largeot, C., Taberna, P.L., Simon, P., and Gogotsi, Y., "Desolvation of Ions in Subnanometer Pores and Its Effect on Capacitance and Double-Layer Theory," *Angew. Chem. Int. Ed.*, vol. 47, no. 18, pp. 3392–3395, 2008.

[135] Szewczyk, A., Sikula, J., Sedlakova, V., Majzner, J., Sedlak, P., and Kuparowitz, T., "Voltage Dependence of Supercapacitor Capacitance," *Metrol. Meas. Syst.*, vol. 23, no. 3, pp. 403–411, Sep. 2016.

[136] Mark, P., and Nilsson, L. , "Structure and Dynamics of the TIP3P, SPC, and SPC/E Water Models at 298 K," *J. Phys. Chem. A*, vol. 105, no. 43, pp. 9954–9960, Nov. 2001.

APPENDICES

Appendix-A: Scanning Electron Microscope (SEM) Analysis

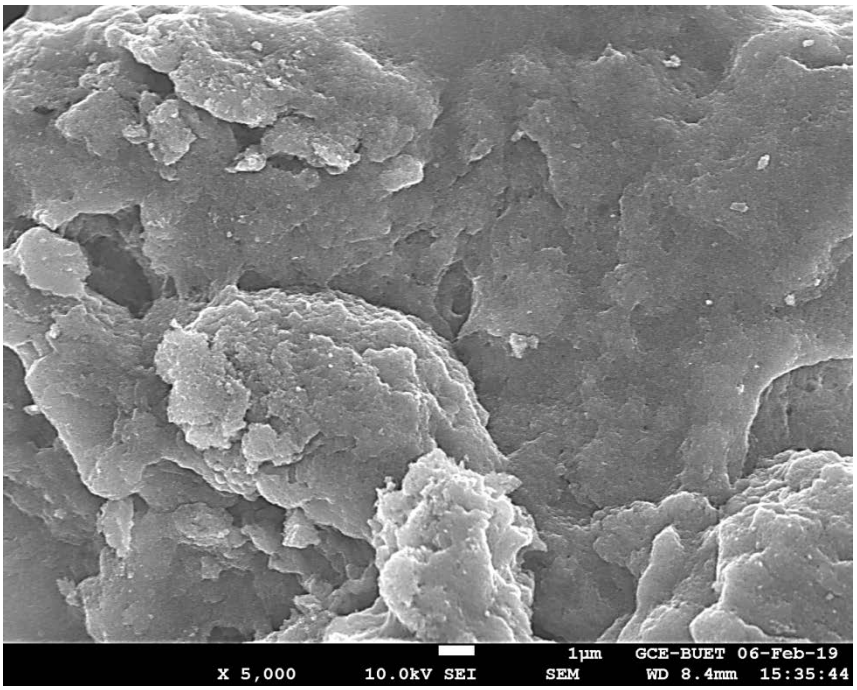

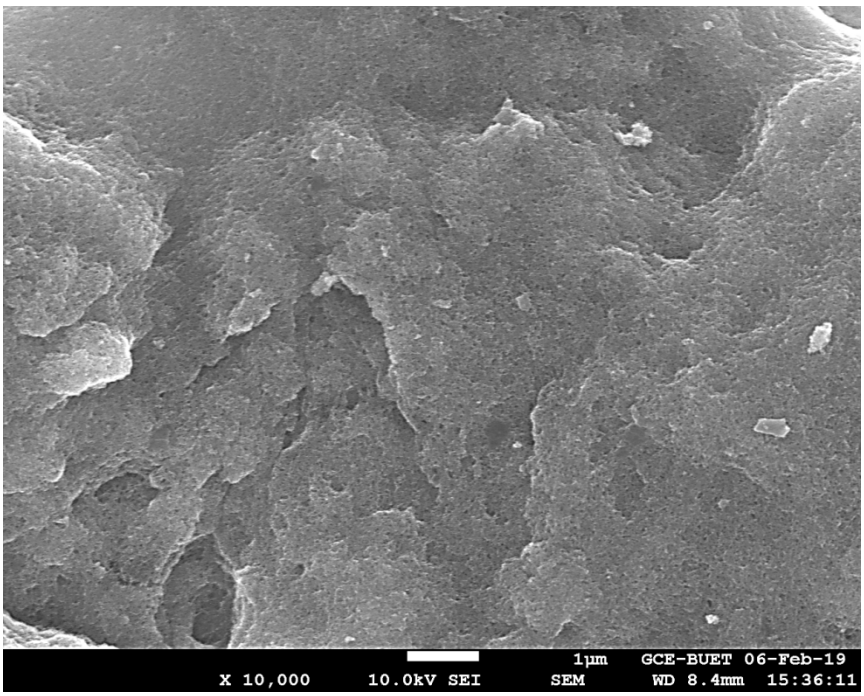

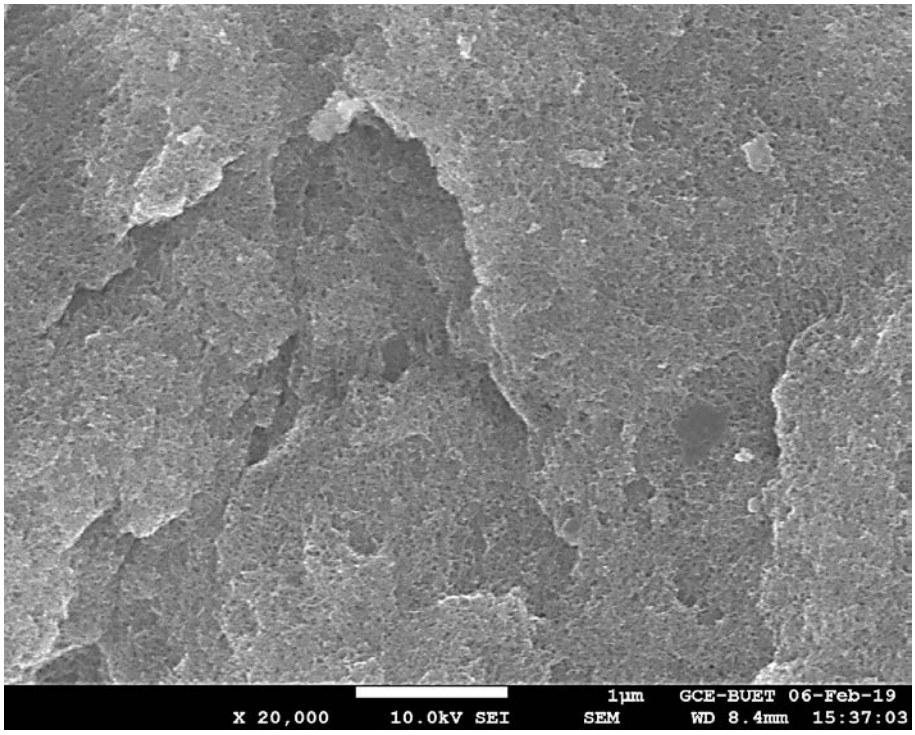
1µm GCE-BUET 06-Feb-19
X 20,000 10.0kV SEI SEM WD 8.4mm 15:37:03

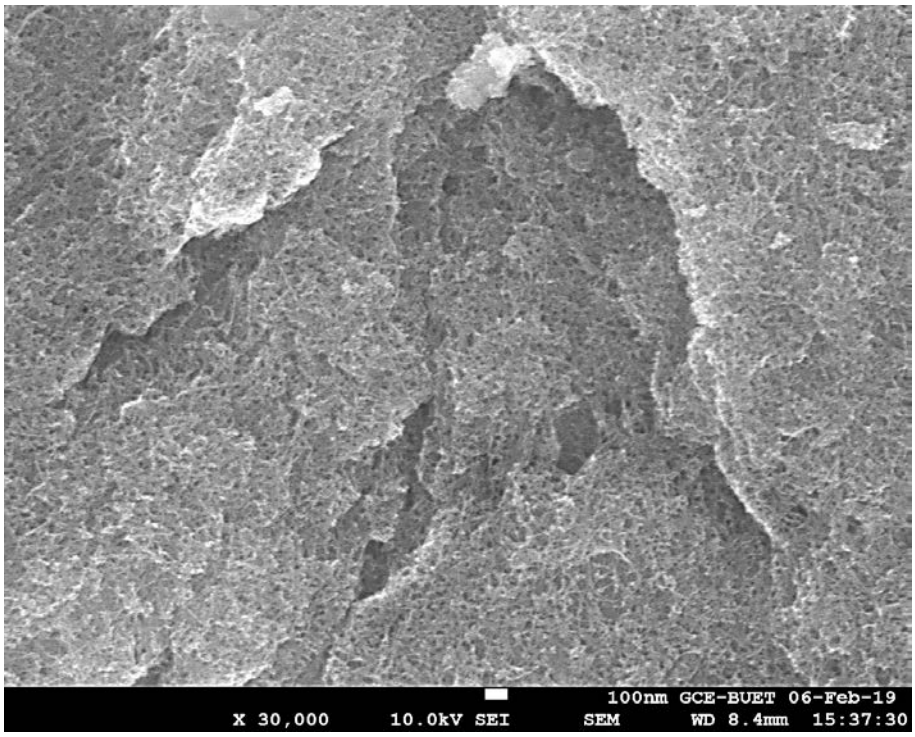
100nm GCE-BUET 06-Feb-19
X 30,000 10.0kV SEI SEM WD 8.4mm 15:37:30

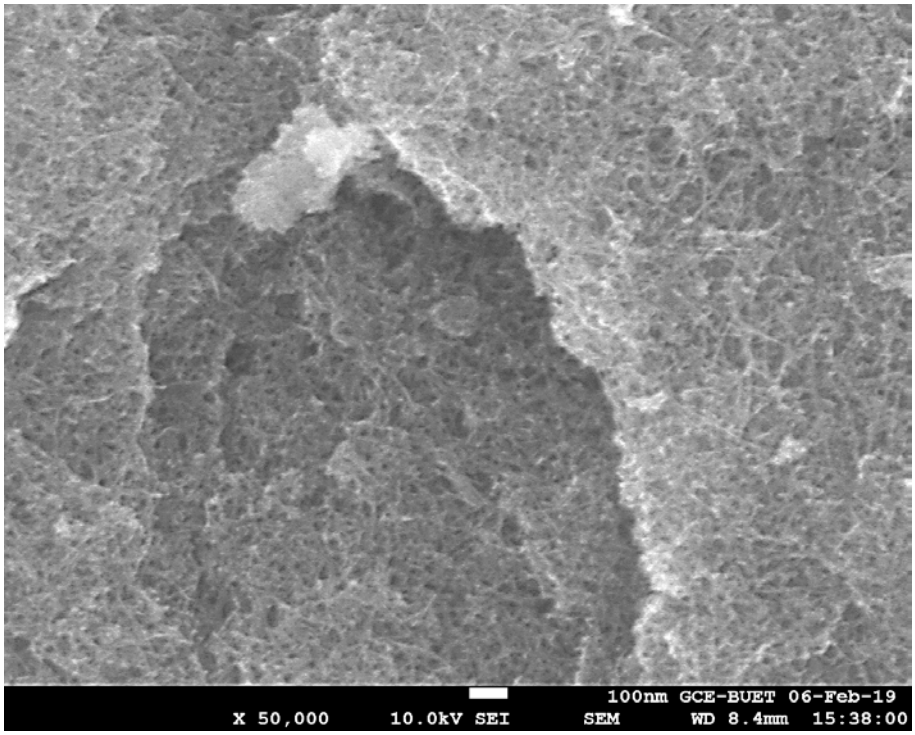
100nm GCE-BUET 06-Feb-19
X 50,000 10.0kV SEI SEM WD 8.4mm 15:38:00

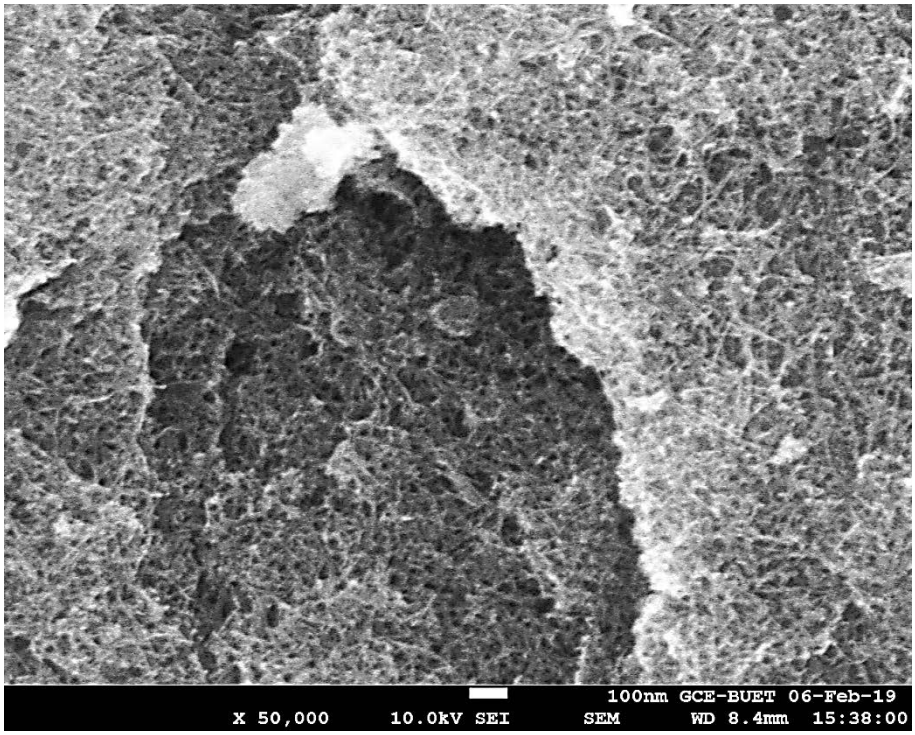
100nm GCE-BUET 06-Feb-19
X 50,000 10.0kV SEI SEM WD 8.4mm 15:38:00

Appendix–B: Energy Dispersive X-Ray Spectroscopy (EDX) Analysis

View002

JEOLUSER 1/1

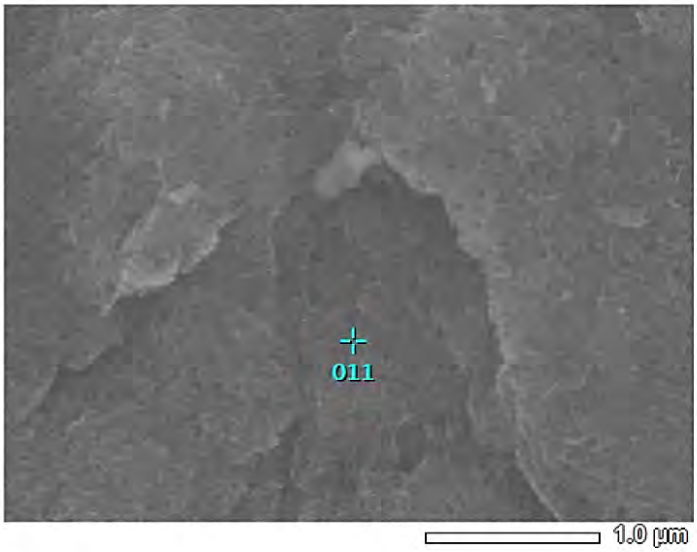


```
Title        : IMG1
----------------------------
Instrument   : 7600F
Volt         : 10.00 kV
Mag.         : x 30,000
Date         : 2019/02/06
Pixel        : 512 x 384
```

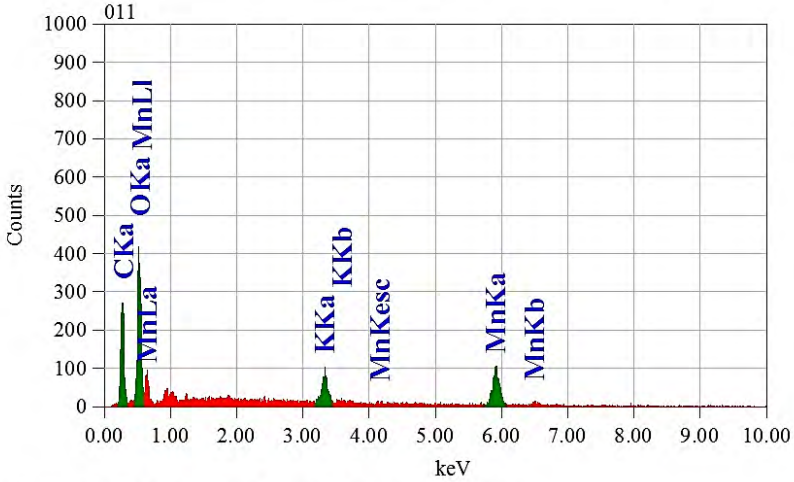


```
Acquisition Parameter
Instrument    : 7600F
Acc. Voltage  : 10.0 kV
Probe Current: 1.00000 nA
PHA mode      : T3
Real Time     : 30.13 sec
Live Time     : 30.00 sec
Dead Time     : 0 %
Counting Rate: 483 cps
Energy Range  :  0 - 20 keV
```

ZAF Method Standardless Quantitative Analysis
Fitting Coefficient : 0.1253

Element	(keV)	Mass%	Sigma	Atom%	Compound	Mass%	Cation	K
C K	0.277	24.50	0.30	45.59				15.4072
O K*	0.525	22.88	0.42	31.96				25.1285
K K	3.312	6.35	0.31	3.63				8.0595
Mn K	5.894	46.27	1.72	18.82				51.4048
Total		100.00		100.00				

JED-2300 AnalysisStation JEOL

View002

JEOLUSER 1/1

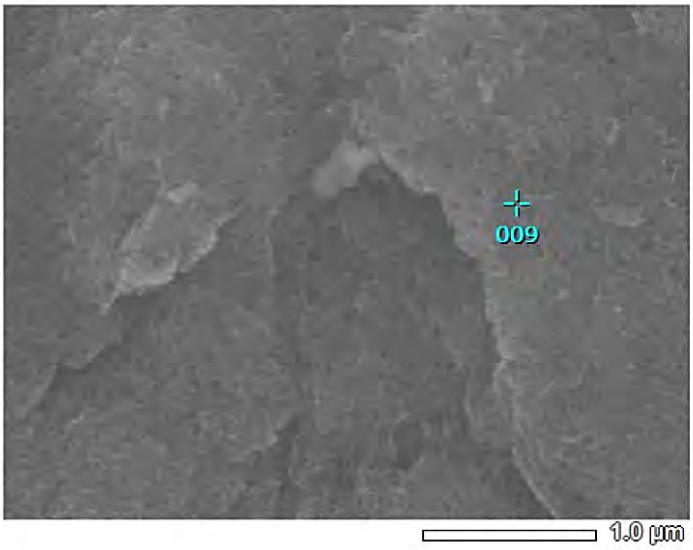


```
Title        : IMG1
---------------------------
Instrument   : 7600F
Volt         : 10.00 kV
Mag.         : x 30,000
Date         : 2019/02/06
Pixel        : 512 x 384
```

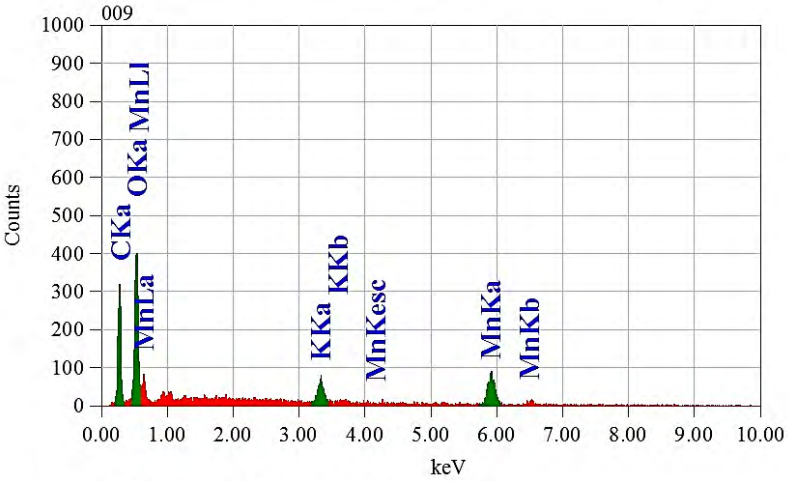


```
Acquisition Parameter
Instrument    : 7600F
Acc. Voltage  : 10.0 kV
Probe Current: 1.00000 nA
PHA mode      : T3
Real Time     : 30.13 sec
Live Time     : 30.00 sec
Dead Time     : 0 %
Counting Rate: 440 cps
Energy Range :  0 - 20 keV
```

ZAF Method Standardless Quantitative Analysis
Fitting Coefficient : 0.1331

Element	(keV)	Mass%	Sigma	Atom%	Compound	Mass%	Cation	K
C K	0.277	27.81	0.32	48.76				18.3680
O K	0.525	24.33	0.45	32.02				26.6328
K K	3.312	5.60	0.29	3.01				7.2488
Mn K	5.894	42.26	1.70	16.20				47.7504
Total		100.00		100.00				